ELECTROCHEMICAL PERFORMANCE OF METAL OXIDE DOPED MULTI-WALLED CARBON NANOTUBES

by

Ngwantshabu Bridget Mkhondo

DISSERTATION

Submitted in fulfilment of the requirements for the degree of

MASTER OF SCIENCE

in

CHEMISTRY

in the

FACULTY OF SCIENCE AND AGRICULTURE

(School of Physical and Mineral Sciences)

at the

UNIVERSITY OF LIMPOPO

SUPERVISOR: Dr T Magadzu

2015

DECLARATION

I declare that this dissertation is my own work and that all the sources that I have used or quoted have been indicated and acknowledged by means of complete references and that this work has not been submitted before for any other degree at any other institution.

Surname, Initials (Ms)

Date

PUBLICATIONS AND PRESENTATIONS

Publications

N.B. Mkhondo and T. Magadzu. Effects of different acid-treatment on the nanostructure and performance of carbon nanotubes in electrochemical hydrogen storage. Published in the *Digest Journal of Nanomaterials and Biostructures*, Vol. 9, No. 4, October-December 2014, p. 1331-1338.

Ngwantshabu B. Mkhondo, Pheladi M. Masipa, and Takalani Magadzu, Electrochemical storage of hydrogen on nickel oxide doped carbon nanotubes. To be submitted.

Oral presentation

N.B. Mkhondo and T. Magadzu. Electrochemical performance of acid-treated multi-walled carbon nanotubes. Presented at the University of Limpopo, Faculty of Science and Agriculture, 4th Annual Post-graduate Research Day, Bolivia lodge, South Africa, October 2013.

Poster presentation

N.B. Mkhondo and T. Magadzu. Electrochemical performance of acid-treated multi-walled nanotubes for hydrogen storage. Presented at the 5th International Conference on Nanoscience and Nanotechnology at Quest conference estates in Vanderbijlpark, Gauteng, March, 2014.

DEDICATION

To my parents, Salmita and Wilfred Mkhondo and my siblings, Lina, Queen and Peter Mkhondo.

ACKNOWLEDGEMENTS

ABSTRACT

The study has focused on the effects of different acids treatments on the nanostructure of MWCNTs; doping metal oxides (copper oxide (CuO), Iron (III) oxide (Fe_2O_3), nickel oxide (NiO) and cobalt oxide (Co_3O_4)) on MWCNTs and investigates their electrochemical hydrogen and energy storage capabilities. Fourier transform infrared (FTIR) confirmed the formation of functional groups on the surface of the acid treated MWCNTs. X-ray diffraction (XRD) showed that the graphitic structure of the MWCNTs was retained after treatment with mild acids (nitric acid (HNO_3), hydrogen peroxide (H_2O_2), a mixture of the acids, hydrogen peroxide: nitric acid (H_2O_2:HNO_3) and hydrogen peroxide: sulfuric acid (H_2O_2:H_2SO_4)). Transmission electron microscopy (TEM) confirms the removal of bamboo carbon structures inside the inner tubes of the MWCNTs after treatment with mild acids. Brunauer-Emmet-Teller (BET) showed an increase in the surface area of mild acids treated MWCNTs. Thermogravimetric analysis (TGA) results demonstrated that the thermal stability of MWCNTs increases after treatment with mixtures of the acids.

Different metal oxides treated at different temperatures were incorporated into MWCNTs (treated by a mixture of H_2O_2:HNO_3). X-ray diffraction (XRD), scanning electron microscopy (SEM) and Transmission electron microscopy (TEM) confirmed the presence of different metal oxides inside/on the surface of the acid treated MWCNTs.

The MWCNTs treated by H_2O_2:HNO_3 gave both the highest discharge capacity (72.63 mAh/g) and capacitance (8.61 F/g), as compared to the other electrode materials. The improved hydrogen storage capacity and specific capacitance can be attributed to high surface area, wider pore size distribution and the amount of functional groups on the surface of H_2O_2:HNO_3-treated MWCNTs; with the functional groups acting as electron transmitters. The 5wt.% CuO@300°C-MWCNTs composite showed the highest hydrogen storage capacity of 159 mAh/g. This capacity was further improved by addition of manganese oxide resulting in the highest discharge capacity of 172 mAh/g (which is equivalent to 0.64 wt.% of hydrogen stored). The

highest specific capacitance of 9.70 F/g was obtained on 5wt% Fe_2O_3@400ºC-MWCNTs composite.

TABLE OF CONTENT

LIST OF FIGURES

LIST OF TABLES

LIST OF ABBREVIATIONS

Ag/AgCl	–	Silver/silver chloride
A-MWCNTs	–	Acid-treated multi-walled carbon nanotubes
BASi	–	Bioanalytical System, inc.
BET	–	Brunauer-Emmett-Teller
BJH	–	Barrett-Joyner-Halenda
CBD	–	Chemical bath deposition
CNTs	–	Carbon nanotubes
CO	–	Carbonyl
CO_2	–	Carbon dioxide
COOH	–	Carboxylic acid
Co_3O_4	–	Cobalt oxide
$CoCl_2.6H_2O$	–	Cobalt (II) chloride hexahydrate
C_S	–	Specific capacitance
CP	–	Chronopotentiometry
CPE	–	Controlled Potential Electrolysis
$Co(NO_3)_2.6H_2O$	–	Cobalt (II) nitrate hexahydrate
$Cu(NO_3)_2.3H_2O$	–	Copper (II) nitrate trihydrate
CuO	–	Copper oxide
CV	–	Cyclic voltammetry
DBD	–	Dielectric barrier discharge
DC	–	Discharge capacity

DI	–	Deionised water
DOE	–	Department of Energy
EDLC's	–	Electrical double-layer capacitors
EDX	–	Energy dispersive X-ray
$Fe(NO_3)_3.9H_2O$	–	Iron (III) nitrate nonahydrate
Fe_2O_3	–	Iron (III) oxide
FT-IR	–	Fourier transform infrared
GCE	–	Glassy carbon electrode
H^+	–	Hydrogen ion
H_2	–	Hydrogen
HNO_3	–	Nitric acid
H_2O_2	–	Hydrogen peroxide
H_2SO_4	–	Sulfuric acid
$KMnO_4$	–	Potassium permanganate
KOH	–	Potassium hydroxide
Li	–	Lithium
LSV	–	Linear sweep voltammetry
m	–	Mass
$MnCl_2$	–	Manganese chloride
MnO_2	–	Manganese oxide
MO	–	Metal oxide
MWCNTs	–	Multi-walled carbon nanotubes
N_2	–	Nitrogen

Na_2SO_4	–	Sodium sulphate
NH_3	–	Ammonia
$Ni(NO_3)_2.6H_2O$	–	Nickel nitrate hexahydrate
NiO	–	Nickel oxide
N,N-DMF	–	N,N-Dimethylformamide
PEM	–	Proton Exchange Membrane
pH	–	Hydrogen potential
Pt	–	Platinum
PTFE	–	Poly (tetrafluorethylene)
RMS	–	Raman spectroscopy
SEM	–	Scanning electron microscopy
SWCNTs	–	Single-walled carbon nanotubes
TEM	–	Transmission electron microscopy
TGA	–	Thermogravimetric analysis
v	–	Scan rate
V	–	Voltage
wt.%	–	Weight percentage
XRD	–	X-ray diffraction

CHAPTER 1

INTRODUCTION

1.1. Background

Fluctuations in the price of crude oil signal a major threat to the present fossil fuel dominated energy economy [1]. On the other hand public concerns about global environmental problems associated with the utilization of fossil fuels are also increasing. Fossil fuels are not infinitely available and this might be a major problem for future generations [2]. Therefore, the search for alternative energy sources is an extremely important issue. There are a number of alternative primary renewable energy sources currently available, such as thermonuclear energy, wind energy, hydropower, solar energy, geothermal energy, etc. A major problem with several of this renewable energy sources is that they are intermittent and their energy density is low [1].

Hydrogen has attracted attention as a possible alternative energy carrier, because of its high energy density, its efficiency and its role in the reduction of air pollution [3]. However, it has not been so far used in great extent, due to the existence of major scientific challenges, such as the lack of a safe, effective and affordable hydrogen storage system [4, 5]. There are three methods of storing hydrogen: Gasification, condensation and solidification. Liquefying hydrogen wastes at least 1/3 of the stored energy while the crucial issue connected with compressed gas is safety. Solidification is the widely accepted method for hydrogen storage [6]. Materials which have been traditionally used for hydrogen storage in the solid form are metal-hydride, but the general weakness of all known metal hydrides is the low mass density, high weight and the lack of reversibility within the required range of temperature and pressure [2].

Carbon nanotubes (CNTs) have attracted considerable interest as possible hydrogen storage material due to their extraordinary properties such as light weight, high

electrochemically assessable surface area of porous nanotubes arrays, excellent electronic conductivity and useful chemical stability [2]. Hydrogen sorption in CNTs can be performed by physisorption and electrochemical methods [4, 7 and 8]. In physisorption, hydrogen is weakly held such that high pressures or low temperatures are often required. This makes physisorbed materials much less attractive for applications at ambient temperatures [9]. In the electrochemical method, there is no need to use high pressure and the hydrogen sorption process occurs directly on the electrode surface at ambient conditions. Hence, this method is very attractive for many applications [10].

Carbon nanotubes are also among the attractive materials for supercapacitors because of their superb properties [11]. Supercapacitors are energy storage systems that have received great attention due to their unique characteristics, such as high power density, fast charging/discharging rate and long term cyclability [12].

1.2. Electrochemical performance of metal oxide supported on carbon nanotubes

CNTs alone have been reported to have low hydrogen and energy storage capacities [13, 14]. Liu *et al.* [15] reported a discharge capacity of 10.5 mAh/g, corresponding to an electrochemical hydrogen storage capacity of about 0.04 wt.% for acid treated multi-walled carbon nanotubes. However, this is far below the benchmark set for on-board hydrogen storage systems by the US Department of Energy [16]. They further demonstrated that MWCNTs can still be modified to store large amounts of hydrogen.

Amongst other factors, the challenge for CNTs utilisation in energy storage is their relative low capacitance [14]. One approach to overcome this disadvantage is to dope the modified CNTs with metal oxides that have a high specific capacitance [14, 17]. Nanostructured transition metal oxides possess the excellent properties such as high surface area, low toxicity and high specific capacitance [11, 12, 18-24]. They have been widely used for practical applications such as heterogeneous catalysis, sensing, photovoltaics, energy conversion and storage and optoelectronics. The integration of CNTs and nanostructured transition metal oxides could generate new

kinds of nanocomposites with multifunctional properties benefited from each kind of nanostructures [25]. Nam *et al.* [21] prepared nickel oxides on carbon nanotube electrodes (NiO_x/CNT electrodes) by depositing $Ni(OH)_2$ electrochemically onto CNT film followed by subsequent heating to 300 °C. The highest normalised specific capacitance of 1701 F/g was obtained for the NiO_x/CNT electrode with 8.9 wt.% of NiO_x. They demonstrated that the pseudocapacitance of NiO_x/CNT electrodes in a 1 M KOH solution originates from redox reactions of NiO_x/NiO_xOH and $Ni(OH)_2/NiOOH$. Nickel oxide (NiO), iron (III) oxide (Fe_2O_3), manganese oxide (MnO_2), copper oxide (CuO) and cobalt oxide (Co_3O_4) are among the transition metal oxides that have shown promising electrochemical activities [18-24].

1.3. Purpose of the study

1.3.1. Aim

The aim of the study is to investigate the electrochemical performance of acid-treated MWCNTs and metal oxide doped MWCNTs for hydrogen and energy storage.

1.3.2. Objectives

The objectives of the study will be to:

i.   investigate the effects of acid treatment on the structure and electrochemical performance of multi-walled carbon nanotubes,

ii. prepare different metal oxides (CuO, Fe_2O_3, NiO and Co_3O_4) nanoparticles by using different temperature pre-treatments,

iii. modify the acid treated multi-walled carbon nanotubes with metal oxides nanoparticles,

iv. investigate the influence of metal oxides on the electrochemical properties of acid treated multi-walled carbon nanotubes, for energy (supercapacitors) and hydrogen storage.

1.4. Dissertation outline

The remaining chapters are organised as follows: The literature review is reported in chapter 2 as follows: (a) Structure, treatment and properties of carbon nanotubes, (b) general introduction to properties and synthesis of metal oxide nanoparticles, (c) general introduction to characterisation techniques such as: FTIR, XRD, SEM, TEM, TGA and RMS, (d) general applications of CNTs in electrochemical energy storage, (e) hydrogen economy, (f) supercapacitors and (g) application of carbon nanotubes for electrochemical hydrogen storage and supercapacitor applications.

Chapter 3 describes the methodologies followed throughout the research project that includes the treatment of MWCNTs by different acids/oxidisers, the preparation of metal oxide nanoparticles, the incorporation of metal oxide nanoparticles into MWCNTs, the characterisation of the prepared materials and finally the electrochemical tests. The results of the study will be presented in chapter 4 and 5. The effect of each acid on the structural properties, and electrochemical performance of MWCNTs towards hydrogen storage and supercapacitors was studied and the results are presented in chapter 4. The results show that acid treatment of MWCNTs with mild acids improves both the structural and electrochemical properties of MWCNTs.

The acid treated MWCNTs were modified by different metal oxides, CuO, Fe_2O_3, NiO and Co_3O_4, prepared at three different temperatures, 300 ^{o}C, 400 ^{o}C and 500 ^{o}C. The characterisation and electrochemical performance of the metal oxide-MWCNTs composites are presented in chapter 5. The results show that metal oxides prepared at low temperature have smaller crystallite sizes and improves the electrochemical performance of MWCNTs. Chapter 6 gives the general conclusion of the results of the experiments conducted in this research project. Finally, in this dissertation, figures and tables are integrated within the text, followed by a listing of references at the end of each chapter.

1.5. References

[1] Sankaran M, On the potential of carbon materials for solid state hydrogen storage, Indian Institute of Technology Madras (2006) 1-203

[2] Hui-Ming C, Quan-Hong Y and Chang L, Hydrogen storage in carbon nanotubes, Carbon 39 (2001) 1447-1454

[3] Chiao K, Carbon nanotubes for hydrogen storage, Physics Letters A 30 (2002) 1-14

[4] Strobel R, Garche J, Moseley P.T, Jorissen L and Wolf G, Hydrogen storage by carbon materials, Journal of Power Sources 159 (2006) 781-801

[5] Hermosilla-Lara G, Momen G, Marty P.H, Le Neindre B and Hassouni K, Hydrogen storage by adsorption on activated carbon: Investigation of the thermal effects during the charging process, International Journal of Hydrogen Energy 32 (2007) 1542-1553

[6] Haiyan Z, Xiaojuan F, Jianfeng Y, Chun Z, Yiming C, Minghu I and Aixiang W, The effect of MWCNTs with different diameters on the electrochemical hydrogen storage capability, Physics Letters A 339 (2005) 370-377

[7] Aqel A, Abou EL-Nour K.M.M, Ammar R.A.A and AL-Warthan A, Carbon nanotubes, science and technology part (1) structure, synthesis and characterisation, Arabian Journal of Chemistry 5 (2012) 1-23

[8] Li S, Pan W and Moa Z, A comparative study of the electrochemical hydrogen storage properties of activated carbon and well-aligned carbon nanotubes mixed with copper, International Journal of Hydrogen Energy 30 (2005) 643-648

[9] Lueking A.D, Pan L, Narayanan D.L and Clifford C.E.B, Effect of expanded graphite lattice in exfoliated graphite nanofibres on hydrogen storage, Journal of Physical Chemistry B 109 (2005) 12710-12717

[10] Wang D.W, Li F, Liu M, Lu G.Q and Cheng H.M, 3D aperiodic hierarchical porous graphitic carbon material for high-rate electrochemical capacitive energy storage, Angewandte Chemie-International Edition 47 (2008) 373-376

[11] Wang G, Zhang B, Yu Z and Qu M, Manganese oxide/MWCNTs composite electrodes for supercapacitors, Solid State Ionics 176 (2005) 1169-1174

[12] Wang J, Yang Y, Huang Z and Kang F, Synthesis and electrochemical performance of MnO_2/CNTs-embedded carbon nanofibers nanocomposites for supercapacitors, Electrochimica Acta 75 (2012) 213-219

[13] Chang L, Yong C, Cheng-Zhang W, Shi-Tao X and Hui-Ming C, Hydrogen storage in carbon nanotubes revisited, Carbon 48 (2010) 452-455

[14] Chou S.L, Wang J.Z, Chew S, Liu H.K and Dou S.X, Electrodeposition of MnO_2 nanowires on carbon nanotube paper as free-standing, flexible electrode for supercapacitors, Electrochemistry Communications 10 (2008) 1724-1727

[15] Liu E, Wang J, Li J, Shi C, He C and Du X, Enhanced electrochemical hydrogen storage capacity of multi-walled carbon nanotubes by TiO_2 decoration, International Journal of Hydrogen Energy 36 (2011) 6739-6743

[16] U.S. Department of Energy, Multi-Year Research, development and demonstration Plan: Planned program activities for 2003-2010,http://www.eere.energy.gov/hydrogenandfuelcells/mypp/ (Aug. 2005).5

[17] Qinghua H, Xianyou W and Jun L, Characterisation and performance of hydrous manganese oxide prepared by electrochemical method and its application for supercapacitors, Electrochimica Acta 52 (2006) 1758-1762

[18] Adekunle A.S, Agboola B.O, Pillay J and Ozoemena K.I, Electrocatalytic detection of dopamine at single-walled carbon nanotubes–iron(III) oxide nanoparticles platform, Sensors and Actuators B 148 (2010) 93-102

[19] Salimi A, Mamkhezri H, Hallaj R and Soltanian S, Electrochemical detection of trace amount of arsenic(III) at glassy carbon electrode modified with cobalt oxide nanoparticles, Sensors and Actuators B 129 (2008) 246-254

[20] Xie L, Wu J, Chen C, Zhang C, Wan L, Wang J, Kong Q, Lv C, Li K and Sun G, A novel asymmetric supercapacitor with an activated carbon cathode and a reduced graphene oxide cobalt oxide nanocomposite anode, Journal of Power Sources 242 (2013) 148-156

[21] Nam K, Kima K, Lee E, Yoon W and Yang X, Pseudocapacitive properties of electrochemically prepared nickel oxides on 3-dimensional carbon nanotube film substrates, Journal of Power Sources 182 (2008) 642-652

[22] Pendashteh A, Mousavia M.F and Rahmanifar M.S, Fabrication of anchored copper oxide nanoparticles on graphene oxide nanosheets via an electrostatic co-precipitation and its application as supercapacitor, Electrochimica Acta 88 (2013) 347-357

[23] Dubal D.P, Gund G.S, Holze R and Lokhande C.D, Mild chemical strategy to grow micro-roses and micro-woolen like arranged CuO nanosheets for high performance supercapacitors, Journal of Power Sources 242 (2013) 687-698

[24] Yan J, Fan Z, Wei T, Cheng J, Shao B, Wang K, Song L and Zhang M, Carbon nanotubes/MnO_2 composites synthesised by microwave-assisted method for supercapacitors with high power and energy densities, Journal of Power Sources 194 (2009)1202-1207

[25] Yan J, Zhou H, Yu P, Su L and Mao L, A general electrochemical approach to deposition of metal hydroxide/oxide nanostructures onto carbon nanotubes, Electrochemistry Communications 10 (2008) 761-765

CHAPTER 2

LITERATURE REVIEW

2.1. Structural features of carbon nanotubes

CNTs were reported in 1991 by Iijima [1] and are regarded as an inner hollow nanotube rolled with graphene sheets, having an inner diameter of 0.7 nm up to several nanometres and a length of 10-100 μm [2]. The ratio of length to diameter is above 1000 [8]. Tubes formed by only one single graphene sheet are called single-walled carbon nanotubes (SWCNTs) and tubes containing multiple concentric graphene sheets are called multi-walled carbon nanotubes (MWCNTs) [3], as shown in figure 2.1. Double-walled carbon nanotubes (DWCNTs) also exist and are sometimes classified as MWCNTs [5]
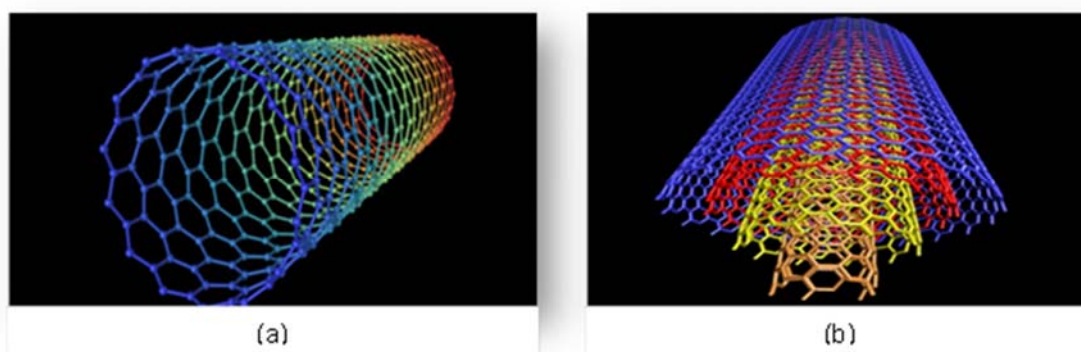
Figure 2.1: Structure of (a) SWCNTs and (b) MWCNTs [4]

2.2. Treatment of carbon nanotubes

Treatment of CNTs can be defined as a process that separates nanotubes from non-nanotube impurities. Impurities include amorphous carbon, catalysts and carbon nanoparticles [5]. CNTs are close ended and the caps can also be removed during the treatment process depending on the treatment process [6, 7]. Although CNTs have attracted attention as possible energy storage medium, their application has been largely hampered by their poor dispersion in solvents or polymers. This is

caused by the strong intermolecular Van der Waals interactions that exist among the nanotubes, which lead to the formation of aggregates [8]. In order to improve the chemical reactivity and interaction of CNTs with foreign molecules, it is necessary to modify the surface of CNTs [9].

The introduction of surface oxides, carboxylic (-COOH), alcohol (-C-OH) and ketone (-C=O), is a widely used approach to overcome the above mentioned problem. By tailoring the structural and electronic properties, the surface oxides can act as anchoring sites for the active surface species (metal ions and oxide, organic molecules, etc.) for specific catalytic reactions [10]. Oxidation of CNTs is more widely carried out by treatment with aqueous solutions of acids or oxidising agents, such as H_2SO_4, HNO_3, H_2SO_4/HNO_3, H_2O_2, $KMnO_4$, $KMnO_4/H_2SO_4$, etc [11-16]. Usually the amount and type of surface groups depends strongly on the method of oxidation and the type of the oxidiser [17]. Treatments methods can generally be separated into two methods i.e., dry and wet methods [5].

2.2.1. Dry methods

This refers to methods that can selectively remove amorphous carbon species within the MWCNTs sample. Amorphous carbon species are highly reactive as compared to carbon nanotubes, hence are easily oxidised [5]. The simplest dry method is air oxidation at selected temperatures [18]. Oxidation is performed at temperatures between 300 °C and 500 °C, metal and carbon impurities are oxidised at these temperatures. Another dry method is annealing, where the nanotubes will be rearranged and defects will be consumed, due to high temperatures (873-1873 K) [19]. Reyhani *et al*. [21] studied the effects of multi-walled carbon nanotubes graphitisation by treating them at different atmospheres. They found that the graphitisation of the purified MWCNTs treated by various atmospheres, increased as follows: $NH_3 < CO_2 < N_2 < H_2$.

2.2.2. Wet methods

Wet methods treat carbon nanotubes in aqueous solutions of strong acids or oxidising agents, such as H_2SO_4, HNO_3, HNO_3/H_2SO_4, H_2O_2, $KMnO_4$, etc [5, 10].

The method can be used alone or together with dry methods. Most dry methods are followed by a step of acid treatment to dissolve metal catalyst and/or metal oxides formed during the gas-phase oxidation step [5].

2.2.2.1. Treatment using acids

Dai *et al.* [23] treated MWCNTs with various HNO_3 concentrations (1 M, 3 M, and 5 M) at 200 ºC. They reported that the MWCNTs treated by the highest concentration (5 M) show better surface properties in relation to the MWCNTs treated by 1 M HNO_3. The characteristic peaks of –CO at IR bands 950-1300 cm^{-1} and –OH at 3440 cm^{-1} functional groups are not well observed on the FTIR spectra of MWCNTs treated by low concentration of HNO_3 (1 M), but they become more clearer as the HNO_3 concentration increase. They further demonstrated that intensities of –CO and –OH functional groups increase with increase in the HNO_3 concentration from 1 M HNO_3 to 5 M HNO_3.

Naseh *et al.* [9] functionalised MWCNTs using two separate methods. One method is a chemical treatment which includes refluxing in HNO_3 for 4 h and the other is done by dry treatment using dielectric barrier discharge (DBD) plasma under air atmosphere. They reported that both chemical and plasma functionalisation increase specific surface area of nanotubes. They suggested that functionalisation causes opening up of tube ends and generate defects on the sidewalls of nanotubes, therefore access into the cavity of the nanotubes can be achieved.

2.2.2.2. Treatment using mixtures of acids

Mazov *et al*. [22] oxidised multiwall carbon nanotubes (MWCNT) with three medium diameters (20-22, 9-13, and 6-8 nm) and different morphology chemically, using concentrated nitric acid, mixture of nitric and sulphuric acids ("mélange" solution) and mixture of sulphuric acid and hydrogen peroxide ("piranha" solution). They demonstrated that the amount of oxygen-containing groups on the surface of oxidised MWCNTs depends on the type of initial MWCNTs. Chiang Y *et al.* [10] investigated the variation in the nature of multi-walled carbon nanotubes (MWCNTs) subjected to different degrees of oxidation. Their results demonstrate that the

graphitic structure of nanotubes oxidised with a mild mixture of H_2SO_4/HNO_3 was preserved.

Shirazi *et al.* [24] oxidised CNTs by HNO_3/H_2SO_4 (1/3) and 8 M HNO_3 respectively. Their results demonstrated that the best acid treatment was performed using 8 M HNO_3. Their Raman spectroscopy results revealed that acid treatment with $HNO_3:H_2SO_4$ (1/3) could increase the degree of disordering of the MWCNTs. This was attributed to the destroying effect of this acid treatment method.

2.3. Properties of carbon nanotubes

Electronic, molecular and structural properties of CNTs are determined to a large extent by their structure [25]. The most important properties of CNTs are high chemical reactivity, high electrical conductivity, high optical activity and high mechanical stability. The chemical reactivity of CNTs, as compared with a graphene sheet, is enhanced as a direct result of the curvature of the CNT surface [26]. Depending on their chiral vector, CNTs with a small diameter are either semi-conducting or metallic. The differences in conducting properties are caused by the molecular structure that results in a different band structure and thus a different band gap [27]. Theoretical studies have revealed that the optical activity of chiral nanotubes disappears if the nanotubes become larger [28]. Theoretical calculations and experimental results indicate that CNTs are stiffer than diamond and exhibit the highest Young's modulus and tensile strength. For example, SWCNT has a Young's modulus that is approximately five times larger and a tensile strength that is approximately 375 times larger than that of steel [29].

2.4. Properties of metal oxides nanoparticles

Transition metal oxides play a very important role in many areas of chemistry, physics and material science [30]. Metals form a large diversity of oxide compounds that can adopt a vast number of structural geometries with an electronic structure that can exhibit metallic, semiconductor or insulator character. Metal oxide nanoparticles can exhibit unique physical and chemical properties due to their limited size and high surface to area ratio, different from those of the bulk [31]. They have

been widely used for practical applications such as heterogeneous catalysis, sensing, photovoltaics, energy conversion and storage, and optoelectronics [32]. Below follows a list of the metal oxides which we focused on in this research project. They were chosen mainly due to the wide range of literature available on first row transition metal oxides. Availability and low cost are also amongst the factors which were considered in choosing the different metal oxides.

2.4.1. Iron oxide

Iron oxide (Fe_2O_3) is considered as a promising electrode material due to its availability, low cost, environment friendly and high capacity [33,]. Fe_2O_3 has been widely used as an anode material in lithium ion batteries [33, 34]. Xie *et al.* [35] investigated highly ordered iron oxide nanotube arrays (fabricated by a simple and cost-effective anodisation method on iron foils) as electrodes for electrochemical energy storage. The α-Fe_2O_3 nanotube arrays exhibit high specific capacitance of 138 F/g at 1.3 A/g. The high specific capacitance was attributed to the unique nanostructures of the α-Fe_2O_3 nanotube arrays, which provide high surface area, fast ion transport pathways and robust structures. Enhanced electrocatalysis is anticipated in Fe_2O_3-CNTs materials due to the electronic interaction between the Fe_2O_3 nanoparticles and CNTs [36].

2.4.2. Cobalt oxide

Cobalt oxides (Co_3O_4) possess advantages such as low cost, natural abundance and environment safety [37]. Co_3O_4 is also known to be highly reactive and has been employed in processes such as energy storage, electrochromic thin films, magneto resistive devices and heterogenous catalysis. Co_3O_4 continue to attract considerable interest due to the excellent electrocatalytic activity [38], its high theoretical capacitance and defined redox behaviour [39]. Deng *et al.* [40] prepared Co_3O_4 by a one-step solution combustion process by adjusting the molar ratio of citric acid (fuel) and $Co(NO_3)_2.6H_2O$ (oxidiser). A specific capacitance of 179.7 F/g was obtained when the citric acid/$Co(NO_3)_2.6H_2O$ molar ratio was 7:27. Lang *et al.* [37] reported the highest specific capacitance of 263 F/g for Co_3O_4 prepared by ultrasonic treatment using $CoCl_2.6H_2O$ as the Co_3O_4 precursor.

2.4.3. Nickel oxide

Nickel oxide (NiO) has generated great interest as a possible electrode material for supercapacitors due to its low cost of raw materials, its low toxicity and non-flammable properties making it safe to handle. NiO has also exhibited excellent cycling abilities [41]. Inamdar *et al.* [42] studied the electrochemical supercapacitor properties of nickel oxide in two different electrolytes, namely, NaOH and KOH. A specific capacitance of ~ 129.5 F/g and 69.8 F/g was obtained in NaOH and KOH electrolyte, respectively. The porous nickel oxide film was synthesised by means of a chemical bath deposition technique from an aqueous nickel nitrate solution.

2.4.4. Copper oxide

Copper oxide (CuO) is an attractive candidate for electrode material due to its low cost, abundant resources and non-toxicity [43]. Copper oxide has recently indicated a promising capacitance value [44]. Pendashteh *et al.* [43] reported a specific capacitance of 125 F/g for CuO nanoparticles prepared through a sonochemical assisted precipitation followed by thermal treatment. Gao *et al.* [45] synthesised CuO for use as a hydrogen storage electrode material, by a dehydration reaction. They reported that the cycle life of CuO electrode, remained over 70 mAh/g after being cycled 50 times at the charge-discharge current density of 10 mA/g. They further demonstrated that this indicates that the as-prepared CuO products have a strong resistance against oxidation and corrosion.

2.4.5. Manganese oxide

Among the studied metal oxide, manganese oxide (MnO_2) is also an attractive candidate for supercapacitors due to its availability, low cost, none-polluting effects and high specific capacitance [46, 47]. Donne *et al.* [48] obtained the specific capacitance of 150 F/g for MnO_2 prepared by a hydrothermal decomposition of permanganate in 0.01 M H_2SO_4 solution. Staiti and Lufrano [49] reported the highest specific capacitance of 267 F/g for a manganese oxide material synthesised by the reduction of potassium permanganate (VII) with manganese chloride. The best capacitive performance was obtained with the material treated at 200 ^{o}C.

2.5. Method of synthesising metal oxides nanoparticles

The preparation methods of metal oxide nanoparticles may be grouped into two main streams as liquid-solid and gas-solid transformations [50]. Regardless of the technique, the goal of particle synthesis generally focuses on minimising and controlling particle size, maintaining a narrow size distribution, control of particle morphology and control of crystallinity. The ability to control size enables the variation of particle properties, while the narrow size distribution allows greater precision and is required for studies of size dependent effects. Particle shape and crystal structure can also influence material properties. For example, the crystalline structure of a particle may affect its stability and adsorption properties [51].

2.5.1. Liquid-solid transformation

A number of specific methods in the liquid-solid transformation have been developed among which those broadly in use are listed below.

2.5.1.1. Co-precipitation methods

This involves dissolving a salt precursor (chloride, nitrate, etc) in water (or other solvent) to precipitate the oxo-hydroxide form with the help of a base [50]. Staiti and Lufrano [49], synthesised a manganese oxide material by precipitation from an aqueous solution of potassium permanganate (vii) and manganese (ii) chloride at 25 ^{o}C. This method resulted in the formation of a mixed oxide materials having the general formula MnO_α. The prepared MnO_α was then used as an electrode material for electrochemical supercapacitor. Dubal *et al.* [44] prepared different nanostructures of the CuO by changing complexing agents in a chemical bath deposition (CBD) method. The prepared CuO nanostructures showed better surface properties like uniform pore size distribution and improved high rate pseudocapacitance. Pendashteh *et al.* [43] synthesised copper oxide nanoparticles using a sonochemical assisted precipitation followed by thermal treatment.

14

2.5.1.2. Sol-gel processing

The method prepares metal oxides via hydrolysis of precursors, usually alkoxides in alcoholic solution, resulting in the corresponding oxo-hydroxide. Condensation of molecules by giving off water leads to the formation of a network of the metal hydroxide. Hydroxide-species undergo polymerisation by condensation and form a dense porous gel. Appropriate drying and calcinations lead to ultrafine porous oxides [52].

2.5.1.3. Microemulsion technique

Microemulsion or direct/inverse micelles represent an approach based on the formation of micro/nano-reaction vessels under a ternary mixture containing water, a surfactant and oil. Metal precursors on water will precede precipitation as oxo-hydroxides within the aqueous droplets, typically leading to monodispersed materials with size limited by the surfactant-hydroxide contact [53].

2.5.1.4. Solvothermal methods

In this case, metal complexes are decomposed thermally either by boiling in an inert atmosphere or using an autoclave with the help of pressure. A suitable surfactant agent is usually added to the reaction media to control particle size growth and limit agglomeration [50].

2.5.1.5. Template/Surface derivative methods

Template techniques are common to some of the previous mentioned methods and use two types of tools; soft-templates (surfactants) and hard-templates (porous solids as carbon or silica). Template- and surface-mediated nanoparticles precursors have been used to synthesise self-assembly systems [50].

2.5.2. Gas-solid transformations

Several gas-phase synthetic techniques have been used to prepare nanoparticles. These methods use both inert and reactive atmospheres at a variety of pressures. Gas phase nanoparticle synthesis methods include electrospray, flame pyrolysis, vaporisation and condensation using lasers and other heat sources, laser ablation and plasma synthesis. These methods feature the rapid cooling of evaporated material to induce nucleation and growth of nanoparticles, typically within a confined region. Particle size depends on material properties as well as the evaporation conditions [51].

2.6. Reactivity of metal oxides modified carbon nanotubes

Nanostructured transition metal oxides (MO's) possess excellent properties such as high surface area and enhanced chemical/electrochemical activities. They have been widely used for practical applications such as heterogeneous catalysis, sensing, photovoltaics, energy conversion and storage, and optoelectronics. Recent efforts have been suggested that the integration of CNTs and nanostructured transition metal oxides could generate new kinds of nanocomposites with multifunctional properties benefited from each kind of nanostructures [36].

The formation of CNTs-MO hybrids involves the absorption of MO's to the CNT surface or through organic fragments in the case of chemically functionalised CNTs. In general, there are two main pathways for the preparation of CNT-MO hybrids [54]. In the first strategy, pre-formed MO's can be linked to the CNT surface via covalent or weaker bonds. The linkers can be of two types: either functional groups, which may form covalent bonds with functional groups present on the surface [54] or linkers that simply stick to the CNT surface through weak intermolecular interactions such as π-π stacking [55] and/or electrostatic attractions [56], the most common method being incipient-wetness impregnation method [57]. The incipient-wetness impregnation is a well-known technique for preparing heterogenous catalysts-metal precursor dissolved in a volume of solvent equal to the total pore volume of the support is used, and after capillary filling the sample is calcined.

An alternative pathway for the formation of CNT-MO hybrids involves the direct reduction/deposition of the suitable precursor to CNT [58]. Yan *et al.* [59] employed microwave irradiation to synthesise CNT/MnO_2 composites by reduction of potassium permanganate in the presence of CNTs. The method resulted in homogenous dispersion of MnO_2 on the surface of CNT. Lang *et al.* [37] prepared cobalt oxide/MWCNTs composites by a facile chemical co-precipitation method for supercapacitors using $CoCl_2.6H_2O$ as the cobalt oxide precursor. They demonstrated that the electrical conductivity of the material was improved as a result of the interaction between the two materials. Su *et al.* [60] synthesised a hierarchical porous architecture consisting of NiO nanoflakes and MWCNTs composite by refluxing and post-annealing as advanced pseudocapacitor materials. The material showed excellent stability after 300 cycles.

Xu *et al.* [61] prepared NiO/MWCNTs nanocomposites using a large scale direct thermal decomposition method using $Ni(NO_3)_2 \cdot 6H_2O$ as the NiO precursor. The authors demonstrated that the as prepared NiO nanoparticles are uniformly coated onto the surface of MWCNTs. They further showed that the direct thermal decomposition method is a versatile route for preparing carbon nanotube-inorganic hybrid electrode materials. Abbas *et al.* [62] anchored functionalised CNTs with mesoporous Co_3O_4 nanoparticles by a facile chemical co-precipitation method. They demonstrated that CNTs not only enhance the conductivity of Co_3O_4 nanoparticles but also improve the structure stability of Co_3O_4 nanoparticles. Furthermore, the mesoporous structure of Co_3O_4 nanoparticles is available for electrolyte transfer.

Ball milling is another method to make CNT metal oxide composites. It can be simply explained as the process where a powder mixture placed in a ball mill is subjected to high-energy collision from the balls. It was found that this method, termed mechanical alloying, could successfully produce fine, uniform dispersions of oxide particles. This innovation has changed the traditional method in which production of materials is carried out by high temperature synthesis. During the high-energy ball milling process, the powder particles are subjected to high energetic impact [56].

2.7. Structural characterisation of carbon nanotubes and metal oxides nanoparticles

2.7.1. X-ray diffraction

X-ray diffraction (XRD) is a technique that is used to provide information about the atomic structure of crystalline substances. X-rays focused on a sample fixed on the axis of the spectrometer are diffracted by the sample. The changes in the diffracted X-ray intensities are measured, recorded and plotted against the rotation angles of the sample. Computer analysis of the peak positions and intensities associated with this pattern enables qualitative analysis, lattice constant determination and/or stress determination of the sample. Qualitative analysis may be conducted on the basis of peak height or peak area. The peak angles and profiles may be used to determine particle diameters and degree of crystallinity [63].

The Scherrer formula (eq. 2.1) below can be used to determine the crystallite size of materials:

(Equation 2.1)

$$t = \frac{k\lambda}{B\cos\theta}$$

Where;

t is the crystallite size in nm, λ is the wavelength of the X-ray radiation (CuK$_\alpha$ = 0.15406 nm), k is a constant taken as 0.94, θ is the diffraction angle in degrees and B is the line width at half maximum height (degrees). The Scherrer equation explains peak broadening in terms of incident beam divergence which makes it possible to satisfy the Bragg condition for non-adjacent diffraction planes. Crystallite size can also cause peak broadening. The crystallite size is easily calculated as a function of peak width (specified as the full width at half maximum peak intensity (FWHM)), peak position and wavelength [63].

2.7.2. Transmission electron microscopy

Transmission electron microscopy (TEM) is used to characterise the structure of materials with very high spatial resolution. Information about the morphology, crystal

structure and defects, crystal phases, composition and magnetic microstructure can be obtained by a combination of electron-optical imaging, electron diffraction and small probe capabilities. It uses a high energy electron beam transmitted through a very thin sample to image and analyse the microstructure of materials with atomic scale resolution [64].

2.7.3. Scanning electron microscopy

Scanning electron microscopy (SEM) is used to reveal information about the sample including external morphology, chemical composition, crystalline structure and orientation of materials making up the sample. It uses a focused beam of high-energy electrons to generate a variety of signals at the surface of the solid sample. Secondary electrons are most valuable for showing morphology and topography on samples and backscattered electrons are most valuable for illustrating contrasts in composition in multiphase samples (i.e. for rapid phase discrimination) [65].

2.7.4. Fourier transform infrared spectroscopy

Fourier-transform infrared spectroscopy (FTIR) is used to obtain information on the molecular structure of all type of samples (solid, liquid or gas). It is the absorption measurement of different IR frequencies by a sample positioned in the path of an IR beam [66]. IR radiation causes the excitation of the vibrations of covalent bonds within the molecule, these vibrations include the stretching and bending modes. The main goal of IR spectroscopic analysis is to determine chemical functional groups in samples. Different functional groups absorb characteristic frequencies of IR radiation [67]. IR absorption information is generally presented in the form of a spectrum with wavelength or wavenumber as the x-axis and absorption intensity or percent transmittance as the y-axis [66].

2.7.5. Raman spectroscopy

Raman spectroscopy (RMS) is a spectroscopic technique based on inelastic scattering of monochromatic light, usually from a laser source. Inelastic scattering means that the frequency of photons in monochromatic light changes upon

interaction with a sample. Photons of the laser light are absorbed by the sample and then re-emitted. Frequency of the re-emitted photons is shifted up or down in comparison with original monochromatic frequency, which is called the Raman effect. This shift provides information about vibrational, rotational and other low frequency transitions in molecules. Raman spectroscopy can be used to study solid, liquid and gaseous samples [68].

The vibrational states probed by Raman spectroscopy are similar to those involved in infrared spectroscopy. However, the two vibrational spectroscopy techniques are complementary, in that vibrations that are strong in an infrared spectrum (those involving strong dipole moments) are typically weak in a Raman spectrum. Likewise, non-polar functional group vibrations that give very strong Raman bands usually result in weak infrared signals [69]. Raman spectroscopy provides key information about the structure of molecules. The position and intensity of features in the spectrum reflect the molecular structure and can be used to determine the chemical identity of the sample. Spectra may also show subtle changes depending on the crystalline form [70].

A typical Raman spectra of as-received and acid-treated CNTs is shown in figure 2.2. The Raman spectroscopy is very sensitive to variation of structural disorder in graphitic materials [71, 72]. The Raman spectra of graphite are compounded by four main bands, designed: D ($\sim$1352 cm^{-1}), G ($\sim$1582 cm^{-1}), D$'$ ($\sim$1600 cm^{-1}) and G$'$ ($\sim$2700 cm^{-1}), when excited by the 514.5 nm wavelength of an Ar laser [73]. The intensity of band D represents the existence of defects and other effects induced by any type of carbon [74]. Generally, a ratio between the intensities of G and D bands (I_D/I_G) is used to evaluate the disorder degree of graphitic materials. An increase in I_D/I_G corresponds to a higher proportion of sp^3 carbon that is usually attributed to the presence of more structural defects [75]. G$'$ band with high intensity is an indicative of high ordered nanographites, compounded by few graphene sheets or 3D structures with defects on lattice parameter by curvature effect [76, 77]. All bands become narrower after oxidation on figure 2.2 which emphasizes the total corrosion of any amorphous carbon.
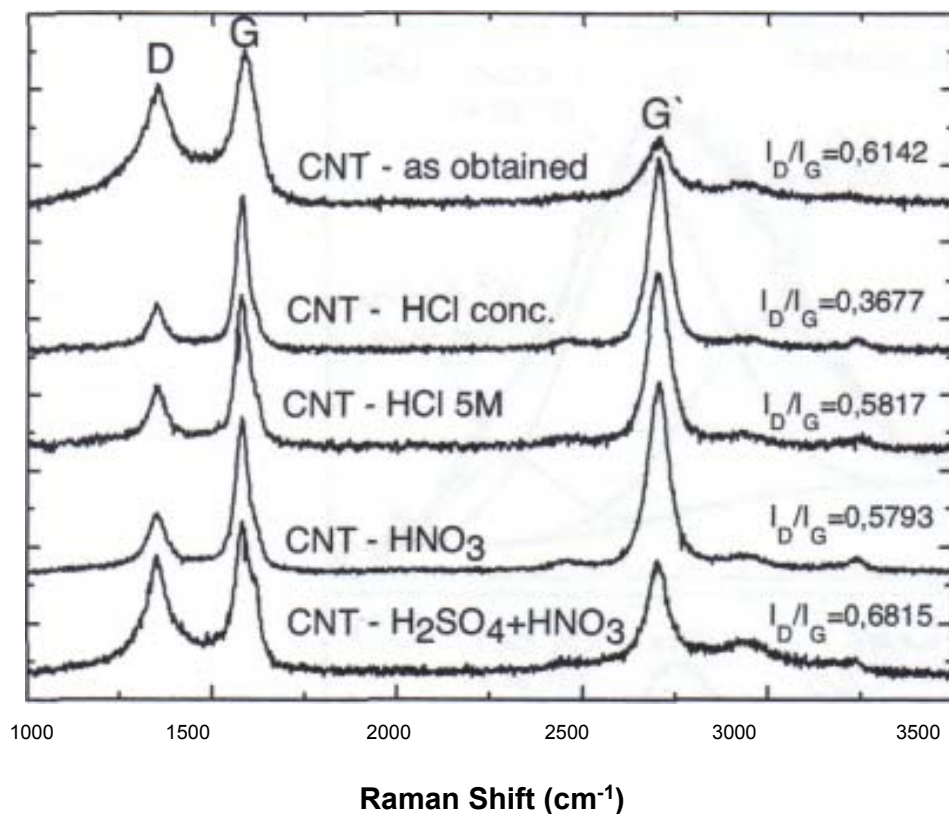
Figure 2.2: Raman spectra of CNT treated at different acidic conditions in comparison to as-obtained CNT [78].

2.7.6. Brunauer-Emmett-Teller analysis

Brunauer-Emmett-Teller (BET) analysis provides precise specific surface area evaluation of materials by nitrogen multilayer adsorption measured as a function of relative pressure. The technique encompasses external area and pore area evaluations to determine the total specific surface area in m^2/g yielding important information in studying the effects of surface porosity and particle size in many applications. Barrett-Joyner-Halenda (BJH) analysis can also be employed to determine pore area and specific pore volume using adsorption and desorption techniques. This technique characterises pore size distribution independent of external area due to particle size of the sample [79].

2.7.7. Thermogravimetric analysis

Thermogravimetric analysis (TGA) measures weight changes in a material as a function of temperature (or time) under a controlled atmosphere. A TGA analysis is performed by gradually raising the temperature of a sample in a furnace as its weight is measured on an analytical balance that remains outside of the furnace [80]. The measurement is normally carried out in air or in an inert atmosphere, such as helium or argon [81]. In TGA, mass loss is observed if a thermal event involves loss of a volatile component.

The weight of the sample is plotted against temperature or time to illustrate thermal transitions in the material, such as loss of solvent and plasticizers in polymers, water of hydration in inorganic materials, and finally, decomposition of the material [80]. A plot of mass change versus temperature (T) is referred to as the thermogravimetric curve (TG curve). For the TG curve, we generally plot mass (m) decreasing downwards on the y axis, and temperature (T) increasing to the right on the x axis. Sometime time (t) is plotted in place of T. TG curve helps in revealing the extent of purity of samples and in determining the mode of their transformations within specified range of temperature [82].

2.8. Hydrogen economy

Fluctuations in the price of crude oil are a major strain to the fossil fuel dominated economy [83]. On the other hand environmental problems (air pollution) associated with the burning of fossil fuels are rapidly increasing [84]. It is widely hoped that the use of carbon-free energy carriers could reverse or decelerate the "greenhouse" phenomenon. The utilisation of sustainable energy resources is predicted to increase exponentially in the coming years [85]. New renewable energy systems include solar energy, wind energy and tidal energy. A major problem associated with several of this renewable energy sources is that they are intermittent and their energy density is low [83]. However, hydrogen has been increasingly recognised as the fuel of the future, due to cleanest and efficient energy carrier with a significantly reduced impact on the environment [86]. Hydrogen is considered as an ideal alternative fuel for many energy converters because of its clean-burning nature, high conversion efficiency, lightweight, zero pollutant emission and potentially abundant production from other renewable resources. One of the main proposed applications of hydrogen is its use as ecologically clean fuel in power transport vehicles and portable electronic devices such as, mobile phones and chargeable/dischargeable electrolytic cells of high energy density [87].

2.8.1. Production of hydrogen

Hydrogen is the most abundant element in the universe [88]. Although it appears to be a possible replacement for fossil fuels, it does not occur as fuel in nature. Rather it occurs in the form of chemical compounds like water or hydrocarbons that must be transformed to yield hydrogen. Unlike petroleum, hydrogen can be easily generated from renewable energy sources with no pollution of any kind. Once produced hydrogen can be stored and used as an energy carrier for both mobile and stationary applications [89]. The following methods are used for the production of hydrogen.

2.8.1.1. Hydrogen from fossil fuels

Hydrogen can be produced from coal (Eq. 2.2), natural gas (Eq. 2.3) and oil (Eq. 2.4) as follows:

$$C + H_2O \longrightarrow CO + H_2 \qquad \text{(Equation 2.2)}$$

$$CH_4 + 2H_2O \longrightarrow CO_2 + 4H_2 \qquad \text{(Equation 2.3)}$$

$$C_{12}H_{24} + 6O_2 \longrightarrow 12CO + 12H_2 \qquad \text{(Equation 2.4)}$$
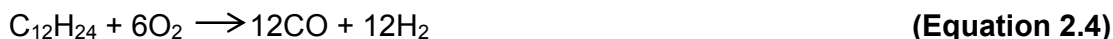
The production of hydrogen from fossil fuels does not reduce the use of fossil fuels but rather shifts them from end use to an earlier production step and it still releases CO_2 to the environment. Thus to achieve the benefits of the hydrogen economy, one must produce hydrogen from non-fossil resources, such as water [83].

2.8.1.2. Hydrogen from water

Methods of producing hydrogen from water includes, among others, electrolysis, photochemical and biochemical processes [83]. Production of hydrogen from water electrolysis is one of the most promising methods, where hydrogen and oxygen are obtained at a theoretical reversible applied potential of 1.23 V, without evolution of any green-house gas [83]. Photocatalytic and photochemical splitting of water are also other possible routes used for the production of hydrogen where sustained energy sources i.e sunlight are used [90]. Microorganisms are used to produce H_2 via either fermentation [89] or photosynthesis, the former being generally preferred because it does not rely on the availability of light sources [83]. Hydrogen can be produced from water as follows:

$$2H_2O \longrightarrow 2H_2 + O_2 \qquad \text{(Equation 2.5)}$$

2.8.2. Methods of storing hydrogen

One of the major technical obstacles in the transition to hydrogen economy is the absence of an affordable and efficient hydrogen storage system. Thus on-going research is focused on the development of advanced hydrogen storage materials [85]. For stationary systems, the weight and volume of the system used for hydrogen storage is not a key factor. However, for mobile applications, hydrogen storage system has to be compact, lightweight and affordable. Stored hydrogen can be used as a fuel in various applications ranging from Proton Exchange Membrane (PEM) fuel cells to rechargeable batteries, used in laptops and cell phones [90]. The

desirable storage capacity for viable commercial exploitation of hydrogen as energy source is at least 6.5 wt.% as postulated by the US Department of Energy (DOE) [91]. Bellow follows the three major technologies for hydrogen storage. However, these technologies either cannot reach the benchmarks just mentioned and/or have significant disadvantages [83].

2.8.2.1. Gaseous hydrogen storage

High pressures are required for the storage of hydrogen in the gas phase. However, the potential risk associated with very high-pressure system is the procedure of compressing hydrogen. This raises important practical problems as there is currently no practical solution to refilling cylinders in a domestic situation to such high pressures rapidly and safely [83].

2.8.2.2. Liquid hydrogen storage

Liquid hydrogen has been used in space technology for several years. This method has less potential risks as compared to the compressed gas in terms of storage pressure. The problem associated with the use of stored liquid hydrogen is the loss of most of the hydrogen due to evaporation since hydrogen liquefies at very low temperatures (20.25 K) [92].

2.8.2.3. Solid hydrogen storage

At present, storage of hydrogen in solid matrices appears to be the appropriate option. This method offers more safety and comfort for transport applications. Solid materials are used to store hydrogen in atomic or molecular form, where hydrogen becomes part of the solid materials through some physicochemical bonding. Metal hydrides; have been traditionally used to store hydrogen in the solid state [83]. Hydrogen forms metal hydrides with some metals and alloys, leading to solid-state storage under moderate temperature and pressure. Hence, the method has important safety advantage over the gas and liquid-storage methods. Metal hydrides have higher hydrogen storage density than hydrogen gas or liquid hydrogen [93]. However, metal hydrides possess the disadvantages of low gravimetric storage

capacity, large weight, and excessive cost of manufacture and high temperatures of decomposition [94-96].

Storage by gas compression, hydrogen liquefaction, or in the form of metal hydrides, possesses severe disadvantages. These drawbacks have induced the study of new storage materials. Adsorption of hydrogen on the surface of porous materials of high surface area is one of the most promising techniques to store hydrogen, with the potential to meet the capacity goals, set by the US Department of energy (DOE) as well as the advantages of low weight and ease of desorption [85]. Materials at nanoscale especially novel carbon materials, such as graphite, activated carbon and carbon nanotubes proves to be promising hydrogen storage materials as they exhibit novel physical and chemical properties and possess nanosize structure. Figures up to 67 wt.% have been claimed as possible storage capacity in carbon materials especially carbon nanotubes [25].

Hydrogen can be adsorbed on carbon nanotubes by physisorption and/or chemisorption [97]. Physisorption (molecular adsorption) takes place when hydrogen maintains its molecular structure and is based on weak van-der-Waals forces that carbon exerts on hydrogen molecules [98]. In physisorption, hydrogen is weakly held and often very high pressures or low temperatures are required. This makes physisorbed materials less attractive for practical applications at ambient temperature [100]. In chemisorption (atomic adsorption) atoms of hydrogen create chemical bonds with the carbon of the nanotubes. The amount of hydrogen stored on/in carbon nanotubes originate from covalent C-H interaction [199]. In chemisorption there is no need to use high pressure and the hydrogen sorption process occurs directly in the electrode material at ambient conditions [100].

2.9. Supercapacitors

Supercapacitors, also called ultracapacitors or electrochemical capacitors, are energy storage devices that continue to attract attention due the their primary advantages of high specific power, high specific capacitance, high charge/discharge rate, excellent reversibility and long cycle life [101-103]. Their specific capacitance and energy density is higher than that of conventional capacitors and they have

greater power densities than batteries [101]. Supercapacitors have been and are further developed for a variety of applications such as in mobile electronic devices, backup power supplies and hybrid electric vehicles [102].

Based on the charge storage mechanism, supercapacitors can be categorised as electrical double-layer capacitors (EDLC's) and pseudocapacitors. EDLC's stores energy using ion adsorption/desorption at the electrode/electrolyte interfaces while the capacitance of pseudocapacitors arises from the fast and reversible Faradaic reactions of electro-active materials in the electrode [103]. The materials for EDLC's usually include carbonaceous materials (carbon nanotubes, graphite, carbon black, etc), that are characterised of high power density but suffer from low capacitance. The transition metal oxides and conducting polymers can offer relatively higher pseudocapacitance but accordingly suffer from low conductivity and poor cyclability [104].

2.10. An overview of electrochemistry

Electrochemistry can be defined as the branch of chemistry that deals with the chemical action of electricity and the production of electricity by chemical reactions. It involves the measurements of potential (potentiometry) or current response (voltammetry). In a cyclic voltammetry experiment, an external potential is applied to the cell and the current response is measured. Precise control of the external applied potential is required and this can be achieved by using a potentiostat and a three electrode system [105].

In a three electrode system, the potential of one electrode (the working electrode) is controlled relative to the reference electrode and the current passes between the working electrode and the third electrode (the auxiliary electrode). A working electrode acts as a source of electrons for exchange with molecules in the solution adjacent to the electrode surface, and must be an electronic conductor. It must also be electrochemically inert over a wide potential range [105].

2.10.1. Two types of electrochemical energy storage in carbon nanotubes

2.10.1.1. Electrochemical hydrogen storage

Because of their cylindrical, hollow geometry and nanometer-scale diameters, carbon nanotubes have been predicted to store atomic hydrogen through chemisorption. Since the report by Dillon *et al.* [106] of a possible 60 wt.% hydrogen storage capacity, much effort has been focused into this material. The cylindrical structures of CNTs led to suggestions that they would be ideal energy storage materials. The large empty space inside the nanotube, the low mass density and their chemical stability opens a new application for the hydrogen storage with high capacities [83].

Haiyan *et al.* [107] studied the electrochemical hydrogen storage of pure MWCNTs with different diameters and obtained the highest hydrogen capacity of 480.6 mAh/g for 60-100 nm CNTs. They demonstrated that hydrogen storage has close connection with the structure of CNTs. The hydrogen molecules can be stored both in the porous hole and between the layers of CNTs. Liu *et al.* [108] studied the electrochemical hydrogen storage of multi-walled carbon nanotubes decorated by TiO_2 nanoparticles by the galvanostatic charge and discharge method. The highest discharge capacity of 540 mAh/g was obtained. The improved discharge capacity of MWCNTs was attributed to the increased effective area for adsorption of hydrogen atoms in the presence of TiO_2 nanoparticles on MWCNTs and the preferable redox ability of TiO_2 nanoparticles.

Reyhani *et al.* [109] studied the hydrogen storage capacity of raw, oxidised, purified and Fe-doped multi-walled carbon nanotubes by electrochemical method. The highest hydrogen storage capacity of 510 mAh/g was obtained for the Fe-doped MWCNTs. Yang *et al.* [110] investigated the electrochemical hydrogen storage properties of Ni nanoparticles coated SWCNT electrodes. The highest electrochemical discharge capacity of 1404 mAh/g was obtained for the SWCNT electrode coated with 8 wt.%Ni nanoparticles. This enhancement of electrochemical hydrogen storage capacity was ascribed to the fact that Ni nanoparticles act as a redox site, thus leading to an improved electrochemical hydrogen storage capacity.

2.10.1.3. Charge storage in supercapacitors

Supercapacitors have a high capacitance and potentially applicable in electronic devices. Typically, they are comprised of two electrodes separated by an insulating material that is ionically conducting in electrochemical devices. The capacity of an electrochemical supercapacitor inversely depends on the separation between the charge on the electrode and the counter charge in the electrolyte. Because this separation is about a nanometre for nanotubes in electrodes, very large capacities result from the high nanotube surface area. In this way, a large amount of charge injection occurs if only a small voltage is applied. This charge injection is used for energy storage in nanotube supercapacitors [25].

Dai *et al.* [23] performed the CV studies of the prepared materials in a 0.1 M H_2SO_4 electrolyte. They found that the specific capacitance increases from 8.9 F/g to 22.6 F/g after treatment (an enhancement of approximately 43.5 %). The reason for the increase in the specific capacitance was attributed to the activated MWCNTs possessing functional groups on the surface which act as active sites for electron transmission. Yan *et al.* [59] studied the electrochemical properties of CNT/MnO_2 by cyclic voltammetry and galvanostatic charge/discharge and obtained the highest specific capacitance of 944 F/g at a scan rate of 1 mV/s. They showed that CNTs provide a direct conductive path for MnO_2 particles, due to their high electric conductivity, thus reducing the internal resistance within the composite itself. They further demonstrated that the inner-tube pores among CNTs also facilitate the rapid transport of the electrolyte ions from bulk solution to the surface of MnO_2.

Ma *et al.* [111] studied the electrochemical properties of MnO_2/CNTs nanocomposite in an organic electrolyte. The birnessite-type MnO_2 was coated uniformly on the CNTs by employing a spontaneous direct redox reaction between the CNTs and MnO_4. The initial specific capacitance of the MnO_2/CNTs nanocomposite was found to be approximately 250 F/g. Fan *et al.* [112] investigated the capacitive behaviour of nickel-cobalt oxides/CNTs electrode by cyclic voltammetry and gavanostatic charge-discharge method in 1 M KOH aqueous solution. Nickel-cobalt oxides/CNTs composites were prepared by adding and thermally decomposing nickel and cobalt

nitrates directly onto the surface of carbon nanotube/graphite electrode. The highest specific capacitance of 569 F/g was obtained at Ni/Co molar ratio = 1:1.

Su *et al.* [60] uses NiO and commercial carbon nanotubes as electrode materials for electrochemical capacitors. The specific capacitance of the electrode materials for 10wt.%, 30wt.% and 50wt.% CNTs are 279, 242 and 112 F/g, respectively in an aqueous 1 M KOH electrolyte. Lang *et al.* [37] investigated the electrochemical properties of cobalt oxide/MWCNTs by cyclic voltammetry, galvanostatic charge/discharge and electrochemical impedance spectroscopy. The highest specific capacitance of 418 F/g at a current density of 0.625 A/g was reported for the Co_3O_4-5%MWCNT composite in 2 M KOH electrolyte.

2.10.2. The solvents and salts appropriate for an electrolytic solutions

The medium must be conducting and this can be achieved by using either a molten salt or an electrolyte solution. An electrolyte solution is made by adding an ionic salt to an appropriate solvent. The salt must become fully dissociated in the solvent in order to generate a conducting solution. The electrolyte solution must also be electrochemically inert over a wide potential range and must be pure. It must also be chemically inert, so that it will not react with any reactive species generated in the experiment. If the temperature is to be varied, the electrolyte solution must have an appropriate liquid range [105].

2.10.3. Voltammetric techniques

In a voltammetric experiment, a potential is applied to a system using two electrodes (a working electrode and a reference electrode), and the current response is measured using the working electrode and a third electrode, the auxiliary electrode. The current arises from transfer of electrons between the energy levels of the working electrode and the molecular energy levels of the system under study. This current is often referred to as the faradaic current. Transfer of electrons from filled electrode orbitals to vacant molecular orbitals is referred as reduction and transfer of electrons from filled molecular orbitals to vacant electrode orbitals is referred to as oxidation [105].

Varying the applied potential changes the oxidising/reducing ability of the electrode. For example, more negative potentials increase the reducing ability of the electrode. Therefore, a common approach in voltammetry experiments is to vary the applied potential, and to record the potential at which a current response is detected. Molecules for which a redox potential can be measured are referred to as electrochemically active. Examples of electrochemically active molecules include organic molecules with extended p-systems (e.g., aromatic molecules) and transition metal complexes. In this study three voltammetric techniques i.e cyclic voltammetry (CV), chronopotentiometry (CP) and controlled potential electrolysis (CPE), were employed [105].

2.10.3.1. Cyclic voltammetry

Cyclic voltammetry (CV) is one of the most commonly used electrochemical techniques, and is based on a linear potential waveform; that is, the potential is changed as a linear function of time. The rate of change of potential with time is referred to as the scan rate. The simplest technique that uses this waveform is linear sweep voltammetry (LSV). The potential range is scanned starting at the Initial potential and ending at the Final potential. CV is an extension of LSV in that the direction of the potential scan is reversed at the end of the first scan (the first switching potential), and the potential range is scanned again in the reverse direction. The potential can be cycled between the two switching potentials for several cycles before the experiment is ended at the final potential [105].

2.10.3.2. Chronopotentiometry

The galvanostat uses a three electrode configuration, in which a current is applied between the auxiliary and working electrodes, and the potential of the working electrode (measured with respect to the reference electrode) is monitored. The basis of controlled current experiments is that a redox (electron transfer) reaction must occur at the surface of the working electrode in order to support the applied current. Chronopotentiometry (CP) is the most basic constant current experiment. In CP, a current step is applied across an electrochemical cell without stirring and the potential is monitored. [105].

2.10.3.3. Controlled potential electrolysis

The principle behind the controlled potential electrolysis (CPE) experiment is very simple. If only the oxidized species is initially present, then the potential is set at a constant value sufficiently negative to cause rapid reduction and is maintained at this value until only the reduced species is present in solution. The total charge passed during the CPE experiment (Q) is calculated by integrating the current and is related to the number of electrons transferred per molecule (n) and the number of moles of the oxidized species initially present (N) through Faraday's law [105]:

$$Q = nFN \hspace{4cm} \textbf{(Equation 2.6)}$$

2.10.4. Mass transport processes

In an electrochemical cell, mass transport is a process which governs the net movement of ions, charge or neutral species across the electrode-electrolyte interface [113]. Below follows the three mass transport processes.

2.10.4.1 Diffusion

Diffusion is a spontaneous movement under the influence of concentration gradient, i.e., the process in which there is movement of a substance from an area of high concentration, aimed at maintaining concentration differences. If the potential at an electrode oxidises or reduces an analyte, its concentration at the electrode surface will be lowered and therefore, more analyte moves to the electrode from bulk of the solution, which makes it the main current-limiting factor in voltammetric process [114].

2.10.4.2. Migration

Migration is the type of charge transport involving movement of charged particles along an electrical field (i.e., the charge is carried through the solution by ions according to their transference number). Controlled-potential experiments require a supporting electrolyte to decrease the resistance of a solution and eliminate electron-migration effects to maintain a constant ionic strength [114].

2.10.4.3. Convection

It is the transport of changes to the electrode by a gross physical movement, such as fluid flow occurs by stirring or flowing the solution and by rotating or vibrating the electrode (i.e. forced convection) or because of density gradient (i.e. natural convection). The effect is eliminated during voltammetry experiment by maintaining the cell under quiet and stable condition [114].

2.10.5. Working electrodes commonly used in electrochemistry

Carbon electrodes such as the glassy carbon and pyrolytic graphites electrode have long been recognised as versatile and supporting platforms, for electrocatalysis and electrochemical sensing. They both have numerous advantages such as low cost, chemical inertness and wide potential window in most electrolyte solutions over the precious metal electrodes such as gold, platinum, aluminium, silver and copper. Glassy carbon is an amorphous form of carbon and is mechanically more durable than pyrolytic graphite. Pyrolytic graphite has a more ordered structure, with distinct planes, the basal plane and the edge plane. The edge plane is considerably more conducting than the basal plane [105].

2.10.6. Electrode modification techniques

Various techniques can be used to modify working electrodes, these techniques include; Electrodeposition, electropolymerisation, dip-dry, drop-dry, spin coating and composite technique. Electrodeposition is a plating process that uses electrical current to reduce cations of a desired material from a solution and a conductive object with a thin layer of the material, such as a metal. Both the anode and the cathode components are immersed in an electrolyte containing one or more dissolved metal salts as well as other ions that permit the flow of electricity [83].

Electropolymerisation is the most efficient method of depositing polymer films on electrodes. The process involves the repetitive voltammetric scanning of the solution of the modifier monomers at the electrode surface within a specific potential window [69]. The dip-dry method involves the immersion of an electrode in solution of a

catalyst or a modifier for a period of time to allow the surface adsorption of the material. The electrode is later withdrawn and the solvent is allowed to dry [115]. During the drop-dry method the electrode is modified by placing few drops of the catalyst or modifier on its surface and allowing the solvent to dry off [116]. Spin coating involves evaporation of solution of a modifier from electrode surface by high speed rotations using centrifugal force [117]. Composite technique is a process of impregnating the bulk electrode material with a chemical modifier [118].

2.11. References

[1] Iijima S, Atoms in carbon cages: The structure and properties of endohedral fullerenes, Nature 354 (1991) 56-60

[2] Yang Q.H and Chang H.M, Carbon nanotubes: surface, porosity and related applications, Carbon Nanotechnology 12 (2006) 323-324

[3] Chiao K, Carbon nanotubes for hydrogen storage, Physics Letters A 30 (2002) 1-14

[4] Hermosilla-Lara G, Momen G, Marty P.H, Le Neindre B and Hassouni K, Hydrogen storage by adsorption on activated carbon: Investigation of the thermal effects during the charging process, International Journal of Hydrogen Energy 32 (2007) 1542-1553

[5] Joselevich E, Dai H, Liu J, Hata K and Windle A. H, Carbon nanotube synthesis and organisation, Applied Physics 111 (2008) 101-164

[6] Liu Y, Gao L, Sun J, Zheng S, Jiang L, Wang Y, Kajiura H, Li Y and Noda K. A, Multi-step strategy for cutting and purification of single-walled carbon nanotubes, Carbon 45 (2007) 1972-1978

[7] Wang Y, Gao L, Sun J, Liu Y, Zhang S, Kajura H, Li Y and Noda K, An integrated route for purification, cutting and dispersion of singled-walled carbon nanutubes, Chemical Physics letters 432 (2006) 205-208

[8] Vukovic G, Marinkovic A, Obradovic M, Radmilovic V, Colic M, Aleksic R and Uskokovc P.S, Synthesis, characterization and cytotoxicity of surface amino functionalized water-dispersible multi-walled carbon nanotubes, Applied Surface Science 255 (2009) 8067-8075

[9] Naseh M.V, Khodadadi A. A, Mortazavi Y, Sahraei O.A, Pourfayaz F and Sedghi S. M, Functionalisation of carbon nanotubes using nitric acid oxidation and DBD plasma M, International Journal of Chemical and Biological Engineering 2 (2009) 66-68

[10] Chiang Y, Lin W and Chang Y, The influence of treatment duration on multi-walled carbon nanotubes functionalized by H_2SO_4/HNO_3 oxidation, Applied Surface Science 257 (2011) 2401-2410

[11] Cuentas-Gallegos A.K, Martínez-Rosales R, Rincón M.E, Hirata G.A and Orozco G, Design of hybrid materials based on carbon nanotubes and polyoxometalates, Optical Material 29 (2006) 126-133

[12] Moreno-Castilla C, Carrasco-Marin F, Maldonado-Hodar F.J and Rivera-Utrilla J, Effects of non-oxidant and oxidant acid treatments on the surface properties of an activated carbon with very low ash content, Carbon 36 (1998) 145-151

[13] Haydar S, Moreno-Castilla C, Ferro-García M.A, Carrasco-Marín F, Rivera-Utrilla J, Perrard A and Joly J.P, Regularities in the temperature-programmed desorption spectra of CO_2 and CO from activated carbons, Carbon 38 (2000) 1297-1308

[14] Xing Y, Li L, Chusuei C.C and Hull R.V, Sonochemical oxidation of multiwalled carbon nanotubes, Langmuir 21 (2005) 4185-4190

[15] Lu C and Chiu H, Chemical modification of multiwalled carbon nanotubes for sorption of Zn^{2+} from aqueous solution, Chemical Engineering Journal 139 (2008) 462-468

[16] Ötvös G, Onyestyák A, Hance I and Kiricsi L.V.C, Rees, surface oxygen complexes as governors of neopentane sorption in multiwalled carbon nanotubes, Carbon 44 (2006) 1665-1672

[17] Dong C, Campell A.S, Eldawud R, Perhinschi G, Rojanasakul Y and Din C.Z, Effects of acid treatment on structure, properties and biocompatibility of carbon nanotubes, Applied Surface Science 264 (2013) 261-268

[18] Ebbesen T. W, Ajayan P. M, Hiura H and Tanigaki K, Purification of nanotubes, Nature 367 (1994) 519-519

[19] Borowiak-palen E, Pichler T, Liu X, Knupfer M, Graff A, Jost O, Pompe W, Kalenczuk R.J and Fink J, Reduced diameter distribution of single-wall carbon nanotubes by selective oxidation, Chemical Physics Letters 363 (2002) 567-572

[20] Farkas E, Anderson M. E, Chen Z. H and Rinzler A.G, Length sorting cut single wall carbon nanotubes by high performance liquid chromatography, Chemical Physics Letters 363 (2002) 111-116

[21] Reyhani A, Golikand A. N, Mortazavi S. Z, Irannejad L and Moshfegh A. Z, The effects of multi-walled carbon nanotubes graphitisation treated with different atmospheres and electrolyte temperatures on electrochemical hydrogen storage, Electrochimica Acta 55 (2010) 4700-4705

[22] Mazov I, Kuznetsov L.V, Simonov I. A, Stadnichenko A.I, Ishchenko A.V, Romanenko A. I, Tkachev E.N and Anikeeva O.B, Oxidation behavior of multiwall carbon nanotubes with different diameters and morphology, Applied Surface Science 258 (2012) 6272-6280

[23] Dai Y, Liu W, Pan T and Jehng J, Surface activation on multi-wall carbon nanotube for electrochemical capacitor applications, Applied Surface Science 258 (2012) 3027-3032

[24] Shirazi Y, Tofighy M.A, Mohammadi T and Pak A, Effects of different carbon precursors on synthesis of multiwall carbon nanotubes: Purification and functionalisation, Applied Surface Science 257 (2011) 7359-7367

[25] Daenen M, 2003, De Fouw R.D, Hamers B, Janssen P.G.A, Schouteden K and Veld M.A.J, The wondrous world of carbon nanotubes: A review of current carbon nanotubes technologies, Multidisciplinary Project Group, Eindhoven University of Technology, Eindhoven

[26] Niyogi S, Hamon M. A, Hu H, Zhao B, Bhowmik P, Sen R, Itkis M.E and Haddon R.C, Chemistry of single-walled carbon nanotubes, Accounts of Chemical Research 35 (2002) 1105-1113

[27] Avouris P, Carbon nanotube electronics, Chemical Physics 281 (2002) 429-444

[28] Damnjanovic M, Milosevic I, Vukovic T and Slavonic R, Full symmetry, optical activity and potentials of single- and multi- wall nanotubes, Physical Review B 60 (1999) 2728-2739

[29] Atkins P and De Paula J, 2006, Physical Chemistry 8th edition, United States and Canada: W.H. Freeman and Company

[30] Noguera C, 1996, Physics and chemistry at oxide surfaces, Cambridge United Kingdom: Cambridge University Press

[31] Gleiter H, Nanostructured Materials: Basic concepts, microstructure and properties, Institute for Nanotechnology 6 (1995) 3

[32] Yan J, Zhou H, Yu P, Su L and Mao L, A general electrochemical approach to deposition of metal hydroxide/oxide nanostructures onto carbon nanotubes, Electrochemistry Communications 10 (2008) 761-765

[33] Cao Z and Wei B, High rate capability of hydrogen annealed iron oxide-single walled carbon nanotube hybrid films for lithium-ion batteries, ACS Applied Materials and Interface 5 (2013) 10246-10252

[34] Tartaj P and Amarilla J.M, Iron oxide porous nanorods with different textural properties and surface composition: Preparation, characterisation and electrochemical lithium storage capabilities, Journal of Power Sources 196 (2011) 2164-2170

[35] Xie K, Li J, Lai Y, Lu W, Zhang Z, Liu Y, Zhou L and Huang H, Highly ordered iron oxide nanotube arrays as electrodes for electrochemical energy storage, Electrochemistry Communications 13 (2011) 657-660

[36] Adekunle A.S, Agboola B.O, Pillay J and Ozoemena K.I, Electrocatalytic detection of dopamine at single-walled carbon nanotubes–iron(III) oxide nanoparticles platform, Sensors and Actuators B 148 (2010) 93-102

[37] Lang J, Yan X and Xue Q, Facile preparation and electrochemical characterisation of cobalt oxide/multi-walled carbon nanotube composites for supercapacitors, Journal of Power Sources 196 (2011) 7841-7846

[38] Salimi A, Mamkhezri H, Hallaj R and Soltanian S, Electrochemical detection of trace amount of arsenic(III) at glassy carbon electrode modified with cobalt oxide nanoparticles, Sensors and Actuators B 129 (2008) 246-254

[39] Xie L, Wu J, Chen C, Zhang C, Wan L, Wang J, Kong Q, Lv C, Li K and Sun G, A novel asymmetric supercapacitor with an activated carbon cathode and a reduced graphene oxide cobalt oxide nanocomposite anode ,Journal of Power Sources 242 (2013) 148-156

[40] Deng J, Kang L, Bai G, Li Y, Li P, Liu X, Yang Y, Gao F and Liang W, Solution combustion synthesis of cobalt oxides (Co_3O_4 and Co_3O_4/CoO) nanoparticles as supercapacitor electrode materials, Electrochimica Acta 132 (2014) 127-135

[41] Nam K, Kima K, Lee E, Yoon W and Yang X, Pseudocapacitive properties of electrochemically prepared nickel oxides on 3-dimensional carbon nanotube film substrates, Journal of Power Sources 182 (2008) 642-652

[42] Inandar A.I, Kim Y, Pawar S.M, Kim J.H, Im H and Kim H, Chemically grown, porous, nickel oxide thin-film for electrochemical supercapacitors, Journal of Power Sources 196 (2011) 2393-2397

[43] Pendashteh A, Mousavia M.F and Rahmanifar M.S, Fabrication of anchored copper oxide nanoparticles on graphene oxide nanosheets via an electrostatic coprecipitation and its application as supercapacitor, Electrochimica Acta 88 (2013) 347-357

[44] Dubal D.P, Gund G.S, Holze R and Lokhande C.D, Mild chemical strategy to grow micro-roses and micro-woolen like arranged CuO nanosheets for high performance supercapacitors, Journal of Power Sources 242 (2013) 687-698

[45] Gao P, Chen Y, Lv H, Li X, Wang Y and Zhang Q, Synthesis of CuO nanoribbon arrays with noticeable electrochemical hydrogen storage ability by a simple

precursor dehydration route at lower temperature, International Journal of Hydrogen Energy 34 (2009) 3065-3069

[46] Chou S.L, Wang J.Z, Chew S, Liu H.K and Dou S.X, Electrodeposition of MnO_2 nanowires on carbon nanotube paper as free-standing, flexible electrode for supercapacitors, Electrochemistry Communications 10 (2008) 1724-1727

[47] Qinghua H, Xianyou W and Jun L, Characterisation and performance of hydrous manganese oxide prepared by electrochemical method and its application for supercapacitors, Electrochimica Acta 52 (2006) 1758-1762

[48] Donne S.W, Hollenkamp A.F and Jones B.C, Structure, morphology and electrochemical behaviour of manganese oxides prepared by controlled decomposition of permanganate, Journal of Power Sources 195 (2010) 367-373

[49] Staiti P and Iufruno F, Study and optimisation of manganese oxide-based electrodes for electrochemical supercapacitors, Journal of Power Sources 187 (2009) 284-289

[50] D´Souza L and Richards R, Synthesis of metal-oxide nanoparticles: Liquid-solid transformations in "Synthesis, properties and applications of oxide nanoparticles" (Rodríguez, J.A., Fernández-García, M; Eds.). Whiley: N. J, 2007, Chapter 3

[51] Gordon W.O, Metal oxide nanoparticles: Optical properties and interaction with chemical warfare agent simulants

[52] Interrante L.V and Hampen-Smith M.J, 1998, Chemistry of advanced materials: An overview, While-VCH: New York

[53] Uskokovick V and Drofenik M, Synthesis of Materials within reverse micelles, Surface Review and Letters 12 (2005) 39-277

[54] Tsoufis T, Tomou A, Gournis D, Douvalis A. P, Panagiotopoulos I and Kooi B, Novel nanohybrids derived from the attachment of fept nanoparticles on carbon nanotubes, Journal of Nanotechnology 8 (2008) 5942-5951

[55] Georgakilas V, Tzitzios V, Gournis D and Petridis D, Attachment of magnetic nanoparticles on carbon nanotubes and their soluble derivatives, Journal of Material Chemistry 17 (2005) 1613-1617

[56] Correa-duarte M. A, Grzelczak M, Salgueirino-maceira V, Giersig M, Liz-marzan L. M and Farle M, Sierazdki K and Diaz R, Alignment of carbon nanotubes under low magnetic fields through attachment of magnetic nanoparticles, Journal Physical Chemistry B 109 (2005) 19060-19063

[57] Haber J, Block J.H and Delmon B, Manual of methods and procedures for catalyst characterization, Pure and Applied Chemistry 67 (1995) 1257-1306

[58] Jia B, Gao L and Sun J, Self-assembly of magnetite beads along multiwalled carbon nanotubes via a simple hydrothermal process, Carbon 45 (2007) 1476-1481

[59] Yan J, Fan Z, Wei T, Cheng J, Shao B, Wang K, Song L and Zhang M, Carbon nanotubes/MnO_2 composites synthesized by microwave-assisted method for supercapacitors with high power and energy densities, Journal of Power Sources 194 (2009)1202-1207

[60] Su A.D, Zhang X, Rinaldi A, Nguyen S.T, Liu H, Lei Z and Lu L, Hierarchical porous nickel-carbon nanotubes as advanced pseudocapacitor materials for supercapacitors, Chemical Physics Letters 561-562 (2013) 68-73

[61] Xu C, Li B, Du H, Kang F and Zeng Y, Electrochemical properties of nanosized hydrous manganese dioxide synthesized by self-reacting microemulsion method, Journal of Power Sources 180 (2008) 664-670

[62] Abbas S.M, Hussain S.T, Ali S and Ahmad N, Synthesis of carbon nanotubes anchored with mesoporous Co_3O_4 nanoparticles as anode material for lithium-ion batteries, Electrochimica Acta 105 (2013) 481-488

[63] Bish D.L and Post J.E, 1989, Modern powder diffraction, Mineralogical society of America, Washington DC

[64] Egerton R.F, Electron energy-loss spectroscopy in the electron microscope

[65] Brundle C.R, Evans Jr C.A and Wilson S, Encyclopedia of materials characterisation, Butterworth-Heinemann

[66] Sherman Hsu C.P, Handbook of instrumental techniques for analytical chemistry, Separation sciences and product development, Mallinckrodt, Inc, Mallinckrodt baker divison

[67] Gunzler H and Gremlich H.U,2002, IR spectroscopy: An introduction, Weinheim Germany: Wiley VCH

[68] Priceton Instruments, Raman spectroscopy basics

[69] Part of Thermo Fischer Scientific, Introduction to Raman spectroscopy

[70] Harris D.C and Bertolucci M.D, 1978, Symmetry and spectroscopy: an introduction to vibrational and electronic spectroscopy, Oxford University Press

[71] Flahaut E, Laurent C and Peigney A, Catalytic CVD synthesis of double and triple-walled carbon nanotubes by the control of the catalyst preparation, Carbon 43 (2005) 375-383

[72] Okamoto A and Shinohara H, Control of diameter distribution of single-walled carbon nanotubes using the zeolite-CCVD method at atmospheric pressure, Carbon 43 (2005) 431-436

[73] Antunes E.F, Lobo A.O, Corat E.J, Trava-Airoldi V.J, Martin A.A and Veríssimo C, Comparative study of first- and second-order Raman spectra of MWCNT at visible and infrared laser excitation, Carbon 44 (2006) 2202-2211

[74] Lee S, Peng J.-W and Liu C.-H, Raman study of carbon nanotube purification using atmospheric pressure plasma, Carbon 46 (2008) 2124-2132

[75] Ebbesen T.W and Takada T, Topological and sp^3 defect structures in nanotubes, Carbon 33 (1995) 973-978

[76] Antunes E.F, Lobo A.O, Corat E.J and Trava-Airoldi V.J, Influence of diameter in the Raman spectra of aligned multi-walled carbon nanotubes, Carbon 45 (2007) 913-921

[77] Barro E.B, De Souza Filho A.G, Hyungbin S.O.N and Dresselhaus M.S, G′ band Raman lineshape analysis in graphitic foams, Vibrational Spectroscopy 45 (2007) 122-127.

[78] Edwards E.R, Antunes E.F, Botelho E.C, Baldan E.C and Corat E.J, Evaluation of residual iron in carbon nanotubes purified by acid treatments, Applied Surface Science 258 (2011) 641-648

[79] Sing K.S.W, Reporting physisorption data for gas/solid systems, Pure and Applied Chemistry 54 (1982) 2201-2218

[80] Willard H.H , Merrit Jr. L.L, Dean J.A and Settle Jr. F.A, 1986, Instrumental method of analysis, Wadsworth publishing company , USA

[81] Brown M.E, 2001, Introduction to thermal analysis, Kluwer academic publisher, London

[82] Duval C, 1962, Inorganic thermogravimetric analysis, Elsevier Amsterdam

[83] Sankaran M, On the potential of carbon materials for solid state hydrogen storage, Indian Institude of Technology Madras (2006) 1-203

[84] Hui-Ming C, Quan-Hong Y and Chang L, Hydrogen storage in carbon nanotubes, Carbon 39 (2001) 1447-1454

[85] Orinakovia R and Orinak A, Recent applications of carbon nanotubes in hydrogen production and storage, Fuel 90 (2011) 3123-3140

[86] Gayathri V, Devi N. R and Geetha R, Hydrogen storage in coiled carbon nanotubes, International Journal of Hydrogen Energy 35 (2010) 1313-1320

[87] Zhang H, Fu X, Chen Y, Yi S, Li S and Zhu Y, The electrochemical hydrogen storage of multi-walled carbon nanotubes synthesized by chemical vapour deposition using a lanthanum nickel hydrogen storage alloy as catalyst, Physica B 352 (2004) 66-72

[88] Wendt H, Thermochemical hydrogen production, International Journal of Hydrogen Energy 12 (1987) 291-295

[89] Fumiaki T, Chang J. D, Mizukami N, Tatsuo S. T and Katsushige H, Continuous hydrogen production by clostridium sp.strain no. 2 from cellulose hydrolysate in an aqueous two-phase system, Journal of Fermentation and Bioengineering 82 (1996) 80-83

[90] Litcht S, Wang B, Mukerjee S, Soga T, Umeno M and Tributsch H, Over 18% solar energy conversion to generation of hydrogen fuel; theory and experiment for efficient solar water splitting, International Journal of Hydrogen Energy 26 (1999) 653-659

[91] U.S. Department of Energy, Multi-Year Research, development and demonstration Plan: Planned program activities for 2003-2010,http://www.eere.energy.gov/hydrogenandfuelcells/mypp/ (Aug. 2005).5

[92] Sheriff S. A, Zeytinoglu N and Veziroglu T. N, Liquid hydrogen: potential, problems and a proposed research program, International Journal of Hydrogen Energy 22 (1997) 683-688

[93] Inman S, El-Gindy M and Haworth D.C, Hybrid electric vehicles technology and simulation: literature review, International Journal Heavy Vehicle Systems 10 (2003) 167-183

[94] Greenwood N. N and Earnshaw A, 1997, Chemistry of the elements, Boston: Butterworth-heinemann

[95] Reddy A. L. M and Ramaprabhu S, Design and fabrication of carbon nanotube-based microfuel cell and fuel cell stack coupled with hydrogen storage device, International Journal Hydrogen Energy 32 (2007) 4272-4280

[96] Eberle U, Arnold G and Helmholtz R. V, Hydrogen storage in metal–hydrogen systems and their derivatives, Journal of Power Sources 154 (2006) 456-460

[97]   Ioannatos G. E and Verykios X. E, H_2 storage on single- and multi-walled carbon nanotubes, International Journal of Hydrogen Energy 35 (2010) 622-628

[98]   Shaijumon M. M and Ramaprabhu S, Studies of yield and nature of carbon nanostructures synthesized by pyrolysis of ferrocene and hydrogen adsorption studies of carbon nanotubes, International Journal of Hydrogen Energy 30 (2005) 311-317

[99]   Darkrim F.L, Malbrunot P and Tartaglia G.P, Review of hydrogen storage by adsorption in carbon nanotubes, International Journal of Hydrogen Energy 27 (2002) 193-202

[100] Wang D.W, Li F, Liu M, Lu G.Q and Cheng H.M, 3D aperiodic hierarchical porous graphitic carbon material for high-rate electrochemical capacitive energy storage, Angewandte Chemie-International Edition 47 (2008) 373-376

[101] Zhang Y, Li J, Kang F, Gao F and Wang X, Fabrication and electrochemical characterization of two-dimensional ordered nanoporous manganese oxide for supercapacitor applications, International Journal of Hydrogen Energy 37 (2012) 860-866

[102] Zhang Y, Li G, Lv Y, Wang L and Zhang A, Electrochemical investigation of MnO_2 electrode material for supercapacitors, International Journal of Hydrogen Energy 36 (2011) 11760-11766

[103] Xu M, Jia W, Bao S, Su Z and Dong B, Novel mesoporous MnO_2 for high-rate electrochemical capacitive energy storage, Electrochimica Acta 55 (2010) 5117-5122

[104] Wang G, Zhang B, Yu Z and Qu M, Manganese oxide/MWCNTs composite electrodes for supercapacitors, Solid State Ionics 176 (2005) 1169-1174

[105] Instruction manual for bas epsilon for electrochemistry, version 1.60.70 (2000-2004) bioanalytical systems

[106] Dillon A.C, Jones K.M, Bekkedahl T.A, Kiang C.H, Bethune D.S and Heben M.J, Storage of hydrogen in single-walled carbon nanotubes, Nature 386 (1997) 377-379

[107] Haiyan Z, Xiaojuan F, Jianfeng Y, Chun Z, Yiming C, Minghu I and Aixiang W, The effect of MWNTs with different diameters on the electrochemical hydrogen storage capability, Physics Letters A 339 (2005) 370-377

[108] Liu E, Wang J, Li J, Shi C, He C and Du X, Enhanced electrochemical hydrogen storage capacity of multi-walled carbon nanotubes by TiO_2 decoration, International Journal of Hydrogen Energy 36 (2011) 6739-6743

[109] Reyhani A, Mortazavi S.Z, Moshfegh A.Z, Golikand A.N and Amiri M, Enhanced electrochemical hydrogen storage by catalytic Fe-doped multi-walled carbon nanotubes synthesized by thermal chemical vapour deposition, Journal of Power Sources 188 (2009) 404-410

[110] Yang C.-C, Li Y.J and Chen W, Electrochemical hydrogen storage behaviour of single-walled carbon nanotubes (SWCNTs) coated with Ni nanoparticles, International Journal of Hydrogen Energy 35 (2010) 2336-2343

[111] Ma S, Nam K, Yoon W, Yang X, Ahn K, Oh K and Kim K, Electrochemical properties of manganese oxide coated onto carbon nanotubes for energy-storage applications, Journal of Power Sources 178 (2008) 483-489

[112] Fan Z, Chen J, Cui K, Sun F, Xu Y and Kuang Y, Preparation and capacitive properties of cobalt–nickel oxides/carbon nanotube composites, Electrochimica Acta 52 (2007) 2959-2965

[113] Baughman R.H, Zakhidov A.A and De Heer W.A, Carbon nanotubes-the route toward applications, Science 297(2002) 787-792

[114] Skoog D.A, West D.M, Holler F.J and Crouch S.R, 2004, Fundamentals of Analytical Chemistry 8

[115] Abbaspour A, Khajehzadeh A and Ghaffarinejad A, Electrocatalytic oxidation and determination of hydrazine on nickel hexacyanoferrate nanoparticles-modified carbon ceramic electrode, Journal of Electroanalytical Chemistry 631 (2009) 52-57

[116] Jafarian M, Mahjani M.G, Heli H, Gobal F, Khajehsharifi H and Hamedi M. H, A study of the electro-catalytic oxidation of methanol on a cobalt hydroxide modified glassy carbon electrode, Electrochimica Acta 48 (2003) 3423-3429

[117] Wang J, Golden T, Varughese K and El-rayes I, Analytical Chemistry 61 (1989) 509

[118] Chen Z and Zhou Y, Surface modification of resistance welding electrodes by electro-spark deposited composite coatings, Surface and Coatings Technology 201 (2006) 2419-2430

CHAPTER 3

RESEARCH METHODOLOGY

3.1. Introduction

This chapter provide the methodologies followed throughout the study. Different acids/oxidisers (i.e., nitric acid (HNO_3), sulfuric acid (H_2SO_4), hydrogen peroxide (H_2O_2) and their mixtures; $H_2O_2:HNO_3$, $H_2O_2:H_2SO_4$ and $HNO_3:H_2SO_4$) were used to investigate the effect of each acid or acid mixtures on the structural and electrochemical properties of MWCNTs. Metal oxides treated at different temperatures were deposited on the surface of the acid-treated MWCNTs (A-MWCNTs) to investigate the effect of thermal treatment of metal oxides on the electrochemical activity of metal oxide functionalised MWCNTs.

3.2. Chemicals and reagents

All chemicals were generally of reagent grade and were used as received except where mentioned. Distilled water was used for all the preparations of materials in this study. Multi-walled carbon nanotubes (MWCNTs, > 98% purity and diameter of 3-7 nm), manganese chloride ($MnCl_2$), cobalt (II) nitrate hexahydrate ($Co(NO_3)_2.6H_2O$), N, N-Dimethylformamide (N, N-DMF, 55%), nafion, potassium hydroxide (KOH), sodium sulphate (Na_2SO_4) and aluminium oxide nanopowder were purchased from Sigma Aldrich. Sulfuric acid (H_2SO_4, 98%) and iron (III) nitrate nonahydrate ($Fe(NO_3)_3.9H_2O$) were purchased from Unilab. Potassium Permanganate ($KMnO_4$) and copper nitrate trihydrate ($Cu(NO_3)_2.3H_2O$) were purchased from Saarchem. Nickel nitrate hexahydrate ($Ni(NO_3)_2.6H_2O$) was purchased from Astrolabs. Nitric acid (HNO_3, 55%) and hydrogen peroxide (H_2O_2, 30%) were purchased from Ace-associated Chemical Enterprises and Rochelle Chemicals respectively.

3.3. Preparation of acid-treated MWCNTs

Acid treatments of the MWCNTs were used to generate a library of samples with different physical and chemical properties. Approximately 0.3 g of MWCNTs mixed with 200 mL of each of the following acids: H_2SO_4 (95%), HNO_3 (55%), H_2O_2 (30%) and a mixture of the acids, H_2O_2:H_2SO_4, H_2O_2:HNO_3 and HNO_3:H_2SO_4 in a ratio of 1:3 (v/v) were sonicated, using an ultrasound bath with a frequency of 35 kHz. After 3 h of sonication, the acid-treated MWCNTs was diluted with 200 mL of distilled water and filtered through a 0.45 µm pore sized Nylon Membrane (Sigma Aldrich). The acid-treated MWCNTs (A-MWCNTs) were then washed thoroughly with distilled water until a neutral pH is reached and left to dry at room temperature overnight [5].
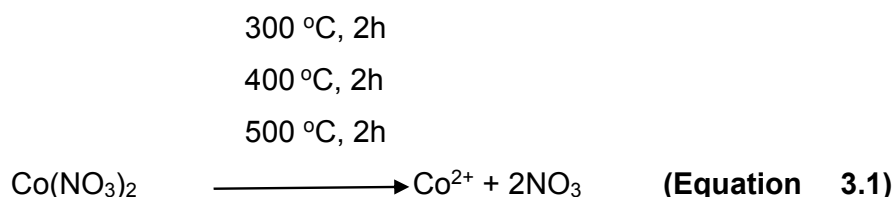
3.4. Preparations of metal oxides

3.4.1. Manganese oxide

Manganese oxide was synthesised by precipitation from an aqueous solution of $KMnO_4$ and $MnCl_2$ at room temperature, following a method described by Staiti and Lufrano [4]. Briefly, a 100 mL solution containing 0.03 moles of $MnCl_2$ was added dropwise to a 200 mL solution containing 0.02 moles of $KMnO_4$ under stirring for 30 min. The obtained suspension was stirred for 6 h during which a dark-brown precipitate was formed. After stirring, the suspension was left in the atmosphere for 16 h. Two distinct layers were formed consisting of fine precipitate and supernatant liquor. The liquor was removed by a pipette and the precipitate was washed with distilled water in the beaker before filtering. The formed precipitate was finally dried at 70 °C for 16 h after which a fine powder of manganese oxide was obtained.

3.4.2. Cobalt oxide

Cobalt oxide (Co_3O_4) samples were prepared by heating 20 g of (Co $(NO_3)_2$.$6H_2O$), under no specific controlled atmosphere, at different temperatures i.e, 300 °C, 400 °C and 500 °C. The heating apparatus used is a Carbolite, Bamford Sheffield England, S302AU. High temperature treatment results in decomposition of nitrate from the complex. The typical chemical reaction for preparation of cobalt oxide is as follows:

$$\text{Co(NO}_3)_2 \xrightarrow[\begin{array}{c}300\ °C, 2h\\400\ °C, 2h\\500\ °C, 2h\end{array}]{} \text{Co}^{2+} + 2\text{NO}_3 \qquad \textbf{(Equation 3.1)}$$

3.4.3. Preparation of CuO, NiO and Fe$_2$O$_3$

Similar method as described in section 3.4.2, above was used to prepare, CuO, NiO and Fe$_2$O$_3$, from their respective precursors.

3.5. Preparation of the manganese oxide/metal oxide composites

The manganese oxide/metal oxide (MnO$_2$/MO) composite was prepared by mixing 0.1 g of MnO$_2$ with metal oxide precursor to give a 1:1 mass ratio (i.e., the preparation of MnO$_2$/CuO composite, 0.1 g of MnO$_2$ was mixed with 0.9 g of Cu(NO$_3$)$_2$.3H$_2$O). The mixture was then calcined at 400 °C for 2 h. The composites were prepared in a 20 mL beaker.

3.6. Incorporation of metal oxide into the acid-treated MWCNTs

About 5 % of the prepared metal oxides were incorporated into the acid treated-MWCNTs (treated with H$_2$O$_2$:HNO$_3$). Approximately 0.01 g of the metal oxide was mixed (in a 20 mL beaker) with 0.2 g MWCNTs (as to give 5 wt.% metal oxide/MWCNTs) and 4 ml of *N, N*-Dimethylformamide as the binder. The nanocomposites were sonicated for 15 min to allow the metal oxides to be well coated/dispersed on the surface of A-MWCNTs. The mixture of metal oxides-multi walled carbon nanotubes (MO-MWCNTs) nanocomposites was left to dry at room temperature for overnight to allow the solvent to evaporate.

3.7. Incorporation of MnO$_2$/metal oxide into the acid treated MWCNTs

The MnO$_2$/MO-MWCNTs was prepared by the same method employed for the preparation of MO-MWCNTs in section 3.6 above. Approximately 0.01 g of the

MnO$_2$/MO was mixed with 0.2 g acid treated-MWCNTs and 4 ml DMF. The mixture was sonicated for 15 min and was left to dry at room temperature for overnight.

3.8. Characterisation techniques

3.8.1. Fourier transform infrared spectroscopy

Fourier transform infrared (FT-IR) Spectroscopy was used to identify the functional groups present on the surface of the raw- and acid-treated MWCNTs. The instrument used is an Agilent Cary 600 series FTIR spectrophotometer (with resolution of 4 cm^{-1} and 4 scan numbers at room temperature). The crystal area was cleaned with acetone and the background was then collected. A small portion of the finely ground powder sample (the tip of a spatula and enough to cover the crystal area of the instrument) was placed onto the small crystal area and analysed.

3.8.2. Scanning electron microscopy

Scanning electron microscopy (SEM) was undertaken on a Supra 55 variable pressure field emission scanning electron microscope. The surface morphology analysis of the metal oxides and metal oxide-MWCNTs nanocomposites was investigated, about 0.0002 g of the finely ground sample was mounded on aluminium stubs, care was taken to obtain a very thin layer of the material. A double sided carbon tape was used to immobilise the powder samples. The samples on the aluminium stubs were then loaded onto sample holders for analysis. The samples were not coated with any conductive film. The images were captured at 2kV, WD= 2.8 – 4.7 mm and using a SmartSEM® (Carl Zeiss, Germany) software.

3.8.3. Transmission electron microscopy

The morphology and microstructure of the acid-treated MWCNTs and metal oxides-MWCNTs samples were analysed using JEOL JEM-2100 electron microscope operating at an accelerating voltage of 200 kV. Sample specimens for TEM studies were prepared by ultrasonic dispersion of a small amount (the tip of a spatula) of MWCNTs samples in ethanol. The suspensions were coated onto a holey carbon

grid by dipping the carbon grid inside the MWCNTs/ethanol suspension. The carbon grids were then allowed to dry at room temperature and loaded onto sample holders for analysis.

3.8.4. X-ray diffraction

Approximately 1 g of the finely ground sample was placed into the aluminium sample holder using a glass slide assuring a flat upper surface. Special care was taken to create a flat upper surface. X-ray diffraction (XRD) patterns of the nanocomposite materials were determined on a Philips PW 1380 X-Ray diffractometer with high intensity of Cu-K_α radiation (λ = 1.54 Å, 40 kV and 40 mA) and a graphite monochrometer at a scanning rate of 0.02 s^{-1} ranging from 5 to 65° 2-theta (2θ), where θ is the diffraction angle. The raw count data was captured using Phillips APD (Automatic Powder diffraction) software, it was then converted into ASCII format and imported into Microsoft excel spread sheet. Data was then transferred from Microsoft excel spread sheet to origin 6.1 for plotting, 5 smoothing points were considered.

3.8.5. Brunauer-Emmett-Teller

The surface area and pore volume of the MWCNTs samples were determined by N_2 physisorption at -195.8 °C using a Micrometrics TRISTAR II surface area analyser. About 0.03 g of the sample was loaded in a glass tube sample holder. The samples were degassed at 60 °C overnight under vacuum to evacuate any atmospheric contaminants. The samples were then loaded onto the Micromeritics Tristar II 3020 surface area and porosity analyser. The surface area and pore volume were determined by the Brunauer-Emmett-Teller (BET) method. Pore size distribution of the MWCNTs samples was obtained by using Barrett-Joyner-Halenda (BJH) equation using the adsorption isotherm.

3.8.6. Thermogravimetric analysis

The TGA analysis was undertaken on a Perkin Elmer STA 4000 analyser. About 5 to 10 mg of sample was placed in a ceramic pan and placed in the instrument furnace. The temperature of the sample was increased from room temperature to 900 $^{\circ}$C at 10 $^{\circ}$C/min under an oxidative atmosphere (air, 50 mL/min). The TGA profile obtained gives information on the sample composition (including % metal loading in the case of a catalyst), thermal stability (under a specific atmosphere) and the purity. The derivative (DTG) curve can be used to identify the decomposition temperature maxima.

3.9. Electrochemical studies

All electrochemical hydrogen storage experiments and supercapacitor studies were performed in nitrogen-saturated potassium hydroxide and sodium sulfate electrolytes, respectively. The experiments were carried out on a Bioanalytical Systems Inc. (BASI) potentiostat driven by the epsilon EC (version 1.60.70), using a three-electrode system consisting of a glassy carbon electrode (GCE, 3.0 mm diameter) as working electrode, Ag/AgCl (saturated NaCl solution) as reference electrode and platinum wire as auxiliary electrode. This ensured that the potential between the working electrode and the reference electrode is minimized. The electrochemical performance of raw, acid treated and metal oxide-MWCNTs were measured using cyclic voltammetry (CV) and chronopotentiometry technique. The electrochemical measurements were performed at room temperature.

3.9.1. Electrode cleaning

Prior to each measurement the electrode was polished with a polishing pad with aluminium oxide (0.05 µm) and rinsed with distilled water. The electrode was then dried using a house hold hairdryer for about 30 s.

3.9.2. Preparation of electrodes and their electrochemical measurements

3.9.2.1. Electrochemical hydrogen storage

The raw, acid-treated and metal oxide-MWCNTs were used to fabricate the electrode as follows: Approximately, 4 mg of nanocomposites materials was added into a solution of nafion (0.1 mL) and distilled water (3 mL). Nafion was used to prevent loss of the materials from the electrode surface. Nafion, a perfluorosulfonated derivative of Teflon, is a cation-exchange polymer whose films are highly permeable to cations but almost impermeable to anions [6]. The mixture was sonicated for 15 min and then drop-dried on the surface of the GCE. Finally the electrodes were dried in an oven at 80 °C for 2h. The mass of the electrode was recorded before and after the fabrication using a 0.0001 g precision balance, to determine the amount of the material on the electrode. The amount of the material on the surface of the GCE electrode ranged between 0.30-0.35 mg.

Electrochemical hydrogen storage capacities of fabricated electrodes were studied using a three electrode system (BASi epsilon) at room temperature in a 6 M solution of KOH as the electrolyte. Cyclic voltammetric (CV) measurements were carried out in a potential window of -1.4 to 0.2 V at a scan rate of 50 mV/s. The experiments of charging and discharging were carried out under the following conditions: The electrodes were charged for 120 s in a constant current of 3 mA and discharged under the same constant current [7].

3.9.2.2. Electrochemical supercapacitor

The fabrication of working electrodes was carried out as follows: The as-prepared nanocomposites, carbon black (to improve the conductivity of the material) and the binder, poly (tetrafluoroethylene) (PTFE) were mixed in a mass ratio of 75:20:5 and dispersed in ethanol. The resulting mixture was dropped on the surface of the working electrode and dried at 100 °C for 2 h in an oven. The measurements were carried out in a 1 M Na_2SO_4 aqueous electrolyte at room temperature. CV tests were carried out using a potential window ranging between -0.1 and 0.9 V at a scan rate of 50 mV/s [8].

3.10. References

[1] Wepasnick K.A, Smith B.A, Schrote K.E, Wilson H.K, Diegelmann S.R and Fairbrother D.H, Surface and structural characterisation of multi-walled carbon nanotubes following different oxidative treatments, Carbon 49 (2011) 24-36

[2] Tsoufis T, Tomou A, Gournis D, Douvalis A. P, Panagiotopoulos I and Kooi B, Novel nanohybrids derived from the attachment of FePt nanoparticles on carbon nanotubes, Journal of Nanotechnology 8 (2008) 5942-5951

[3] Staiti P and Iufruno F, Study and optimisation of manganese oxide-based electrodes for electrochemical supercapacitors, Journal of Power Sources 187 (2009) 284-289

[4] Wen J, Ruan X and Zhou Z, Preparation and electrochemical performance of novel ruthenium-manganese oxide electrode materials for electrochemical capacitors, Journal of Physics and Chemistry of Solids 70 (2009) 816-820

[5] Kim Y, Cho J, Ansari S.G, Kim H, Dar M.A, Seo H, Kim G, Lee D, Khang G and Shin H, Immobilisation of avidin on the functionalised carbon nanotubes, Synthetic metals 156 (2006) 938-943

[6] Wen J, Ruan X and Zhou Z, Preparation and electrochemical performance of novel ruthenium-manganese oxide electrode materials for electrochemical capacitors, Journal of Physics and Chemistry of Solids 70 (2009) 816-820

[7] Reyhani A, Mortazavi S.Z, Golikand A.N, Moshfegh A.Z and Mirershadi S, The effect of various acids treatment on the purification and electrochemical hydrogen storage of multi-walled carbon nanotubes, Journal of Power Sources 183 (2008) 539-543

[8] Yan J, Fan Z, Wei T, Cheng J, Shao B, Wang K, Song L and Zhang M, Carbon nanotubes/MnO_2 composites synthesised by microwave-assisted method for supercapacitors with high power and energy densities, Journal of Power Sources 194 (2009)1202-1207

CHAPTER 4

RESULTS AND DISCUSSION

ELECTROCHEMICAL STUDIES OF MWCNTs TREATED WITH DIFFERENT ACIDS/OXIDISER

4.1. Introduction

Herein, the study focused on the investigation of the effect of acids treatment on the structure, electrochemical hydrogen storage and supercapacitor performance of MWCNTs. The study hoped to develop an efficient method for the treatment of MWCNTs without compromising the structure of the material. The method should not only decrease the hydrophobicity of MWCNTs but also increase the electrochemical reactivity of the material towards hydrogen storage and supercapacitors.

4.2. Characterisation

4.2.1. Fourier transform infrared analysis

The data in figure 4.1 shows the FTIR spectra of raw and acid-treated MWCNTs. The spectra of raw MWCNTs show the absence of –CO and –OH functional groups, similar results have been reported by Dai *et al.* [1]. However on acidification, the peak at 2985 cm^{-1} due to –CH stretch and 1064 cm^{-1} due to C-O, becomes clearer. Interesting to note is an increase in intensity of the C-O and CH stretch, when acids were changed from H_2SO_4, to HNO_3, and lastly H_2O_2. The intensity of this peaks became prominent on the H_2O_2 treated MWCNTs, with an emergence extra peaks at 3673 cm^{-1}, due to an –OH stretch. Two weak peaks also emerged at 1401 and 1241 cm^{-1}, which are due to the O-H bending deformation of carboxylic acid group and acidic C-O bonds, respectively [2, 3].
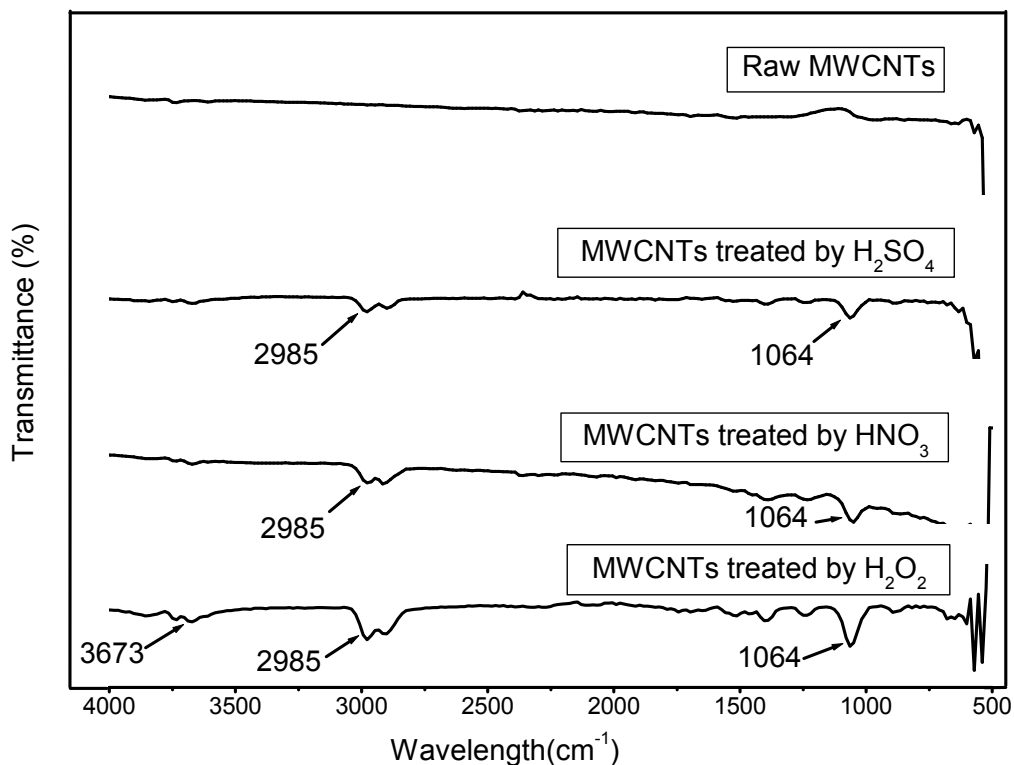
Figure 4.1: FTIR spectra of raw- and acid-treated MWCNTs.

The intensity of peaks (1064, 1241, 1401, and 2984 cm^{-1}), as shown in figure 4.2 become more prominent when the MWCNTs was treated by mixture of acids. Dai *et al.* [1] reported an increase in the intensities of –CO and –OH functional groups on the surface of the acid-treated MWCNTs with an increase in the HNO$_3$ concentration from 1 M to 5 M. Almost similar intensity of the functional groups has been introduced on the surface of MWCNTs from both nitric and sulphuric acid (HNO$_3$:H$_2$SO$_4$) and hydrogen peroxide and nitric acid (H$_2$O$_2$:HNO$_3$) mixtures. The data clearly reveals some interesting findings, especially on the mixture of H$_2$O$_2$:HNO$_3$. This mixture is not a mixture of choice in all or most of the previous acids treatments of MWCNTs, [1, 4] yet it shows almost the same functional groups as the mixture of HNO$_3$:H$_2$SO$_4$. Moreover, the H$_2$O$_2$:HNO$_3$ acid mixture does not cause damage to the walls of MWCNTs, as confirmed by XRD results [Figure 4.4].
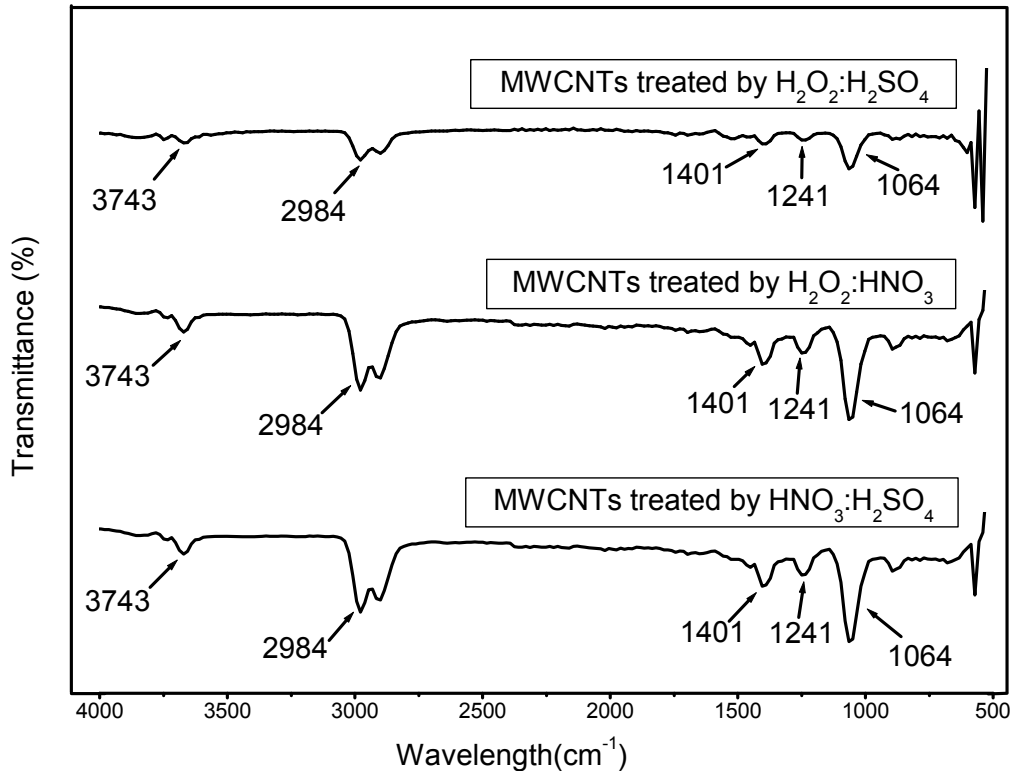
Figure 4.2: FTIR spectra of acid-treated MWCNTs.

4.2.2. X-ray diffraction analysis

Figure 4.3 and 4.4 shows the XRD profiles of raw MWCNTs and acid-treated MWCNTs. The intense diffraction at 26 $^\circ$ two theta, in all samples is indexed to the C (002) plane reflection of the graphite [1, 5]. The sharpness of the peak for the MWCNTs treated by HNO_3, H_2O_2, H_2O_2:H_2SO_4 and H_2O_2:HNO_3 (Figure 4.3 and 4.4), indicates that the graphitic structure of the MWCNTs remained intact without significant damage [5]. A decrease in the sharpness of the peak is observed when the MWCNTs are treated by H_2SO_4 (Figure 4.3), this could be attributed to the damaging effect that this strong acid can have on the structure of the MWCNTs. This finding is clearly visible when the MWCNTs are treated by a mixture of two stronger acids HNO_3:H_2SO_4 (Figure 4.4). This is attributed to the destroying effect of this acid treatment method [2]. However, the use of a mixture of an oxidiser (H_2O_2) and HNO_3 or H_2SO_4 gave sharp and more intense peak (Figure 4.4). This shows the formation of more ordered MWCNTs [6].
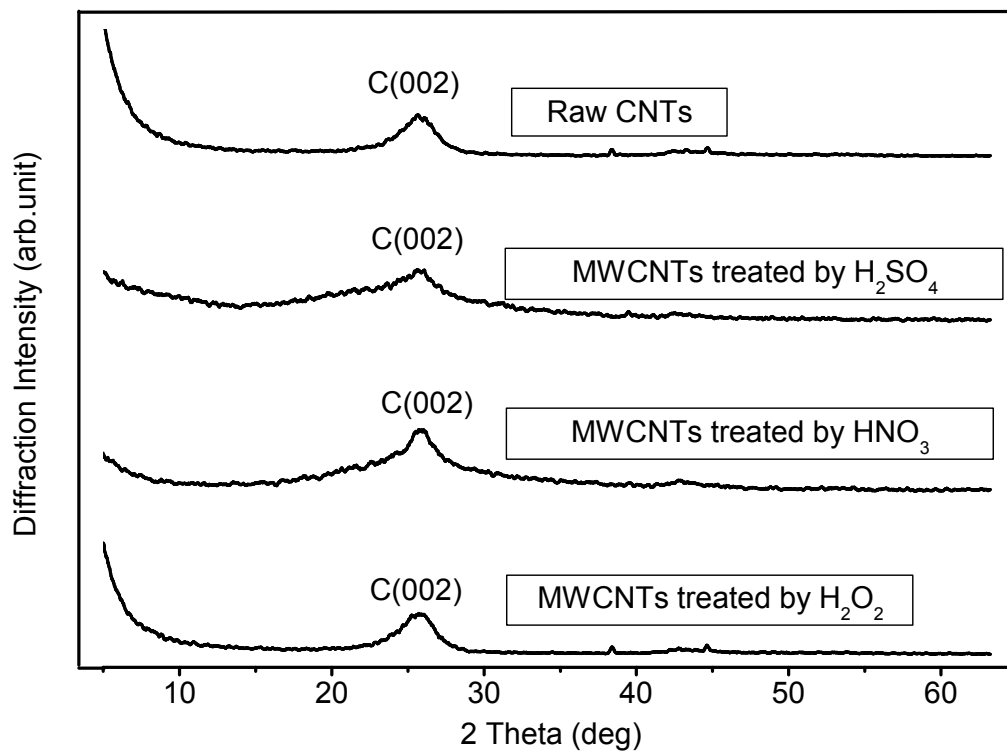
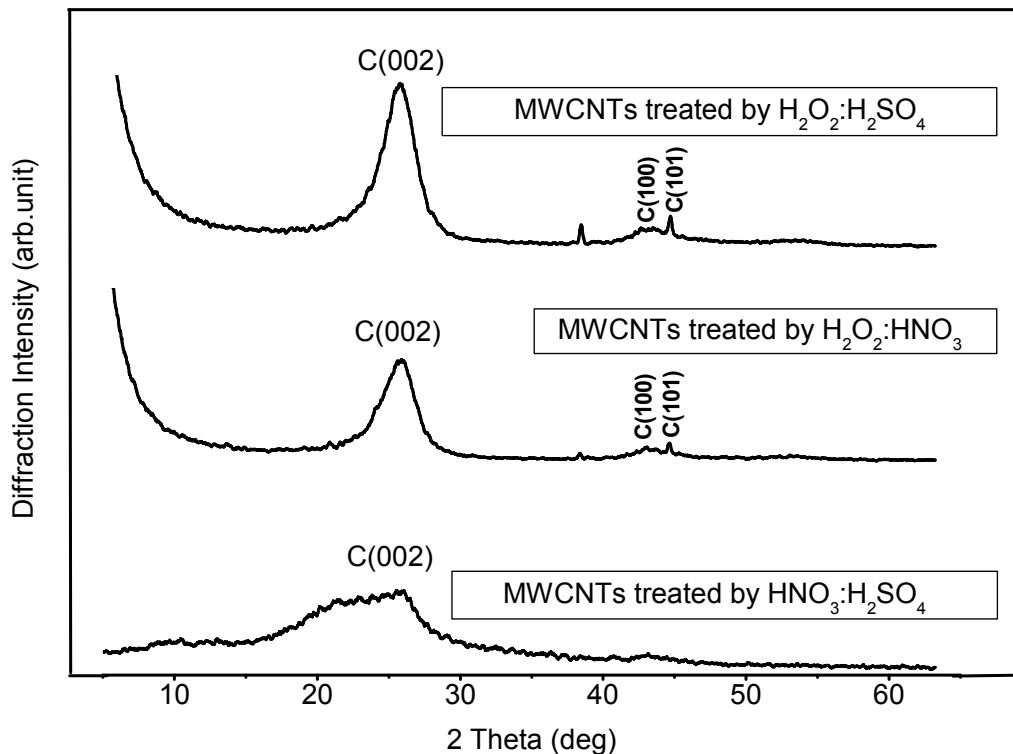**Figure 4.3:** XRD spectra of raw- and acid-treated MWCNTs.

Figure 4.4: XRD spectra of MWCNTs treated by mixture of acids.

4.2.3. Transmission electron microscopy analysis

4.2.3.1 Low magnification TEM micrographs of the raw and acid-treated MWCNTs

The microstructure of the raw- and acid-treated MWCNTs was characterised by TEM which provides sufficient resolution for direct visualisation of the MWCNTs length and surface. Figure 4.5 and 4.6 illustrates the low magnification TEM micrographs of the raw and acid-treated MWCNTs. It can be clearly seen from the images that some tubes were open at one end and some were open at both ends (shown by black circles on Figure 4.5 and 4.6). Tubes length were not measured before and after treatment, but from the images it looks like the length of MWCNTs remains almost the same after treatment suggesting that the treatment with mild acids does not cause any significant damage to the structure of the MWCNTs. Chiang *et al.* [5] reported similar results when they treated MWCNTs with 4 M H_2SO_4/HNO_3 for different days (0.5, 1, 2, 4, or 7 days). They reported that 4 M H_2SO_4/HNO_3 reflux

retained the long-tube structure of MWCNTs but, prolonged refluxing would cut some of the nanotubes. According to TEM data the overall morphology of the MWCNTs remains almost intact after mild acid treatments (HNO_3, H_2O_2, H_2O_2:HNO_3 and H_2O_2:H_2SO_4).

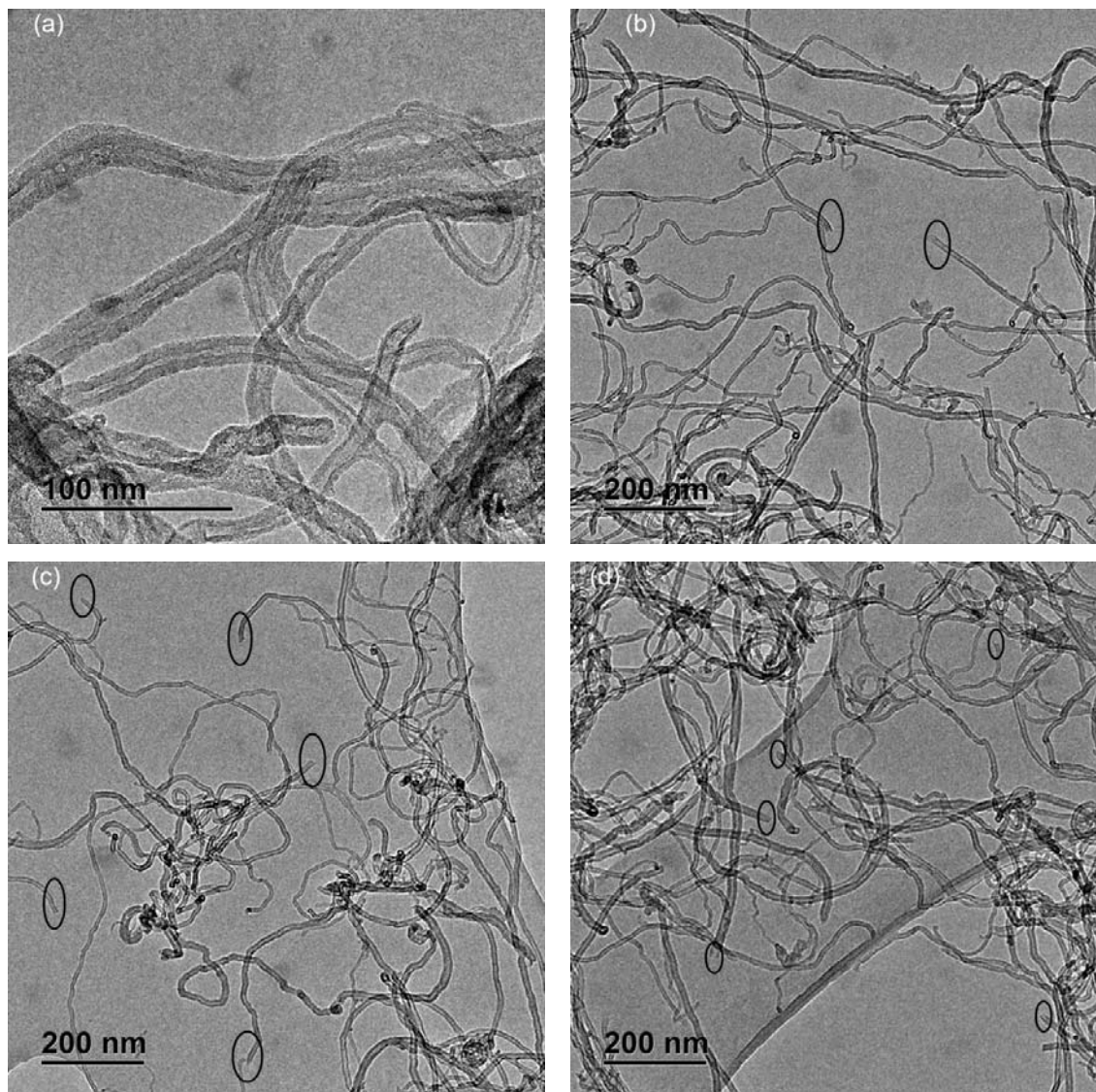**Figure 4.5:** Low magnification TEM images of (a) raw MWCNTs, MWCNTs treated by (b) H_2O_2 (c) HNO_3 and (d) H_2SO_4.
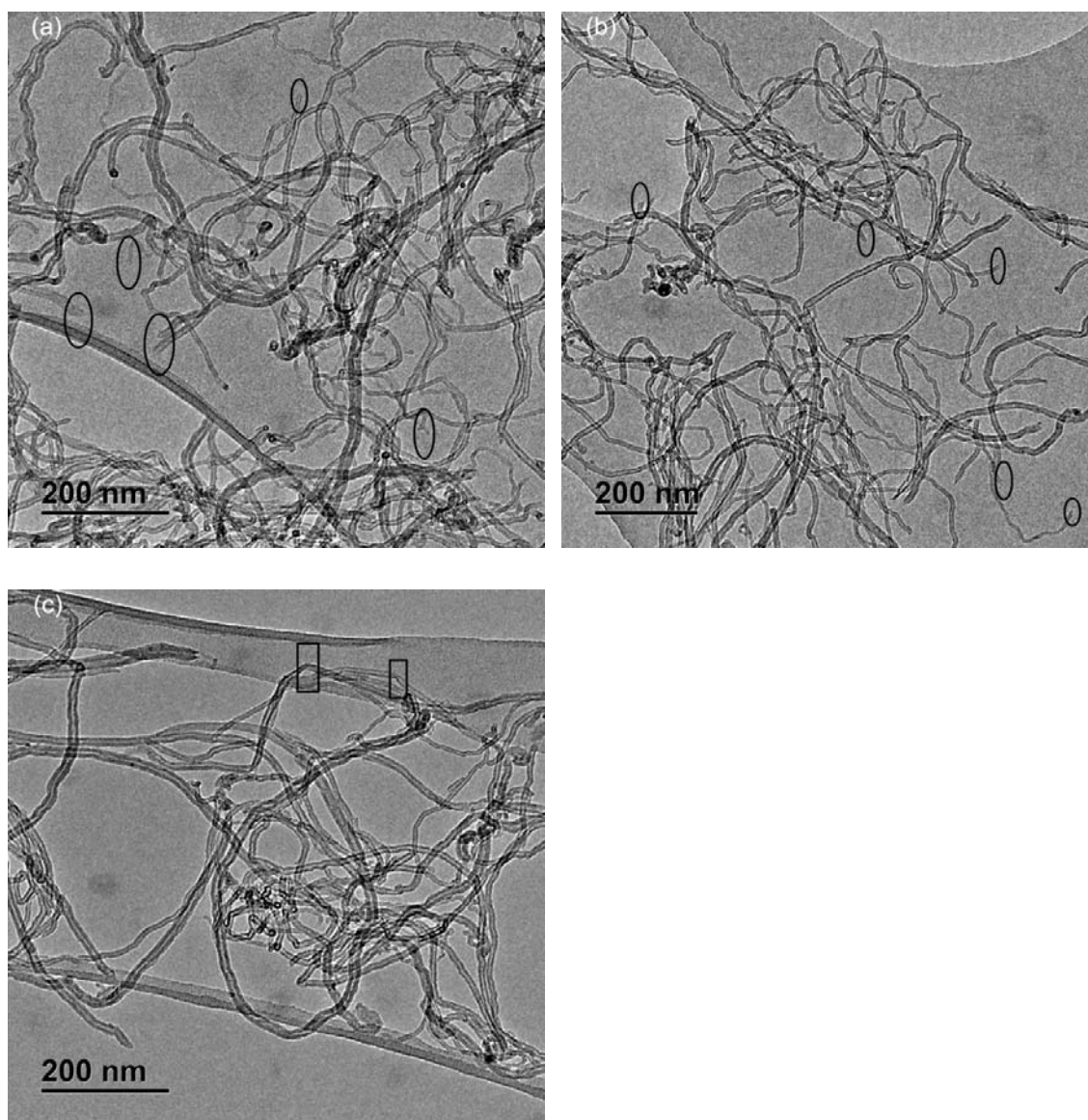
Figure 4.6: Low magnification TEM images of MWCNTs treated by (a) H_2O_2:HNO_3 (b) H_2O_2:H_2SO_4 and (c) HNO_3:H_2SO_4.

4.2.3.2 High magnification TEM micrographs of the raw and acid-treated MWCNTs

The high magnification micrographs of the MWCNTs treated by single acid and mixture of acids are shown on figure 4.7 and 4.8. From the TEM images it shows that the samples exhibit a narrow tubular morphology. The walls are often parallel to the main axis of the tubes and seem to be well organised: Single graphene sheets propagate over hundreds of nanometres. However, hollow fishbone-like structures with prismatic edges on both the external and internal surfaces of the tubes were

also often observed (Figure 4.8 (a)). For the raw MWCNTs (Figure 4.7(a)), a more unusual observation was made: different numbers of walls presents defective sides were the tubes are bent from each side of the nanotube (shown by black circles). We also observe bamboo carbon structures inside the inner hollow nanotube. The tubes become thinner when they are treated with H_2O_2, with the removal of some of the bamboo carbon structures observed on the raw MWCNTs. The structures inside the tubes are completely removed when the MWCNTs are treated by HNO_3 (Figure 4.7(c)). The walls of some of the thin MWCNTs are damaged after treatment with H_2SO_4 (Figure 4.7(d)), which is consistent with the results obtained from XRD.
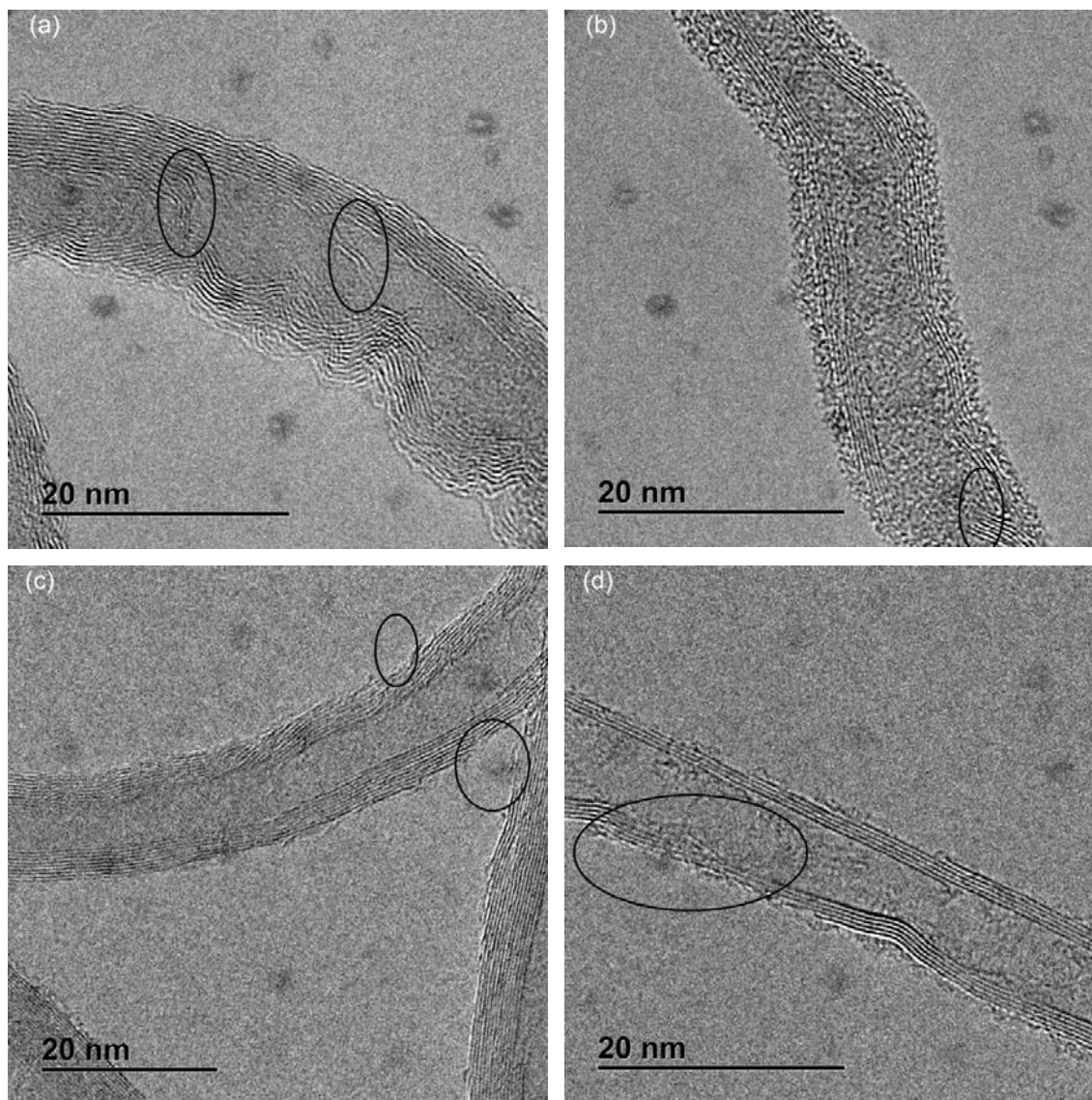

Figure 4.7: High magnification TEM images of (a) raw MWCNTs, MWCNTs treated by (b) H_2O_2 (c) HNO_3 and (d) H_2SO_4.

The treatment of MWCNTs with HNO_3 + H_2SO_4 (Figure 4.8(c)) results in a destruction of tubular structure of MWCNTs and formation of bamboo carbon structures inside the tube, similar results have been reported by Mazov *et al.* [4] and Shirazi *et al.* [2]. The surface of treated nanotubes remains relatively smooth with less significant topological damage to the walls after treatment with mild acids. The treatment using mild acids results in the removal of bamboo carbon structures inside the inner tubes of the MWCNTs and results in the formation of thinner MWCNTs, similar results have been reported elsewhere [4]. For the MWCNTs treated by mild acids the inner channel of the MWCNTs is empty and accessible.
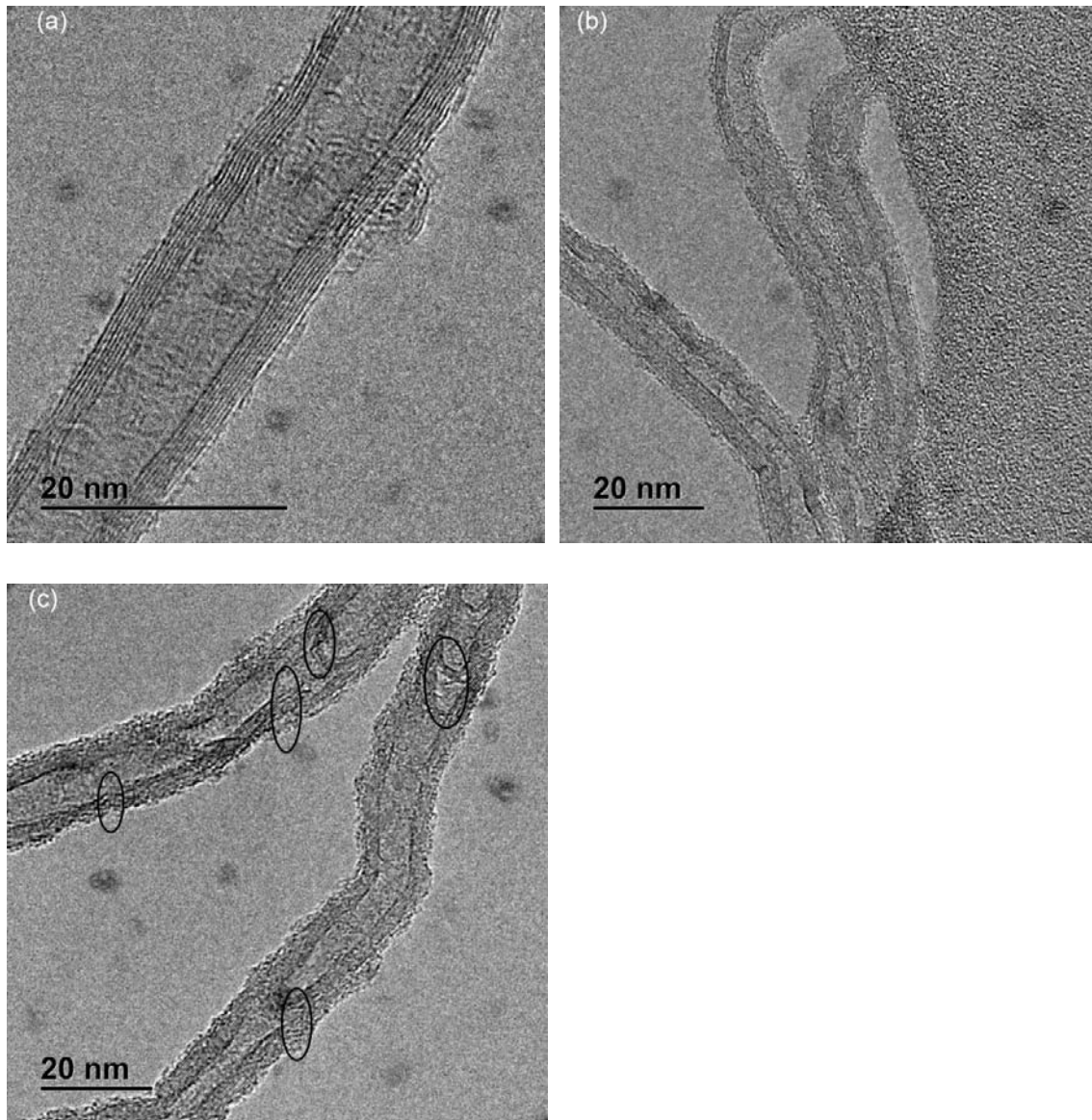

Figure 4.8: High magnification TEM images of MWCNTs treated by (a) H_2O_2:HNO_3 (b) H_2O_2:H_2SO_4 and (c) HNO_3:H_2SO_4.

4.2.4. Brunauer-Emmett-Teller analysis

Nitrogen adsorption represents the most widely used technique to determine materials surface area and to characterise its porous structure [7]. The nitrogen adsorption-desorption isotherms of the MWCNTs samples are shown in figure 4.9 and 4.10. The hysteresis loop of MWCNTs are close to the type-IV isotherm and show a sharp capillary condensation step at a relative pressure of P/P_0 ~ 0.40-0.99, indicating a typical mesoporous structure. The surface and volume characteristics of MWCNTs samples calculated according to the isotherm data are summarised in table 4.1. The total BET surface area of the samples ranges from 223.72 m^2/g to 736.58 m^2/g. The BET surface area of the MWCNTs increases after treatment with mild acids and remains almost the same after treatment with H_2SO_4. However the surface area of the MWCNTs treated by HNO_3:H_2SO_4 decreases to 223.72 m^2/g compared to 251.48 m^2/g of the raw MWCNTs. The decrease in the surface area is due to the structural changes caused by the use of a mixture of two strong acids, as it was observed on the XRD spectra and TEM images (Figure 4.4 and 4.8 (c)).

The surface area increases to 343.09 m^2/g for the MWCNTs treated by H_2O_2+HNO_3 compared to 251.48 m^2/g of the raw MWCNTs. The highest BET surface area of 736.58 m^2/g was recorded on MWCNTs treated by H_2O_2:H_2SO_4. De-bundling of MWCNTs and breakage/removal of bamboo carbon structures observed inside the inner tubular channel of the raw MWCNTs (Fig 4.7 (a)) after treatment with mild acids contributed to the higher surface area observed. Dai *et al.* [1] and Naseh *et al.* [8] also reported an increase in the specific surface area of MWCNTs after treatment with acids. Naseh *et al.* suggested that the increase in the specific surface area might be due to opening of the tube ends and the generation of defects on the sidewall of nanotubes, creating access into the cavity of the nanotubes. The pore size distribution of the MWCNTs samples are shown as inserts in figure 4.9 and 4.10. The pore size distribution calculated from the desorption branch of the isotherm using the BJH method shows a bimodal distribution: Small pores between 2-5 nm in diameter, which correspond to the inner channel of the nanotubes. Longer pores, with maxima ranging between 42 and 87 nm are formed between the entangled nanotubes. The MWCNTs treated by H_2O_2:HNO_3 (Figure 4.10, insert) showed much higher pore volume and wider pore size distribution between the nanotubes.

The major peak of distribution for the raw MWCNTs is observed at around 87 nm (Figure 4.9 and 4.10, insert). The H_2O_2:HNO_3 treated MWCNTs shows two major distribution peaks at 43 and 87 nm (Figure 4.10, insert). The major peak of distribution for the MWCNTs treated by H_2O_2:H_2SO_4 (Figure 4.10, insert) is observed around 43 nm. From the pore distribution curves (Figure 4.10, insert) it can be clearly seen that the MWCNTs treated by H_2O_2:H_2SO_4 have smaller average diameter between the nanotubes as compared to the other MWCNTs samples. This indicates that the H_2O_2:H_2SO_4 treated MWCNTs are more entangled as compared to H_2O_2:HNO_3 treated MWCNTs.

Figure 4.9: N_2 adsorption and desorption isotherms and BJH pore size distribution of the (a) raw MWCNTs (black line), MWCNTs treated by (b) H_2O_2 (red line) (c) HNO_3 (green line) and (d) H_2SO_4 (blue line).
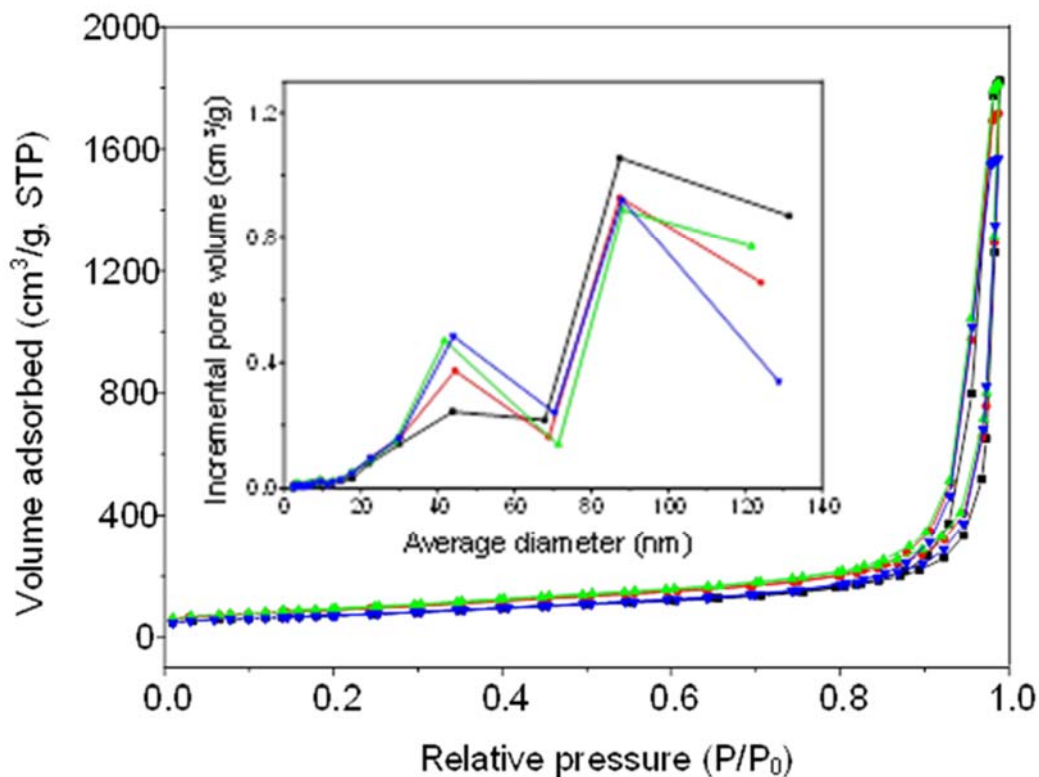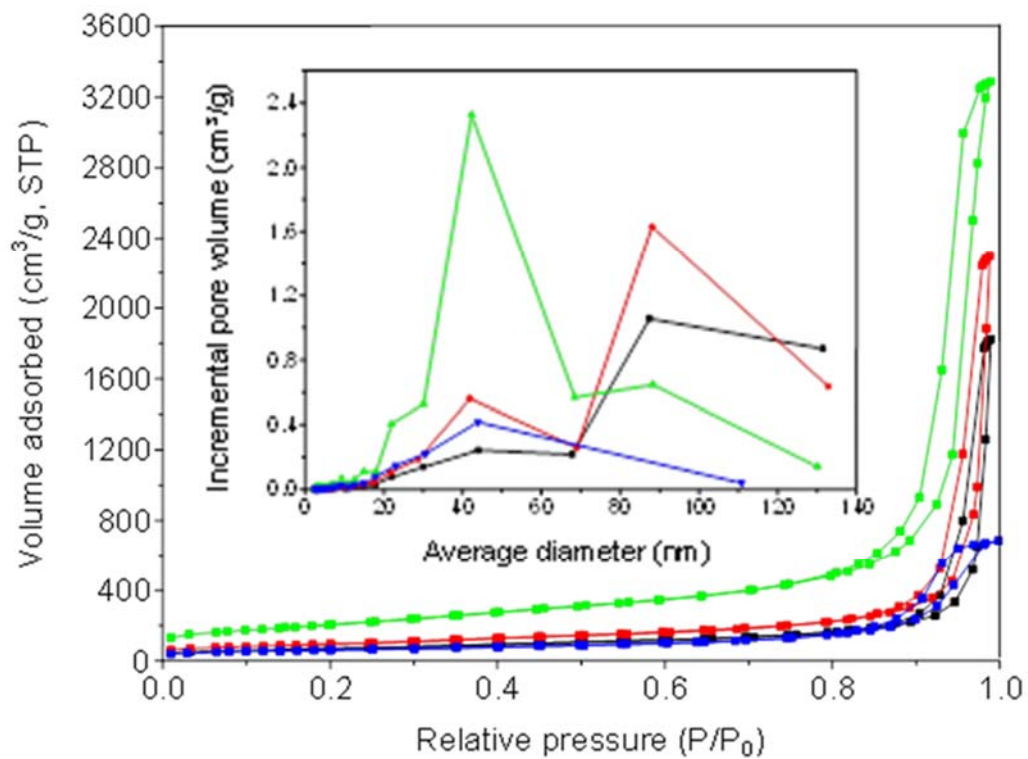
Figure 4.10: N_2 adsorption and desorption isotherms and BJH pore size distribution of the (a) raw MWCNTs (black line), MWCNTs treated by (b) $H_2O_2:HNO_3$ (red line) (c) $H_2O_2:H_2SO_4$ (green line) and (d) $HNO_3:H_2SO_4$ (blue line).

Table 4.1: Surface characteristics of raw- and acid-treated MWCNTs determined from nitrogen physisorption at -195.8 °C

Sample name	BET surface area (m^2g^{-1})	Pore volume (cm^3g^{-1})	Pore sizes (nm)
MWCNTs treated by HNO_3:H_2SO_4	223.72	1.06	18.97
MWCNTs treated by H_2SO_4	250.59	2.09	33.30
Raw MWCNTs	251.48	1.95	30.98
MWCNTs treated by H_2O_2	313.61	1.99	25.46
MWCNTs treated by HNO_3	328.25	2.03	24.74
MWCNTs treated by H_2O_2:HNO_3	343.09	2.91	33.96
MWCNTs treated by H_2O_2:H_2SO_4	736.58	4.94	26.83

4.2.5. Thermogravimetric analysis

Thermogravimetric analysis (TGA), coupled with a derivative curve of the weight loss (DTG), is often used to investigate the thermal stability as well as the composition and purity of carbon materials. The TGA profiles measured in flowing air for the raw-

and acid-treated MWCNTs are shown in figure 4.11. All the samples exhibited only one weight loss step. Thermal stability of MWCNTs treated by $HNO_3:H_2SO_4$ decreases in comparison to the other electrode material. The material start decomposing at low temperatures around 400 °C, in relation to the other electrode materials, which starts decomposing at around 550 °C. This can be attributed to the damaging effect that this acid mixture had on the walls of MWCNTs decreasing the thermal stability of the MWCNTs.
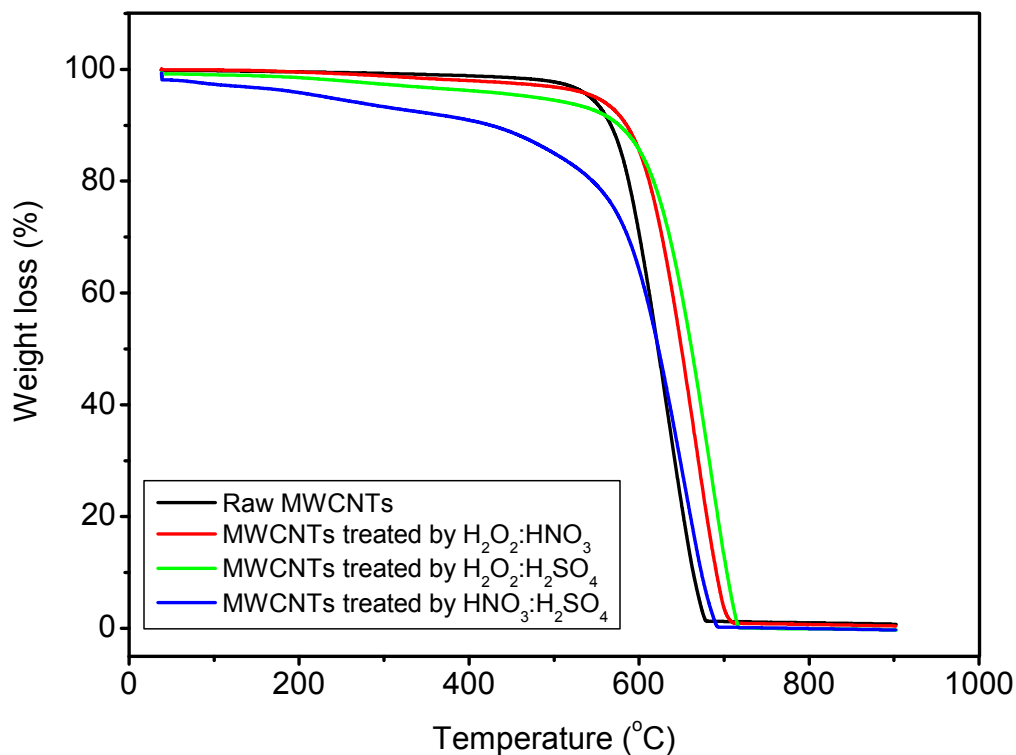

Figure 4.11: TGA profiles for the raw- and acid-treated MWCNTs under air atmosphere.

Derivative curves directly reflect the variation in the weight as a function of temperature by occurrence of thermal events. The DTG profiles measured in flowing air for the raw- and acid-treated MWCNTs are shown in figure 4.12. It is observed that DTG curves of the samples has only one peak which belongs to the oxidation of MWCNTs. This is evidence of low/no amorphous carbon content on the samples. DTG curves consist of broad peaks in different positions, suggesting an influence of the different acids treatment on the thermal stability of MWCNTs. The maximum

weight losses of the MWCNTs samples are observed at 630 °C, 651 °C, 662 °C and 680 °C for the raw MWCNTs, MWCNTs treated by $HNO_3:H_2SO_4$, MWCNTs treated by $H_2O_2:HNO_3$ and MWCNTs treated by $H_2O_2:H_2SO_4$ respectively.

Oxidation with mild acids mixtures increase the thermal stability of the MWCNTs, however the thermal stability of the MWCNTs treated by $HNO_3:H_2SO_4$ is lower than the other acid-treated MWCNTs samples. This results demonstrate that the acid-treatment with mild acid mixtures did not damage the structure of MWCNTs, but the oxidant started to attack active sites already existing on the nanotubes such as the –CH_2 and –CH groups, improving the thermal stability of the MWCNTs [5].
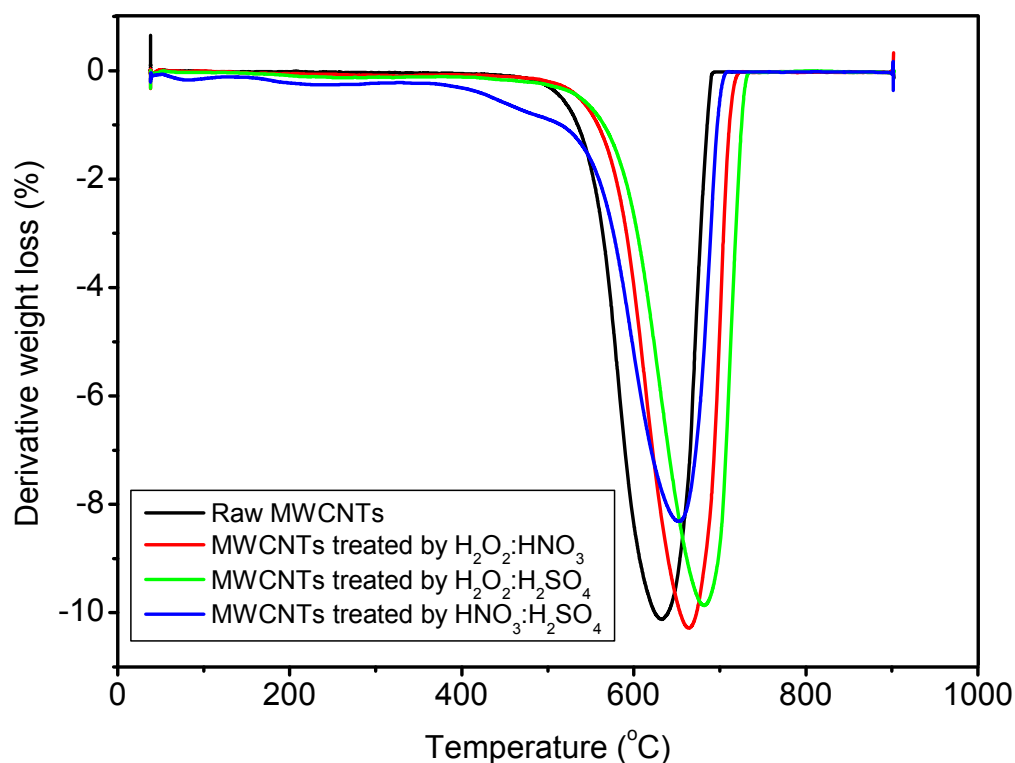

Figure 4.12: DTG profiles for the raw- and acid-treated MWCNTs under air atmosphere.

4.3. Electrochemical measurements

4.3.1. Electrochemical hydrogen storage

4.3.1.1. Cyclic voltammetric characteristic of raw and acids-treated MWCNTs electrode

Figure 4.13 shows the cyclic voltammogram of raw-, and acids-treated MWCNTs electrodes. Measurements were studied using a three electrode system in a 6 M solution of KOH as the electrolyte. Runs were carried out in a potential window of -1.4 to 0.2 V at a scan rate of 50 mV/s. The results show the current respond peak at -450 mV, due to the hydrogen uptake by raw MWCNTs during the electrode charging process. Its discharge process occurred at -350 mV. The current responds of both H_2SO_4 (red line) and HNO_3 (green line) acid treated MWCNTs, showed an increase and slight shift of peak position (towards more negative overpotential), as compared to raw MWCNTs. However, a decrease in current response accompanied by a peak shift (towards less negative overpotential) was observed on H_2O_2 treated MWCNTs (Figure 4.13, blue line). It shows that the oxidative overpotential of hydrogen at this electrode is lower. The reduction reaction of hydrogen is more easy [9]. This behaviour is also observed for the MWCNTs treated by a mixture of H_2O_2:HNO_3 (Figure 4.14), with the electrodes showing an increase in current response.
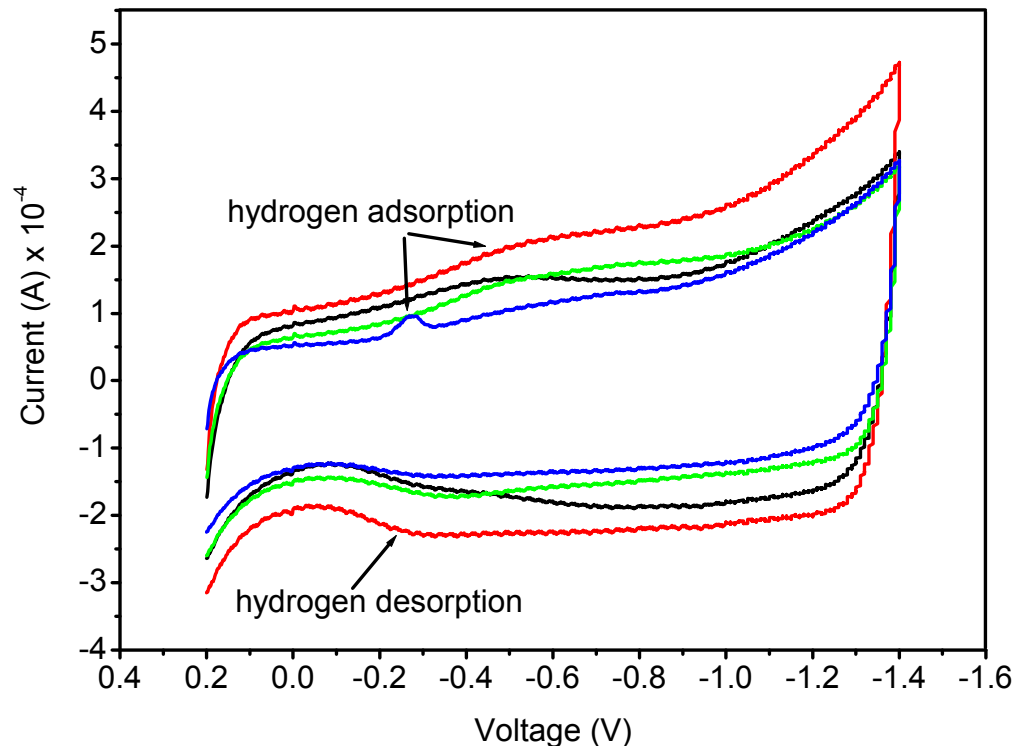
Figure 4.13: CV curves of (a) raw MWCNTs (black line), MWCNTs treated by (b) H_2SO_4 (red line) (c) HNO_3 (green line) and (d) H_2O_2 (blue line).

The results in figure 4.14 shows cyclic voltammogram of raw MWCNTs (black line), mixture of H_2O_2:H_2SO_4 (red line), H_2O_2:HNO_3 (green line) and HNO_3:H_2SO_4 (blue line) treated MWCNTs electrodes. The mixture of H_2O_2:HNO_3 treated MWCNTs electrode gave higher current response, and a more prominent rectangular shape compared to all other electrodes. This clearly shows that H_2O_2:HNO_3 treated MWCNTs contain some interesting properties as confirmed by FTIR, XRD, TEM and BET results.

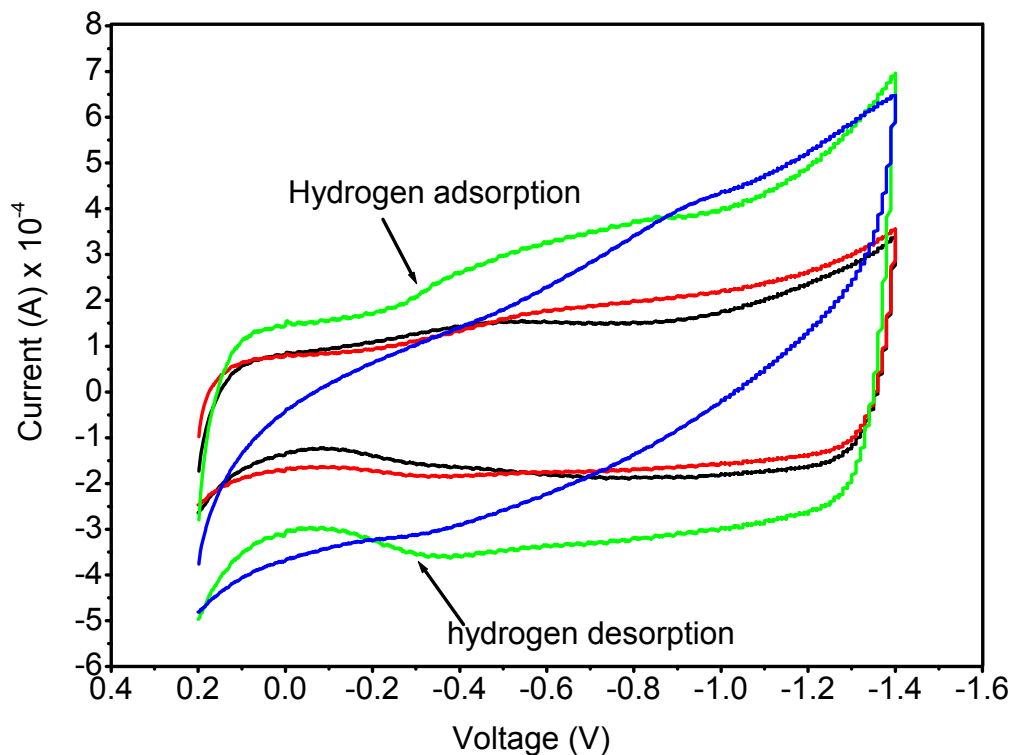**Figure 4.14:** CV curves of (a) raw MWCNTs (black line), MWCNTs treated by (b) H_2O_2:H_2SO_4 (red line) (c) H_2O_2:HNO_3 (green line) and (d) HNO_3:H_2SO_4 (blue line).

4.3.1.2. Charge-discharge capacity studies of raw and acids-treated MWCNTs electrode

The charge-discharge capacity studies revealed that H_2O_2:HNO_3 treated MWCNTs electrode gave the discharge capacity of 73 mAh/g, relative to that of H_2O_2:H_2SO_4 and HNO_3:H_2SO_4, which gave 52 mAh/g and 3 mAh/g, respectively. It is well known in electrochemistry that high surface area is one of the prerequisites for the good performance of electrode materials, because electric energy is stored in aggregated charges at the surface of electrode materials [10]. It can be clearly seen from BET results that H_2O_2:H_2SO_4 treated MWCNTs show the highest BET surface area (736.58 m^2g^{-1}) compared to the H_2O_2:HNO_3 treated MWCNTs (343.09 m^2g^{-1}). However these MWCNTs (H_2O_2:HNO_3 treated MWCNTs) in turn shows the highest hydrogen storage capacity and capacitance.
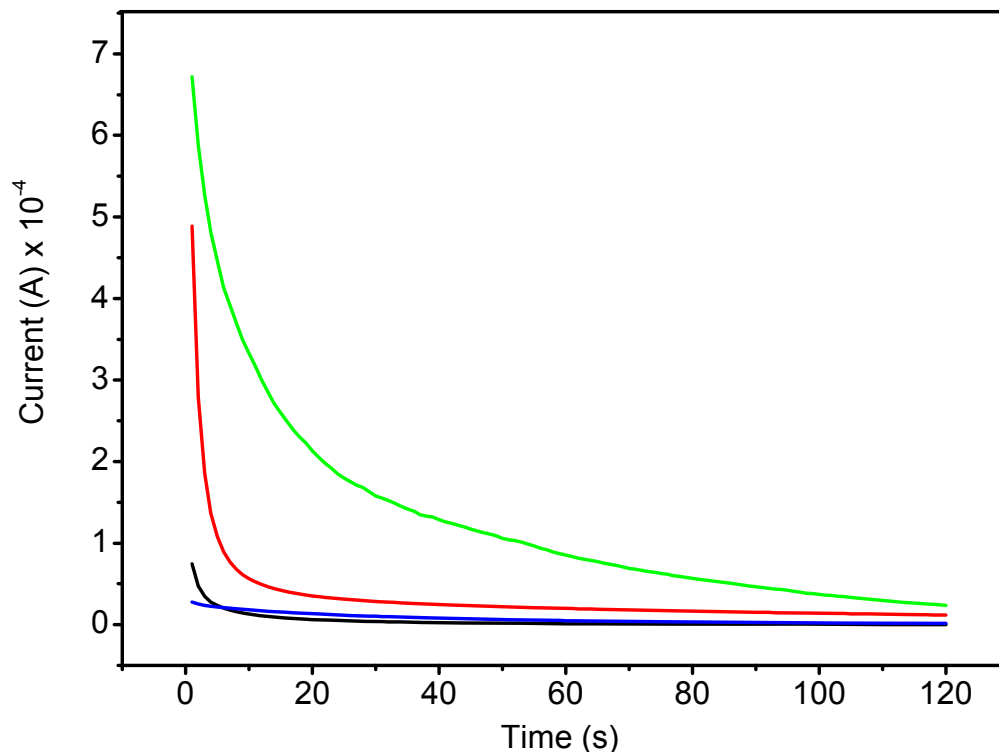
Figure 4.15: Discharge curves of (a) raw MWCNTs (black line), MWCNTs treated by (b) $H_2O_2:H_2SO_4$ (red line) (c) $H_2O_2:HNO_3$ (green line) and (d) $HNO_3:H_2SO_4$ (blue line).

The major reason for these findings has to do with the pore size distribution curves of BET, seen in figure 4.10. It was observed that the $H_2O_2:HNO_3$ treated MWCNTs consist of a combination of both small and large channels while $H_2O_2:H_2SO_4$ treated MWCNTs consist mainly of small channels [Figure 4.8(b)] between the MWCNTs. Since large pore channels permit rapid electrolyte transport, while the small pores provide more active sites for chemical reactions [11], a combination of both small and large channels results in a good material for energy applications. Furthermore, the BET data shown in table 4.1, agrees with the decrease of hydrogen storage capacity of the MWCNTs treated by $HNO_3:H_2SO_4$. Hydrogen could be stored between the graphene layers, however due to the damage of graphite structure (Figure 4.4 and 4.8(c)) of MWCNTs, the amount of hydrogen stored would be reduced.

Table 4.2: Electrochemical hydrogen storage data for the MWCNTs samples

Sample no.	Sample name	Discharge capacity (mAh/g)[a]	Hydrogen storage (wt%)[b]
1	MWCNTs treated by HNO_3:H_2SO_4	2.98	0.01
2	Raw MWCNTs	8.23	0.03
3	MWCNTs treated by H_2O_2	15.15	0.06
4	MWCNTs treated by H_2SO_4	41.97	0.17
5	MWCNTs treated by HNO_3	50.51	0.19
6	MWCNTs treated by H_2O_2:H_2SO_4	52.36	0.20
7	MWCNTs treated by H_2O_2:HNO_3	72.63	0.27

[a]All data were repeated three times. [b] The amount of hydrogen stored was calculated as follows: ((discharge capacity x 2.02 wt.%)/540 mAh/g).

4.3.1.3. Charging-discharging mechanism of hydrogen oxidation

The major research demonstrates that the main way of MWCNTs hydrogen adsorption is physical and reversible adsorption, (i.e, hydrogen is adsorbed as molecule and deposited on MWCNTs tubes). In addition, a little amount of hydrogen is likely to form bond with carbon atom [9]. The electrochemical reaction mechanism of the MWCNTs electrode can be expressed as follows:

$$MWCNTs + xH_2O + xe^- \leftrightarrow (MWCNTs + xH) + xOH^- \qquad \textbf{(Equation 4.1) [12]}$$
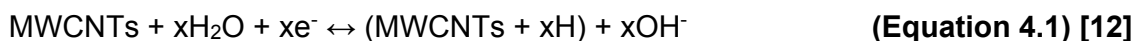
The experimental results indicate that through proper acid treatment, the hydrogen discharge capacity of MWCNTs improve by a factor of 8.82. The significant increase in hydrogen storage performance due to acid treatment can be attributed to two

factors: (i) since the bamboo carbon structures inside the inner hollow nanotube of the as- prepared MWCNTs were removed, the active hydrogen adsorption sites on the surface can be effectively increased, (ii) Because the acid treated MWCNTs are thin, the electrolyte can easily penetrate inside the tubes, which is beneficial for electrochemically gathering hydrogen (via eq. 4.1) [12]. The hydrogen storage capacities reported in our study are low in comparison to what has been reported in the literature. The possible reasons behind this are: the smaller electrodes surface that were used (3.0 mm diameter), the small amount of the material on the electrodes (0.3 - 0.35 mg). However an improvement by a factor of 8.82 is quite satisfying.

4.3.2. Supercapacitor studies

4.3.2.1. Cyclic voltammetric characteristic of MWCNTs electrode

The CV curves of the MWCNTs treated by mixtures of acids are shown in figure 4.16. Measurements were carried out in a 1 M Na_2SO_4 aqueous electrolyte at room temperature. CV tests were carried out using a potential window ranging between 0.1 and 0.9 V at a scan rate of 50 mV/s. The CV curves (Figure 4.16 and Appendix 1) are relatively rectangular in shape without any obvious redox peaks, indicating an ideal capacitive behaviour [13]. The specific capacitance (C_s) of the composites was calculated from the CV measurements using equation 4.2.

$$C_s = \left(\frac{\int_{V_2}^{V_1} I(V)dV}{(V_1 - V_2)vm} \right)$$

[Equation 4.2]

Equation 4.2 represents the area of current against voltage curve, with V_1 and V_2 being the switching potential in cyclic voltammetry, v is the scan rate (mVs^{-1}), m is the mass of the material on the electrode (g) and I (V) denotes the current response (A) [14].

The area of the CV curve [Figure 4.16] for MWCNTs treated by H_2O_2:HNO_3 is larger than all the other MWCNTs samples which imply that more numbers of charges are involved in this electrode [13]. The raw MWCNTs show the lowest capacitance value of 4.9 F/g, probably due to the lack of functional groups on the MWCNTs surface, the

presence of bamboo structures inside the tubes and low surface area [15]. The capacitance reached a maximum of 8.61 F/g for the MWCNTs treated by H_2O_2:HNO_3. Thus it appears that acid treatment modifies the MWCNTs and hence improves the electrode performance. The increase of capacitance was due to the MWCNTs after the activated treatment possessing functional groups, wider pore size distribution and higher surface area [1].
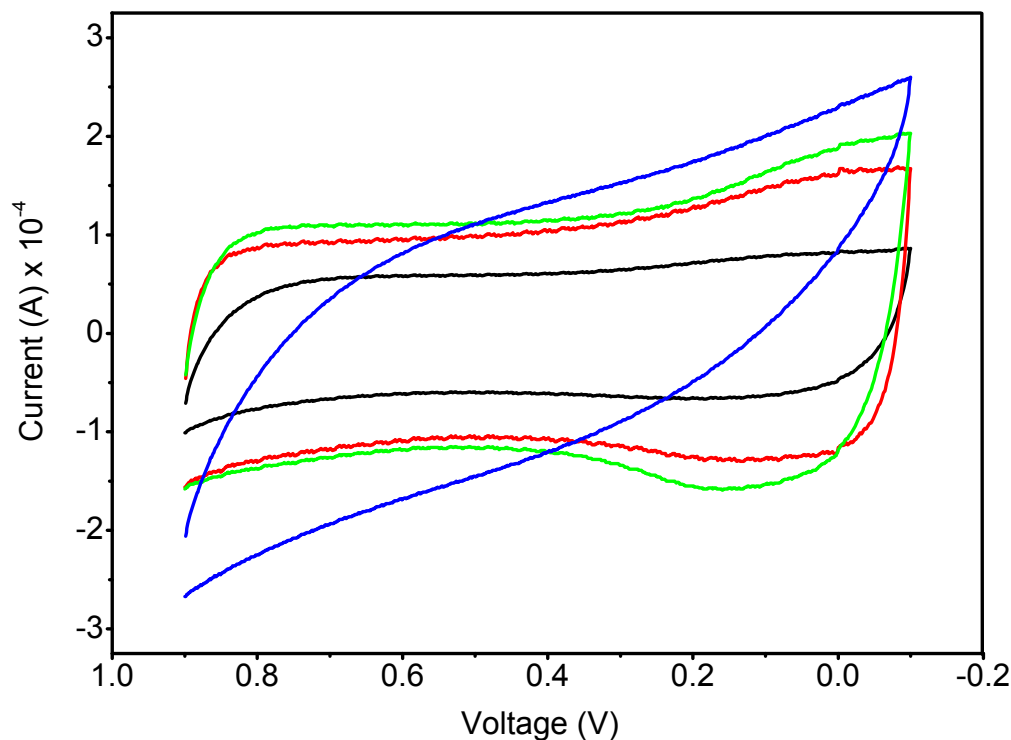

Figure 4.16: CV curves of (a) raw MWCNTs (black line), MWCNTs treated by (b) H_2O_2:H_2SO_4 (red line) (c) H_2O_2:HNO_3 (green line) and (d) HNO_3:H_2SO_4 (blue line).

Oxidation of MWCNTs introduces many functional groups such as hydroxyl (-OH) and carboxyl (-CO) on the surface of MWCNTs. These functional groups act as the active sites which help the MWCNTs serve as electron transmitters [1]. This is evidenced by the increase in the specific capacitance when the intensity of these functional groups increases on the surface of the MWCNTs treated by a mixture of the acids (Figure 4.2). This shows that surface properties of electrode materials affect the performance of materials in energy storage applications. A distorted rectangular CV curve is observed for the MWCNTs treated by HNO_3:H_2SO_4, due to

the delay in current responses. This behaviour is caused by the fact that the graphitic structure of these MWCNTs was destructed after treatment, as confirmed by XRD and TEM results (Figure 4.4 and 4.8(c)). The specific capacitance values for the raw and MWCNTs treated by the different acids were calculated using eq. 4.2 and they are presented in table 4.3.

The specific capacitance values presented in our study are low in comparison to what is reported in the literature [1]. The major reasons for the low capacitance values besides those mentioned in the hydrogen storage studies are still unknown. However, the specific capacitance (8.6 F/g) obtained increased by a factor of 1.76 as compared to the raw MWCNTs (4.9 F/g), which is quite interesting.

Table 4.3: Specific capacitance values of the MWCNTs samples

Sample no.	Sample name	Specific capacitance (F/g)
1	Raw MWCNTs	4.90
2	MWCNTs treated by H_2SO_4	6.45
3	MWCNTs treated by $HNO_3:H_2SO_4$	6.50
4	MWCNTs treated by HNO_3	7.36
5	MWCNTs treated by H_2O_2	8.49
6	MWCNTs treated by $H_2O_2:H_2SO_4$	8.60
7	MWCNTs treated by $H_2O_2:HNO_3$	8.61

4.3.2.2. Life cycle stability tests of MWCNTs treated by H_2O_2:HNO_3

The long term cycle stability is a very important requirement for supercapacitor applications [16]. The cycling stability of the electrode fabricated from MWCNTs treated by H_2O_2:HNO_3 was tested by CV at a scan rate of 50 mVs^{-1} for 200 life-cycles. Figure 4.17 shows the voltammograms recorded for the 1st, 100th and 200th cycles. The CV curves initially exhibit essentially rectangular-shaped profiles, with increasing cycle number, and a deviation from the original rectangular shaped curve was later observed. The specific capacitance decreased by 20% of the original value after 100 cycles and a slight drop of 26% of the original value after 200 cycles (see figure 4.18). The specific capacitance loss is about ~ 20 % between the 1st and 100th cycle and only about ~ 6 % between the 100th and 200th. The cause for the initial quicker capacitance loss is still unknown, but may be associated with morphological changes in the MWCNTs resulting from repeated charging-discharging [17] accompanied by the adsorption-desorption of the counter ions, i.e. H^+ and/or Na^+ ions [18]. In addition, the respective variations on the CVs in figure 4.17 also suggest compositional and/or structural changes in the nanocomposite [18-21].
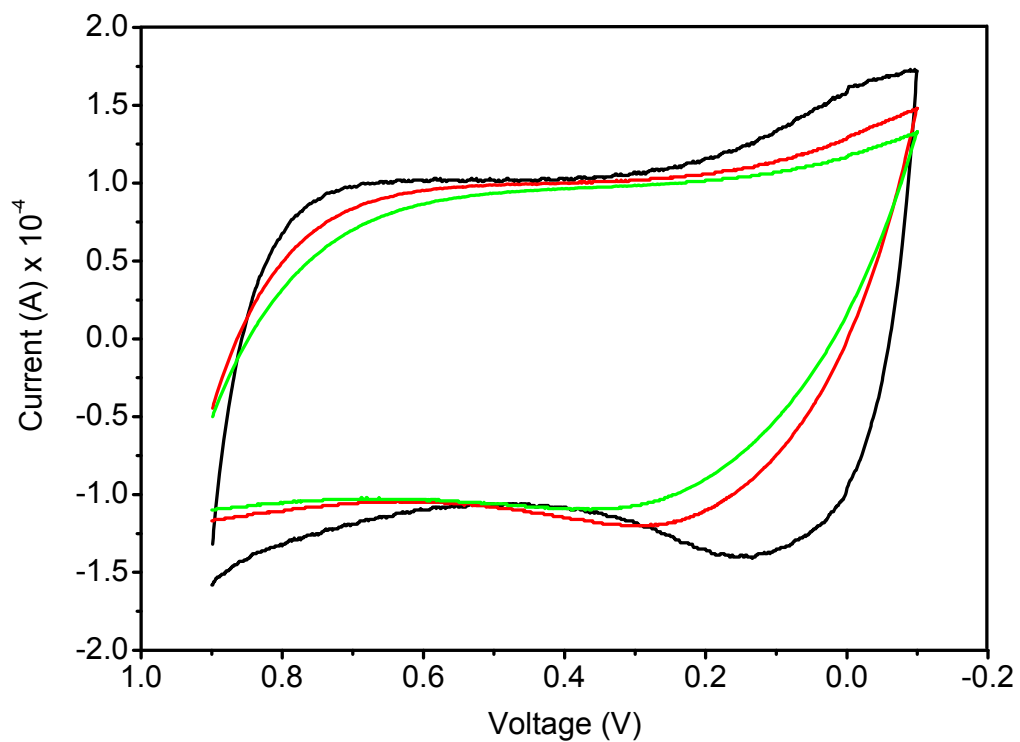
Figure 4.17: CVs of MWCNTs treated by H_2O_2:HNO_3 electrode recorded during different cycles, (a) 1st cycle (black line) (b) 100th cycle (red line) and (c) 200th cycle (green line).
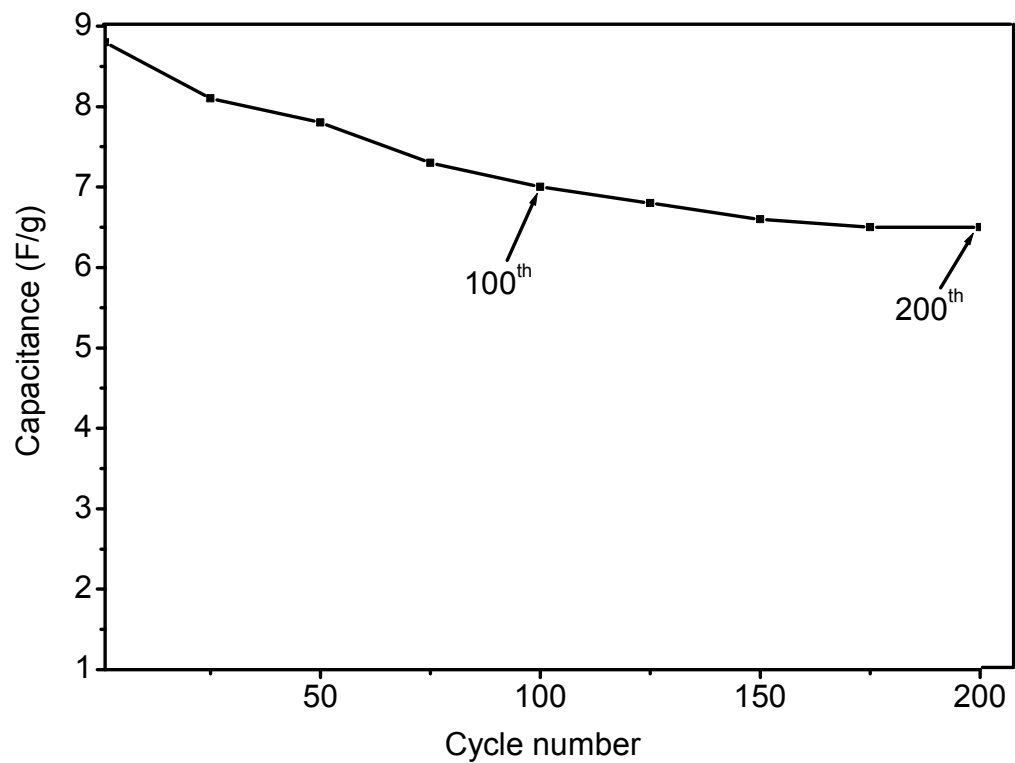
Figure 4.18: Capacity retention from MWCNTs treated by H_2O_2:HNO_3 electrode as a function of cycling number.

4.4. References

[1] Dai Y, Liu W, Pan T and Jehng J, Surface activation on multi-walled carbon nanotube for electrochemical capacitor applications, Applied Surface Science 258 (2012) 3027-3032

[2] Shirazi Y, Tofighy M.A, Mohammadi T and Pak A, Effects of different carbon precursors on synthesis of multi-walled carbon nanotubes: Purification and functionalisation, Applied Surface Science 257 (2011) 7359-7367

[3] Maraes F.C, Cabral M.F, Mascaro L.H and Machado S.A.S, The electrochemical effect of acid functionalisation of carbon nanotubes to be used in sensors development, Surface Science 605 (2011) 435-440

[4] Mazov I, Kuznetsov L.V, Simonov I. A, Stadnichenko A.I, Ishchenko A.V, Romanenko A. I, Tkachev E.N and Anikeeva O.B, Oxidation behavior of multi-walled carbon nanotubes with different diameters and morphology, Applied Surface Science 258 (2012) 6272-6280

[5] Chiang Y, Lin W and Chang Y, The influence of treatment duration on multi-walled carbon nanotubes functionalised by H_2SO_4/HNO_3 oxidation, Applied Surface Science 257 (2011) 2401-2410

[6] Buang N.A, Fadil F, Majid Z.A and Shahir S, Characteristic of mild acid functionalised multi-walled carbon nanotubes towards high dispersion with low structural defects, Digest Journal of Nanomaterials and Biostructures 7 (2012) 33-39

[7] Matchelaho M.A.M, Xiong H, Moyo M, Jewell L.L and Coville N.J, Effect of acid treatment on the surface of multi-walled carbon nanotubes prepared from Fe-Co supported on $CaCo_3$: Correlation with Fischer-Tropsch catalyst, Journal of Molecular Catalysis A: Chemical 335 (2011) 189-198

[8] Naseh M.V, Khodadadi A. A, Mortazavi Y, Sahraei O. A, Pourfayaz F and Sedghi S. M, Funtionalisation of carbon nanotubes using nitric acid oxidation and DBD plasma, International Journal of Chemical and Biological Engineering (2009) 2:2

[9] Feng H, Wei Y, Shao C, Lai Y, Feng S and Dong Z, Study on overpotential of the electrochemical hydrogen storage of multiwall carbon nanotubes, International Journal of Hydrogen Energy 32 (2007) 1294-1298

[10] Su A.D, Zhang X, Rinaldi A, Nguyen S.T, Liu H, Lei Z and Lu L, Hierarchical porous nickel-carbon nanotubes as advanced pseudocapacitor materials for supercapacitors, Chemical Physics Letters 561-562 (2013) 68-73

[11] Simon P and Gogotsi Y, Materials for electrochemical capacitors, Nature Materials 7 (2008) 845-854

[12] Chang J, Tsai H and Tsai W, A metal dusting process for preparing nano-sized carbon materials and the effects of acid post-treatment on their hydrogen storage performance, International Journal of Hydrogen Energy 33 (2008) 6734-6742

[13] Yan J, Fan Z, Wei T, Cheng J, Shao B, Wang K, Song L and Zhang M, Carbon nanotubes/MnO_2 composites synthesised by microwave-assisted method for supercapacitors with high power and energy densities, Journal of Power Sources 194 (2009)1202-1207

[14] Giri S, Ghosh D and Das C.K, Effect of ruthenium (III) incorporation in polyaniline backbone: materials for supercapacitor energy storage application, World Scientific Publishing Company 8 (2013) 1-13

[15] Hermosilla-Lara G, Momen G, Marty P.H, Le Neindre B and Hassouni K, Hydrogen storage by adsorption on activated carbon: Investigation of the thermal effects during the charging process, International Journal of Hydrogen Energy 32 (2007) 1542-1553

[16] Wang J, Yang Y, Huang Z and Kang F, Synthesis and electrochemical performance of MnO_2/CNTs-embedded carbon nanofibers nanocomposites for supercapacitors, Electrochimica Acta 75 (2012) 213-219

[17] Wu M.Q, Snook G.A, Chen G.Z and Fray D.J, Redox deposition of manganese oxide on graphite for supercapacitors, Electrochemistry Communication 6 (2004) 499-504

[18] Zhang S, Chuang P, Ng K.C and Chen G.Z, Nanocomposites of manganese oxides and carbon nanotubes for aqueous supercapacitor stacks, Electrochimica Acta 55 (2010) 7447-7453

[19] Zhang Y, Li G, Lv Y, Wang L and Zhang A, Electrochemical investigation of MnO_2 electrode material for supercapacitors, International Journal of Hydrogen Energy 36 (2011) 11760-11766

[20] Zhang L.L, Xiong Z and Zhao X.S, A composite electrode consisting of nickel hydroxide, carbon nanotubes, and reduced graphene oxide with an ultrahigh electrocapacitance, Journal of Power Sources 222 (2013) 326-332

[21] Zhu X, Dai H, Hu J, Ding L and Jiang L, Reduced graphene oxide–nickel oxide composite as high performance electrode materials for supercapacitors, Journal of Power Sources 203 (2012) 243-249

CHAPTER 5

RESULTS AND DISCUSSIONS

ELECTROCHEMICAL STUDIES OF METAL OXIDES DOPED MULTI-WALLED CARBON NANOTUBES

5.1. Introduction

Although many studies have been conducted on the effect of metal catalysts on the electrochemical performance of CNTs, few studies have been conducted on the electrochemical performance of metal oxides/CNTs especially towards hydrogen storage. The dissertation objectives were focused mainly on the effect of different metal oxides on the electrochemical performance of acid-treated MWCNTs. The study involves the investigation of the effect of preparation temperature on the electrochemical performance of the metal oxide-MWCNTs nanocomposites. The study hoped to obtain a hybrid material that will show better electrochemical activities. MWCNTs treated with H_2O_2:HNO_3 were used to make the composites. All the SEM images of the metal oxide containing MWCNTs were obtained from samples treated at 300 and 500 °C, to study the effects of two different temperatures.

5.2. Characterisation of CuO and 5wt.% CuO-MWCNTs nanocomposite

5.2.1. SEM analysis of CuO nanoparticles

Figure 5.1 show the SEM images of CuO prepared at different temperatures. CuO was prepared by heating $Cu(NO_3)_2$.$3H_2O$ at different temperatures for 2 h. The CuO of clusters of varying amounts of thin nanosheets were observed (Figure 5.1(a)). Similar morphology was observed by Dubal *et al.* [1] when they prepared CuO via Chemical bath deposition (CBD) method using $CuSO_4$ as a source of copper. They demonstrated that the clusters of small nanosheets generate abundant pores, which ensures an easier electrolyte ion transport and more superficial electro-active sites.

The nanosheets formed agglomerates at high preparation temperatures which resulted in the formation of thick sheets (Figure 5.1(c)).
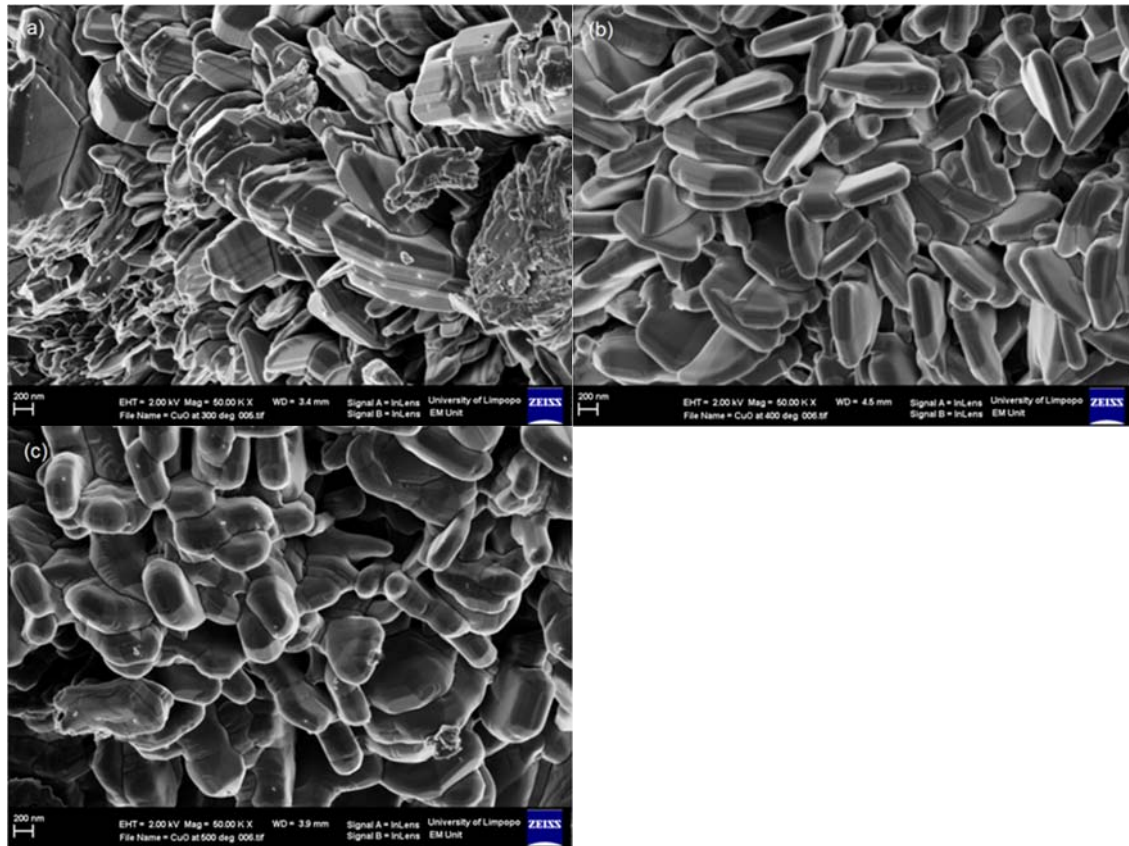

Figure 5.1: SEM images of CuO prepared at (a) 300 °C (b) 400 °C and (c) 500 °C.

5.2.2. SEM analysis of 5wt.% CuO-MWCNTs nanocomposite

Figure 5.2 show the SEM images of 5wt.% CuO-MWCNTs nanocomposites. The SEM images show clusters of various lengths and diameters of MWCNTs. The MWCNTs are highly curved and bunched together in a random and disordered manner. The images show the presence of the CuO nanosheets among the MWCNTs. Some big CuO sheets are visible on the CuO@500 °C-MWCNTs composites in relation to the CuO@300 °C-MWCNTs composite.
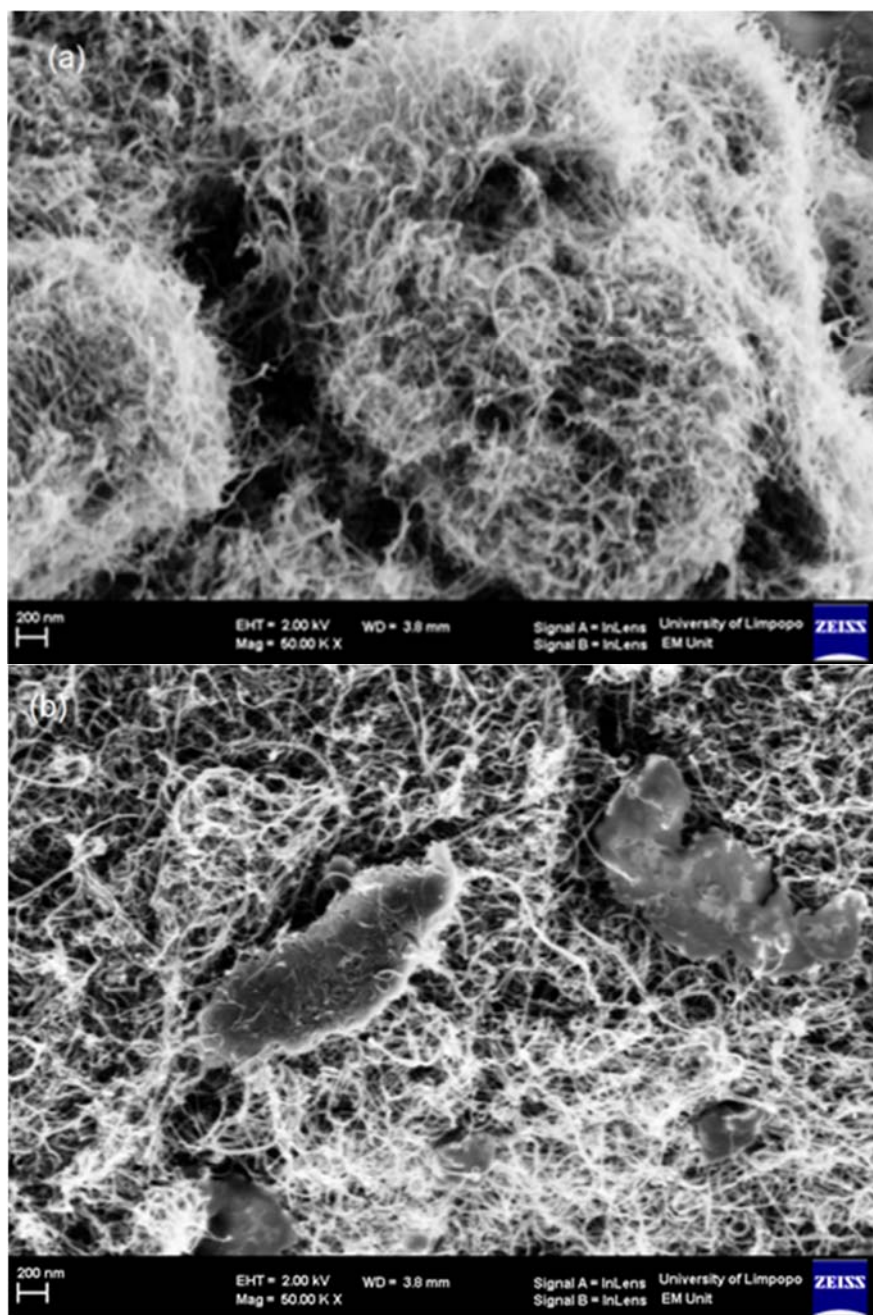
Figure 5.2: SEM images of (a) CuO@300 °C-MWCNTs and (b) CuO@500 °C-MWCNTs.

5.2.3. TEM analysis of 5wt.% CuO@300 °C-MWCNTs

The TEM images of the 5wt.% CuO@300 °C-MWCNTs at low- and high magnification are shown in figure 5.3. The TEM images show that some of the CuO nanoparticles were embedded inside the walls of MWCNTs [Figure 5.3(a) and (b)]. This shows that most of the CuO particles are within the inner diameters of

MWCNTs, although occasionally some few large particles are observed as well. Lower magnification TEM images of the CuO@300 °C-MWCNTs composites do not show formation of any noticeable aggregates [Figure 5.3(a)]. It should however be noted that some of the CuO deposits blocked the inner tubes of the three dimensional entangled structure of the MWCNTs. The diameter of the CuO particles measured from the high magnification TEM image was found to be 6.8 nm [Figure 5.3(b)].
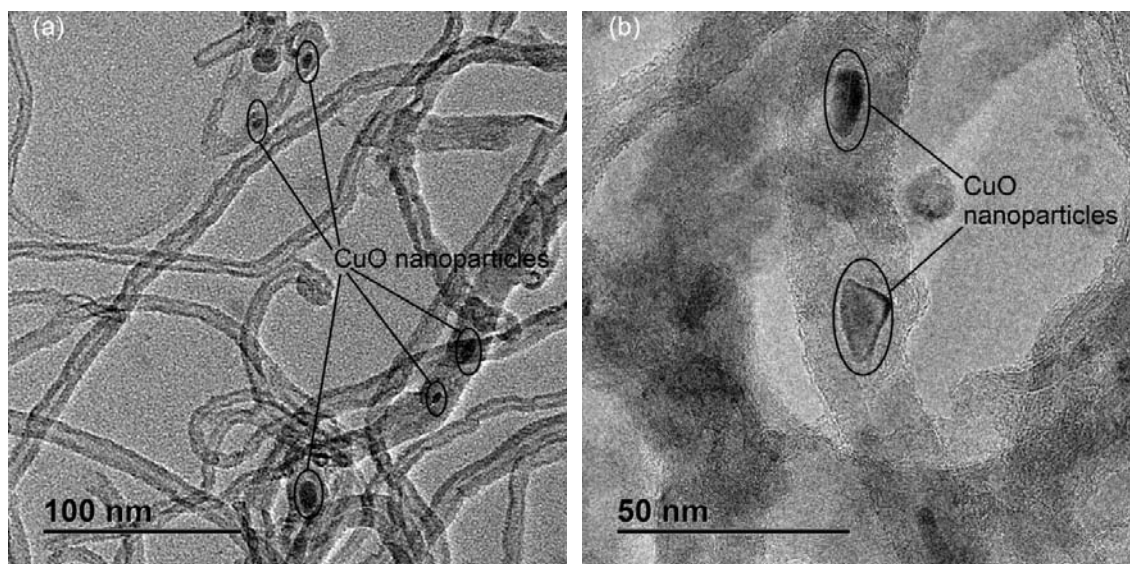

Figure 5.3: TEM images of 5wt.% CuO@300 °C-MWCNTs at (a) low- and (b) high magnification.

5.2.4. XRD analysis of CuO and 5wt.% CuO-MWCNTs nanocomposite

Figure 5.4 shows the XRD patterns of CuO and the corresponding 5wt.% CuO-MWCNTs nanocomposite. The XRD pattern of the CuO can be well indexed as the monoclinic copper oxide (CuO) phase [2]. No characteristic peaks assigned to impurities such as $Cu(OH)_2$ or Cu_2O were detected (Figure 5.4(a)). The average crystallite size calculated using the Scherrer's equation from the (-111) peak was found to be 25.06 nm and 19.73 nm for CuO@300 °C and CuO@300 °C-MWCNTs, respectively. The crystallite size of CuO increased with treatment temperature (27.1 nm at 500 °C, (Figure 5.4(c)), however they remain the same inside MWCNTs. This clearly suggests that the CuO nanoparticles were restricted to a specific size as soon as they are attached to or within the MWCNTs structure. The CuO-MWCNTs

composites, showed additional peak (002) at around 2θ = 26 °, which is due to the graphitic characteristic of MWCNTs structure (Figure 5.4(c)).

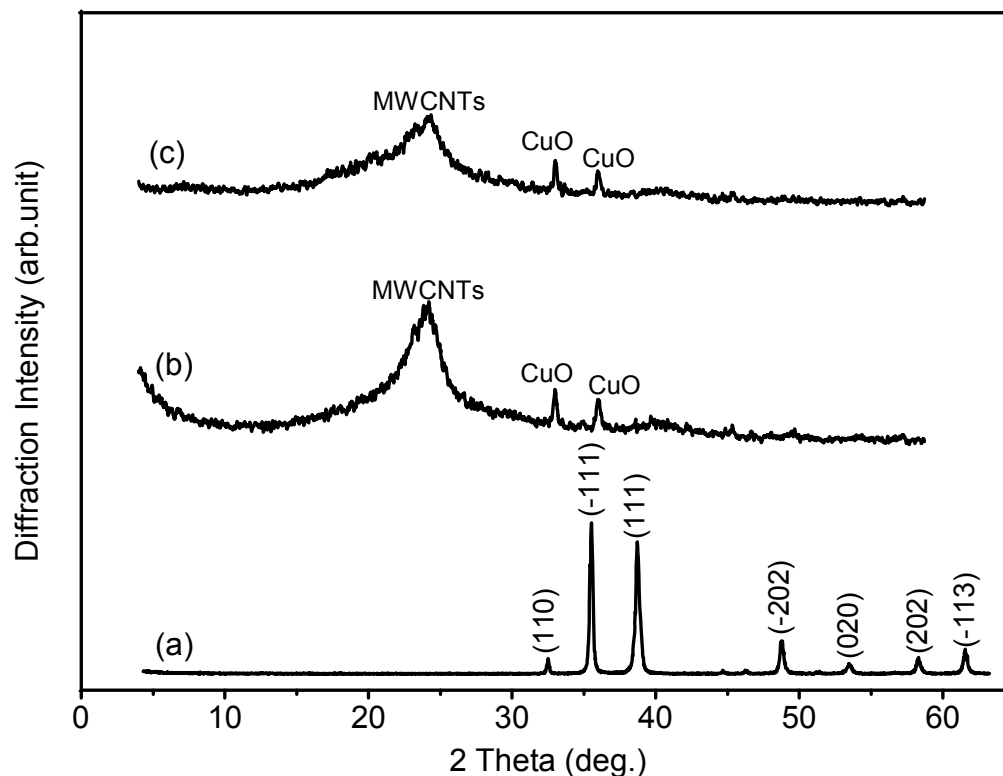**Figure 5.4:** XRD pattern of (a) CuO@300 °C and (b) 5wt.% CuO@300 °C-MWCNTs and (c) 5wt.% CuO@500 °C-MWCNTs.

5.3. Characterisation of Fe_2O_3 and 5wt.% Fe_2O_3-MWCNTs nanocomposite

5.3.1. SEM analysis of Fe_2O_3

Figure 5.5 show the SEM images of Fe_2O_3 prepared at different temperatures. Fe_2O_3 was prepared by heating $Fe(NO_3)_3.9H_2O$ at different temperatures for 2 h. Nanotubular structures of Fe_2O_3 can be observed at 300 °C. There is formation of round blobs among the Fe_2O_3 nanotubes at pre-treatment temperature of 400 °C. The observed blobs became bigger at 500 °C pre-treatment temperature. Xie *et al.* [3] reported a similar tabular morphology, when they prepared α-Fe_2O_3 through an anodization method on iron films. They demonstrated that the unique nanostructures of α-Fe_2O_3 nanotube arrays provide high surface area, fast ion transport pathways

and robust structures. They further demonstrated that these features made the α-Fe_2O_3 nanotube array electrode very attractive for supercapacitor applications.
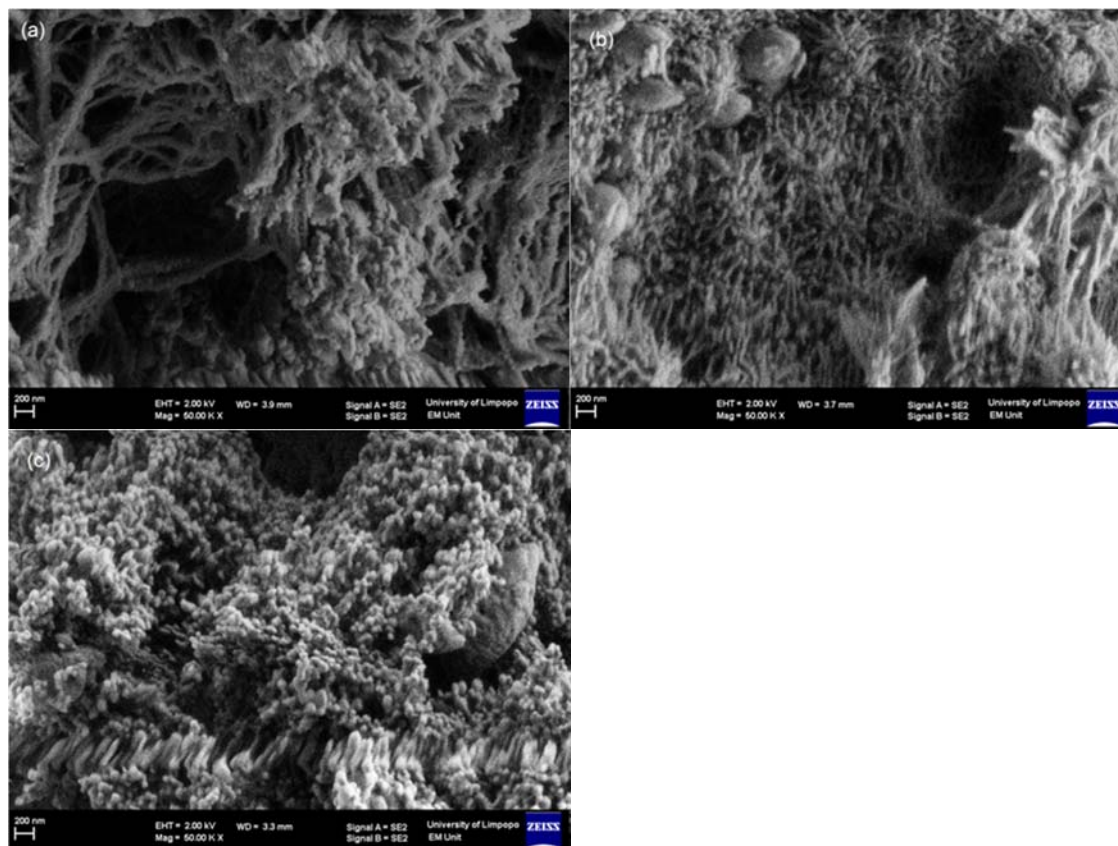

Figure 5.5: SEM images of Fe_2O_3 prepared at (a) 300 °C (b) 400 °C and (c) 500 °C.

5.3.2. SEM analysis of Fe_2O_3-MWCNTs nanocomposites

Figure 5.6 show the surface morphology of Fe_2O_3-MWCNTs nanocomposites. The images show the presence of the Fe_2O_3 nanoparticles among the MWCNTs samples. Distribution of various particle sizes of Fe_2O_3 are observed on the surface, with clear visibility on Fe_2O_3@300 °C-MWCNTs compared to CuO@300 °C-MWCNTs nanocomposite. The Fe_2O_3 nanoparticles on the Fe_2O_3@500 °C-MWCNTs nanocomposite form a bundle of agglomerate on the top left corner.
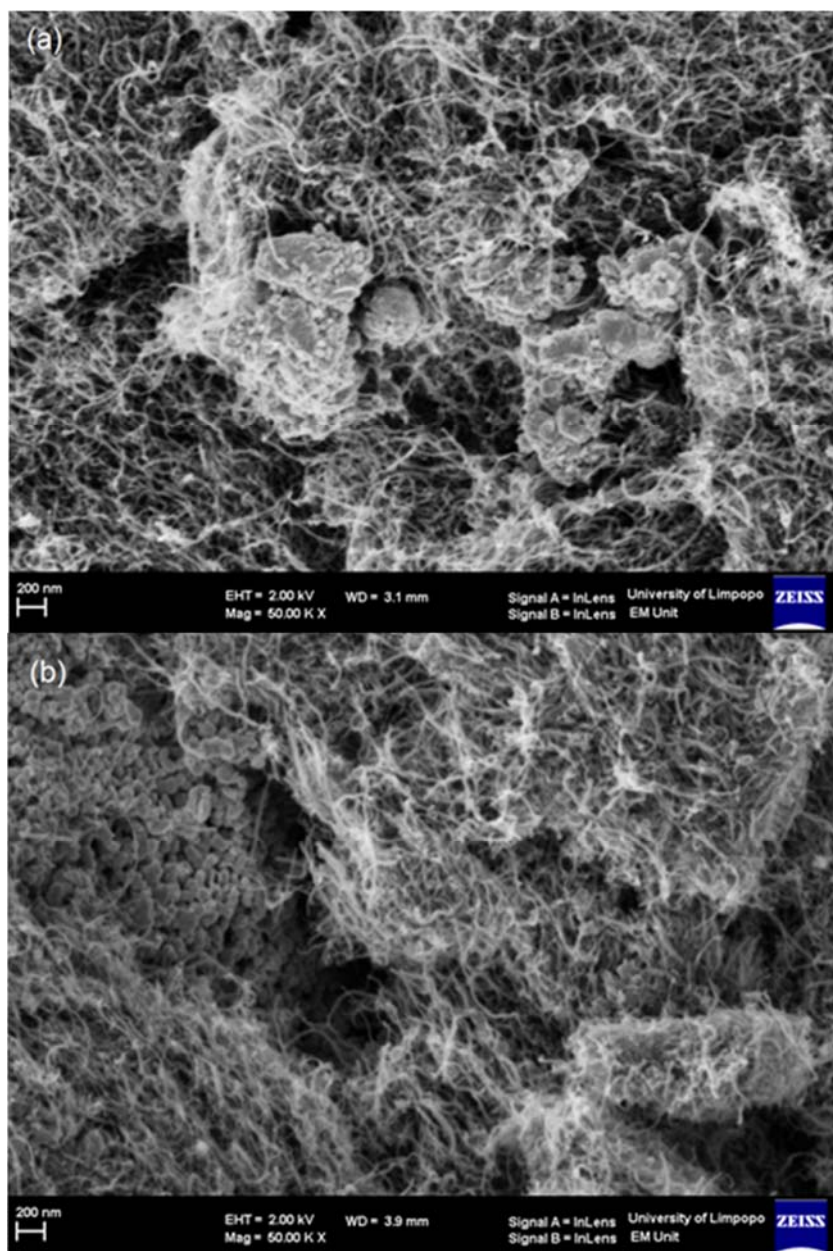
Figure 5.6: SEM images of (a) Fe_2O_3@300 °C-MWCNTs and (b) Fe_2O_3@500 °C-MWCNTs.

5.3.3. TEM analysis of 5wt.% Fe$_2$O$_3$@300 °C-MWCNTs

The TEM images of the 5wt.% Fe$_2$O$_3$@300 °C-MWCNTs at low- and high magnification are shown in figure 5.7. The TEM images show the presence of Fe$_2$O$_3$ nanoparticles on the surface of the MWCNTs, which is consistent with the SEM images (Figure 5.6). The Fe$_2$O$_3$ particles are big, however small Fe$_2$O$_3$ nanoparticles are occasionally observed. The diameter of the Fe$_2$O$_3$ particles measured from the high magnification TEM image was found to be 11.5 nm.
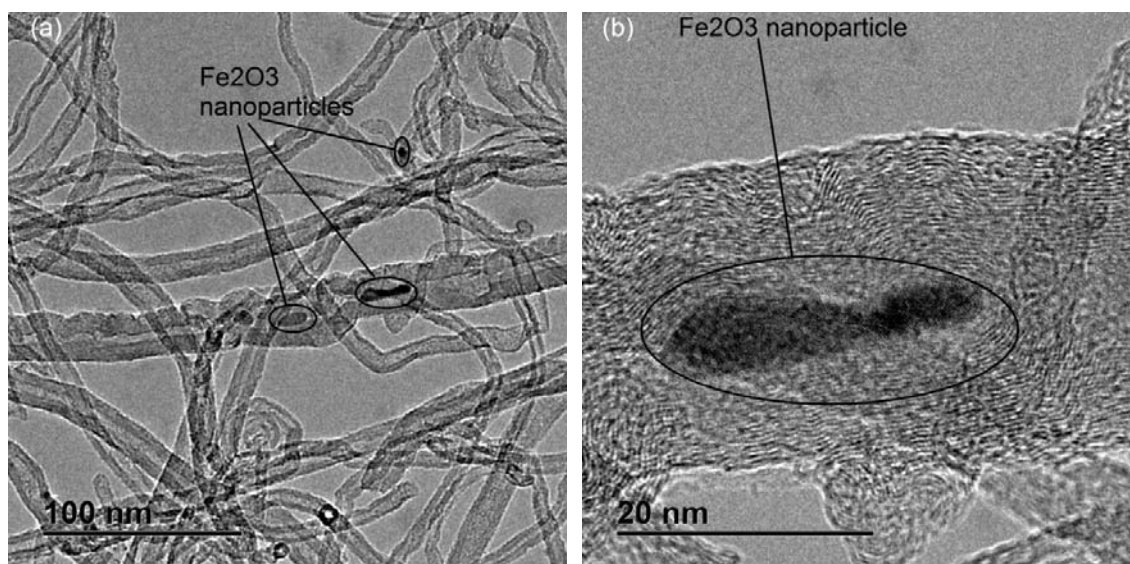

Figure 5.7: TEM images of 5wt.% Fe$_2$O$_3$@300 °C-MWCNTs at (a) low- and (b) high magnification.

5.3.4. XRD analysis of Fe$_2$O$_3$ and 5wt.% Fe$_2$O$_3$-MWCNTs nanocomposite

Figure 5.8 show the XRD pattern of Fe$_2$O$_3$ and corresponding 5wt.% Fe$_2$O$_3$-MWCNTs nanocomposite. The iron oxide was confirmed to be Fe$_2$O$_3$ [4] and no impurities were detected. The average crystallite size calculated using the Scherrer's equation from the (104) peak was found to be 30.2 nm, and 25.8 nm for Fe$_2$O$_3$@300 °C and Fe$_2$O$_3$@300 °C-MWCNTs respectively, with some high crystallite sizes obtained at high temperature treatments. For the Fe$_2$O$_3$-MWCNTs composites, in addition to the Fe$_2$O$_3$ peaks, the characteristic graphitic (002) peak of the MWCNTs is observed at around 2θ = 26 °.
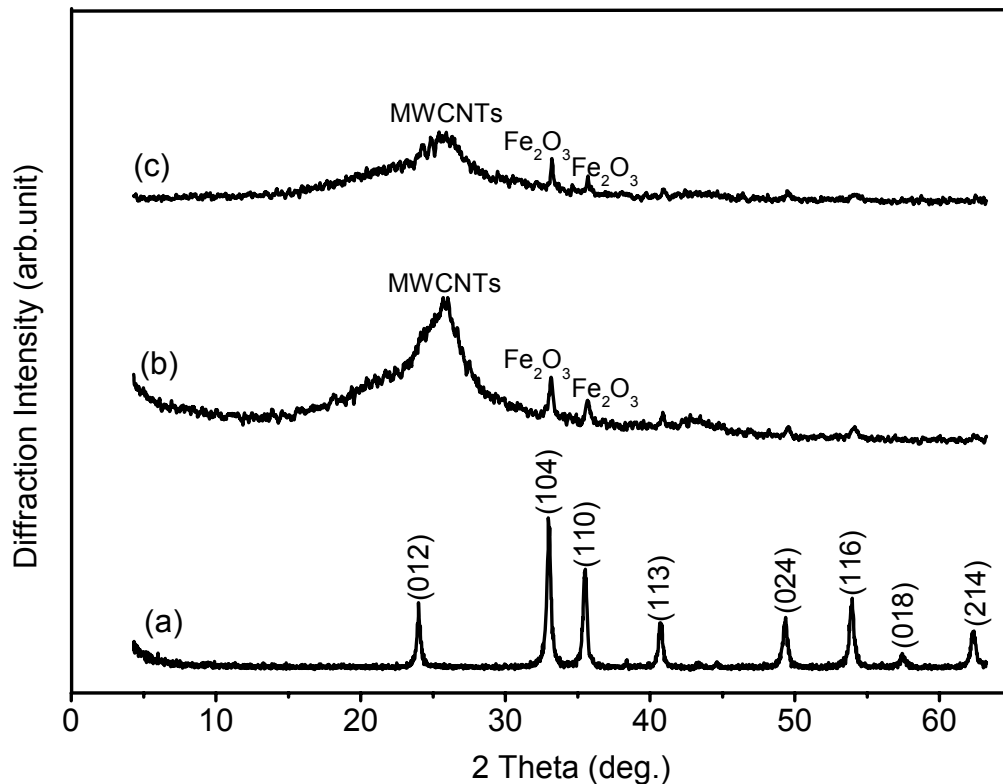
Figure 5.8: XRD pattern of (a) Fe_2O_3@300 °C and (b) 5wt.% Fe_2O_3@300 °C-MWCNTs and (c) 5wt.% Fe_2O_3@500 °C-MWCNTs.

5.4. Characterisation of NiO and 5wt.% NiO-MWCNTs nanocomposite

5.4.1. SEM analysis of NiO

Figure 5.9(a) shows the NiO nanoparticles with a combination of small and large octahedral-like geometry. NiO was prepared by heating $Ni(NO_3)_2.6H_2O$ at different temperatures for 2 h. The formation of bigger nanoparticles is observed at high pre-treatment temperature (Figure 5.9 (c)). However, this shape of NiO nanoparticles differs from the flake-like morphology reported by Su *et al.* [5] who prepared the NiO-MWCNTs composites by refluxing a mixture of nickel nitrate hexahydrate, urea and MWCNTs, which was followed by calcination at 300 °C. The flake-like morphology was also obtained by Inamdar *et al.* [6] when they synthesised a porous nickel oxide film by a chemical bath method deposition technique from an aqueous nickel nitrate solution. They demonstrated that the flakes provide easy access for ions to access

90

the electrode/electrolyte interface, which is a very important factor for faradaic surface reactions.
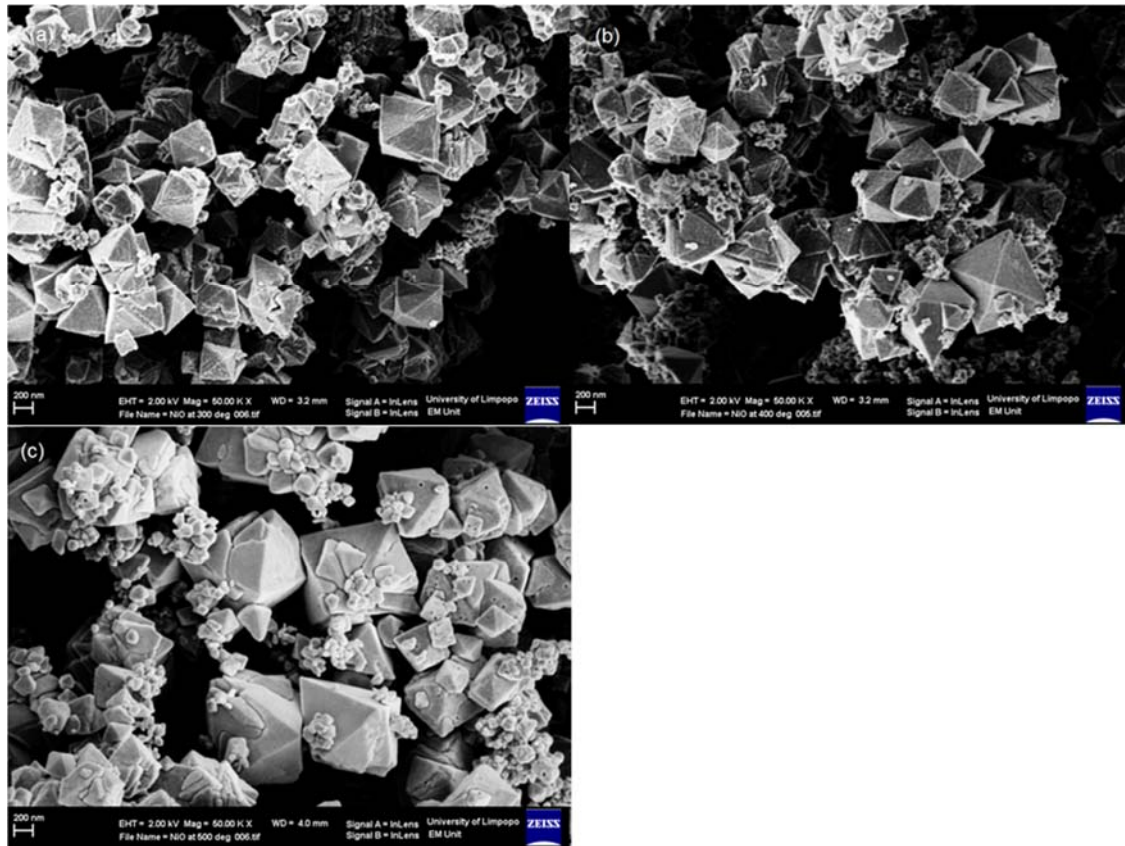

Figure 5.9: SEM images of NiO prepared at (a) 300 °C (b) 400 °C and (c) 500 °C.

5.4.2. SEM analysis of 5wt.% NiO-MWCNTs nanocomposite

The data in figure 5.10 shows the surface morphology of the NiO-MWCNTs nanocomposite. The images show the presence of the NiO lumps with distinct shapes among the MWCNTs clusters. Some agglomerates of NiO particles on NiO@500 °C-MWCNTs composite [Figure 5.12 (b)], are visibly clear as compared to NiO@300 °C-MWCNTs composite.
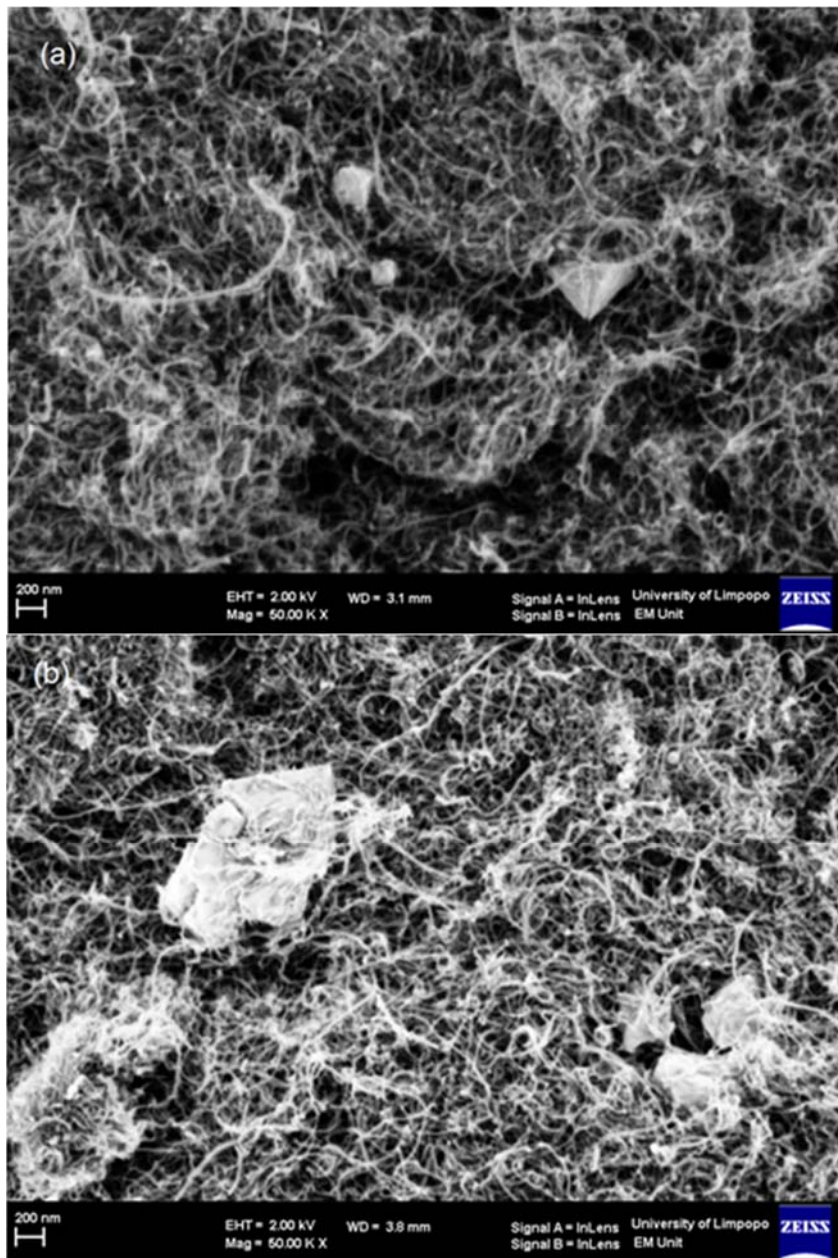
Figure 5.10: SEM images of (a) NiO@300 $^{\circ}$C-MWCNTs and (b) NiO@500 $^{\circ}$C-MWCNTs.

5.4.3. TEM analysis of 5wt.% NiO@300 °C-MWCNTs

The TEM images of the 5wt.% NiO@300 °C-MWCNTs at low- and high magnification are shown in figure 5.11. The TEM images show that some of the NiO nanoparticles were embedded inside the walls of MWCNTs. Lower magnification TEM images of the NiO@300 °C-MWCNTs composites do not show formation of any noticeable aggregates. It should however be noted that some of the NiO deposits blocked the inner tubes of the three dimensional entangled structure of the MWCNTs. The diameter of the NiO particles measured from the high magnification TEM image was found to be 4.2 nm.
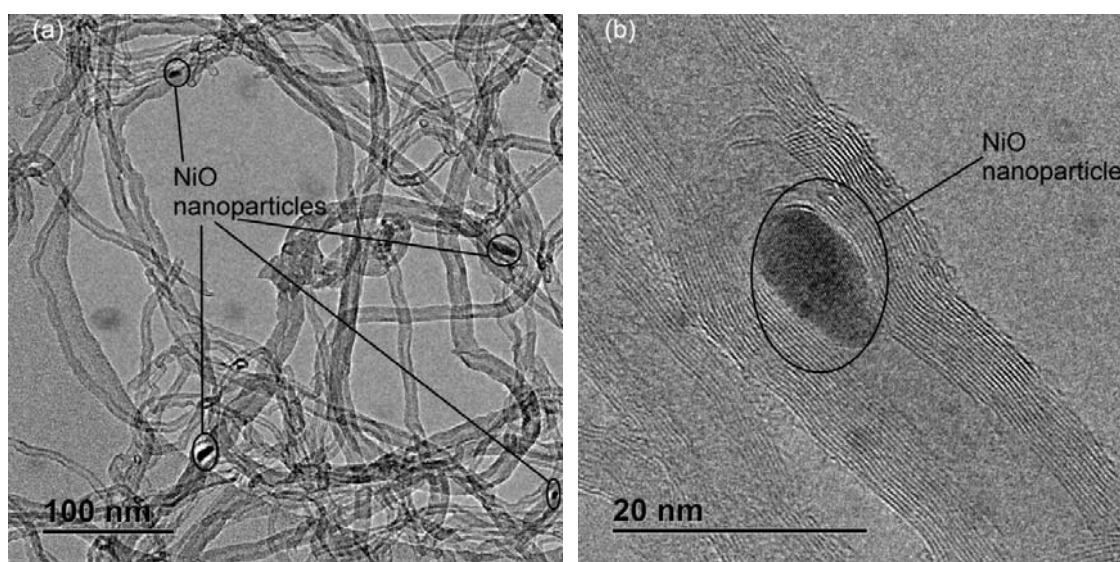

Figure 5.11: TEM images of 5wt.% NiO@300 °C-MWCNTs at (a) low- and (b) high magnification.

5.4.4. XRD analysis of NiO and 5wt.% NiO-MWCNTs nanocomposite

Figure 5.12 shows the XRD patterns of NiO and the corresponding 5wt.% NiO-MWCNTs composites . The diffraction pattern obtained, confirms the formation of rock-like polycrystalline structure of NiO [5, 7], as seen on the SEM images in figure 5.9. The average crystallite size calculated from the (111) peak using the Scherrer's equation was found to be 26.5 nm, and 20.2 nm, for NiO@300 °C and NiO@300 °C-MWCNTs respectively. Small NiO crystallite sizes were obtained inside MWCNTs, due to walls restrictions, however their sizes increased at 500 °C treatments (Figure

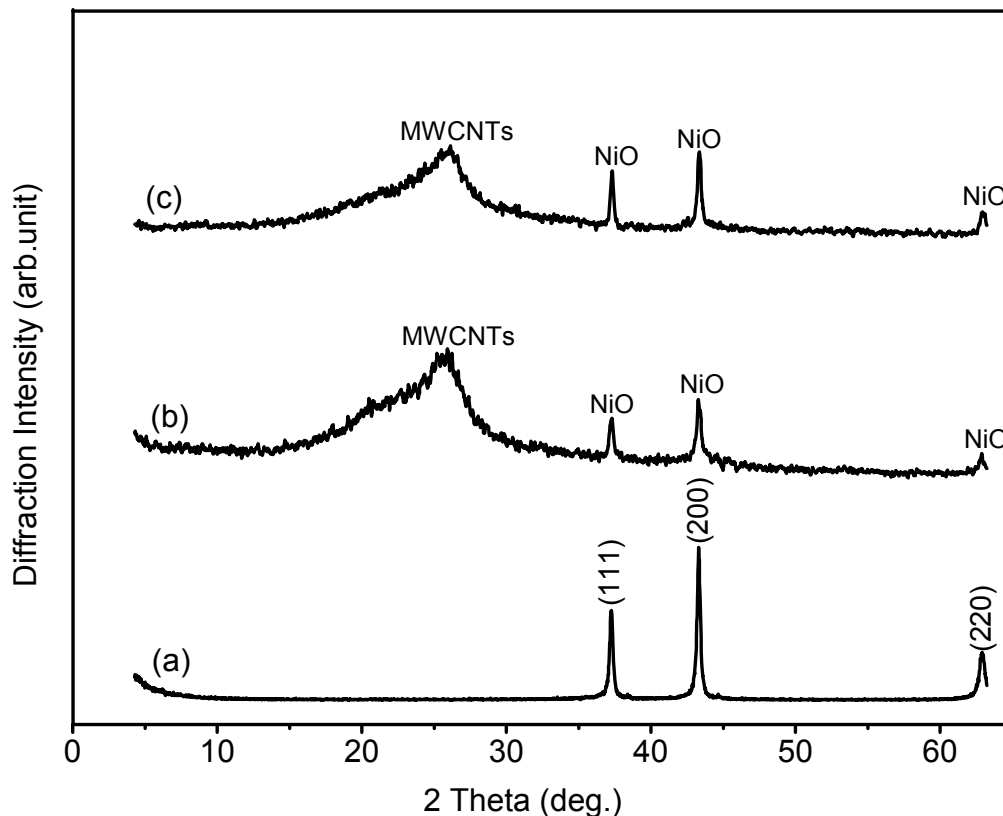5.12(c)). Additional peak (002), due to graphitic structure of MWCNTs is observed at around $2\theta = 26$ °.

Figure 5.12: XRD pattern of (a) NiO@300 °C and (b) 5wt.% NiO@300 °C-MWCNTs and (c) 5wt.% NiO@500 °C-MWCNTs.

5.5. Characterisation of Co_3O_4 and 5wt.% Co_3O_4-MWCNTs nanocomposite

5.5.1. SEM analysis of Co_3O_4

Figure 5.13 show the SEM images of Co_3O_4 prepared at different temperatures. Co_3O_4 was prepared by heating $Co(NO_3)_2.6H_2O$ at different temperatures for 2 h. The pure Co_3O_4 product is composed of nanoparticles with the sizes of dozens of nanometers with a grain-like morphology, these particles arrange randomly and form a relatively loose packed microstructure. When pre-treatment temperature increased up to 400 °C, the particles became obviously aggregated. After 500 °C pre-treatment,

most of the aggregates of small particles have transformed into large ones with a smooth surface, forming fluffy sheets. In general the size of particles is determined by the rates of collision and coalescence. At high temperatures coalescence occurs almost on contact resulting in large particles and hence small surface area. At low temperatures, the collision rate is faster than the rate of coalescence, leading to fractal-like agglomerates consisting of very small particles and thus large surface area [29]. The sizes of the Co_3O_4 crystallite were identified by scherrer's formula (55.3 nm by XRD) to be higher than 30 nm, this is not in line with the grain sizes of cubic Co_3O_4 [8]. Abbas *et al.* [9] prepared nanosized Co_3O_4 with an average grain size of 25 nm. The pure Co_3O_4 was prepared by in-situ chemical co-precipitation of $Co^{2+/3+}$ ions in alkaline solution using $Co(NO_3)_2.6H_2O$ as the precursor. They demonstrated that the nanosized, mesoporous and high surface area structure of Co_3O_4 can provide ion-transport pathways for electrochemical reactions.
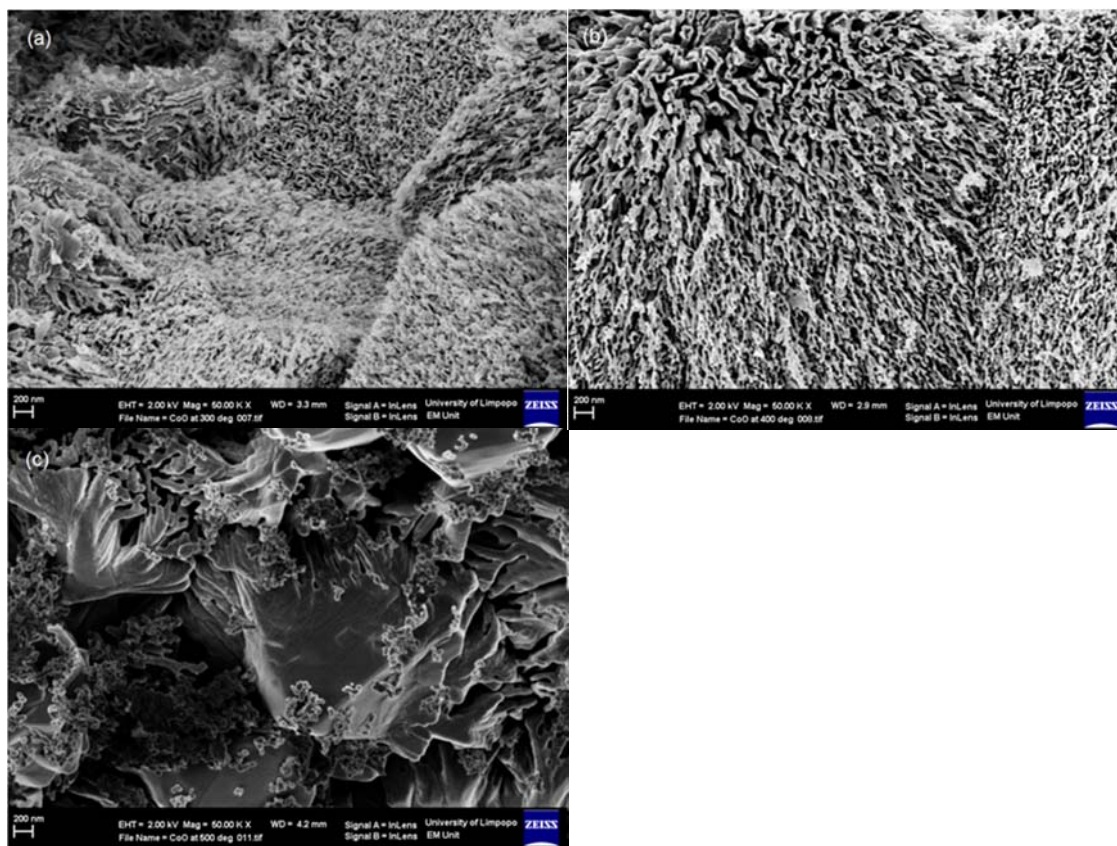

Figure 5.13: SEM images at 200nm of Co_3O_4 prepared at (a) 300 °C (b) 400 °C (c) 500 °C at high magnification.

5.5.2. TEM analysis of 5wt.% Co$_3$O$_4$@300 °C-MWCNTs

The TEM images of the 5wt.% Co$_3$O$_4$@300 °C-MWCNTs at low- and high magnification are shown in figure 5.14. Lower magnification TEM images of the Co$_3$O$_4$@300 °C-MWCNTs composites do not show formation of any noticeable aggregates. It should however be noted that some of the Co$_3$O$_4$ deposits blocked the inner tubes of the three dimensional entangled structure of the MWCNTs. The diameter of the Co$_3$O$_4$ particles measured from the high magnification TEM image was found to be 4.9 nm.
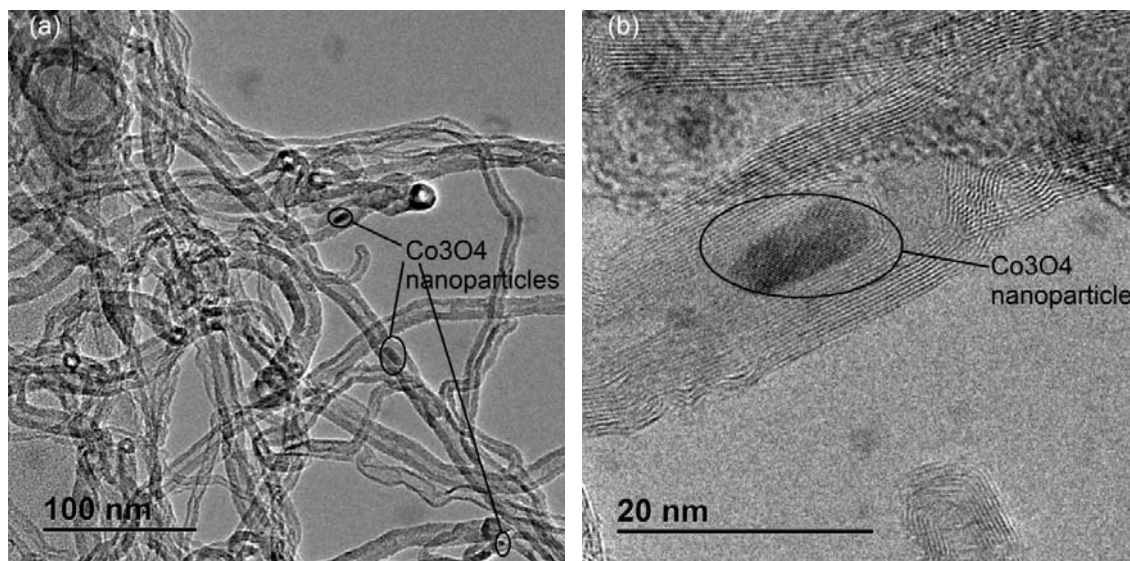

Figure 5.14: TEM images of 5wt.% Co$_3$O$_4$@300 °C-MWCNTs at (a) low- and (b) high magnification.

5.5.3. XRD analysis of Co$_3$O$_4$ and 5wt.% Co$_3$O$_4$-MWCNTs nanocomposite

Figure 5.15 shows the XRD patterns of Co$_3$O$_4$ and the corresponding 5wt.% Co$_3$O$_4$-MWCNTs composites. All sharp diffraction peaks in the Co$_3$O$_4$ are indicative of nanosized Co$_3$O$_4$, which is in good agreement with the cubic phase of Co$_3$O$_4$ [9]. The average crystallite size calculated from the (311) peak using the Schererr's equation was found to be 55.3 nm, and 42.5 nm for Co$_3$O$_4$@300 °C and Co$_3$O$_4$@300 °C-MWCNTs, respectively. The crystallite size of Co$_3$O$_4$ increased at high preparation temperature (Figure 5.15(c)), but remained low once attached to MWCNTs or inside the walls of MWCNTs structure. Similar graphitic (002) peak noted in other composites was observed at around 2θ = 26 °.
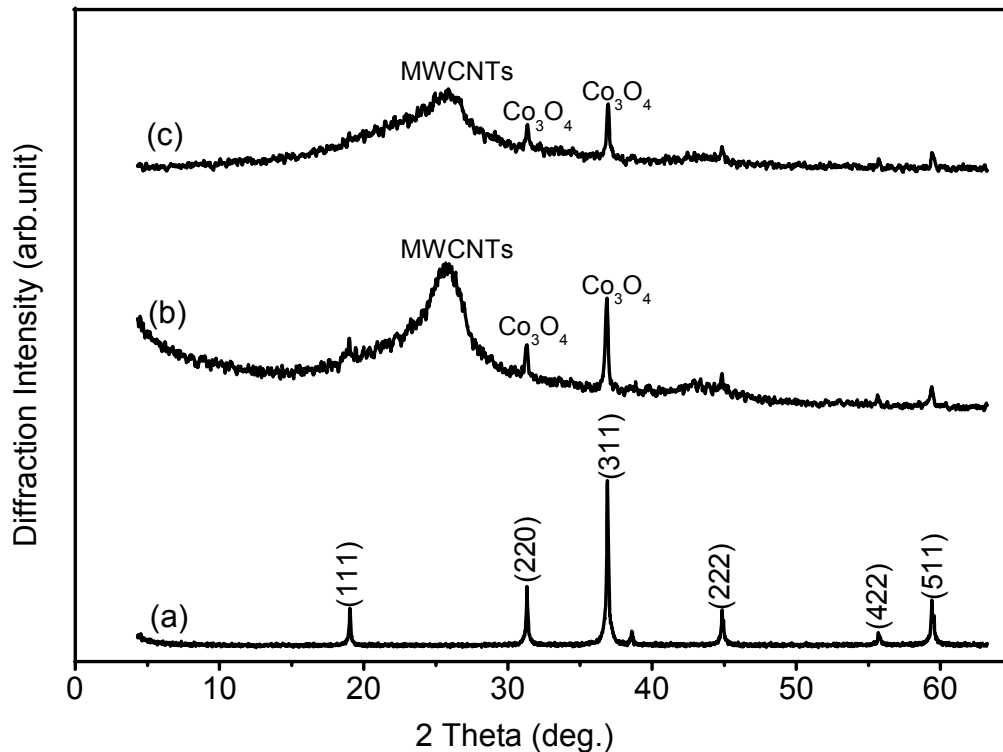
Figure 5.15: XRD patterns of (a) Co_3O_4@300 °C and (b) 5wt.% Co_3O_4@300 °C-MWCNTs and (c) 5wt.% Co_3O_4@500 °C-MWCNTs.

5.6. Characterisation of 5wt.% (MnO_2/CuO)-MWCNTs and 5wt.% (MnO_2/Fe_2O_3)-MWCNTs

5.6.1. SEM analysis of MnO_2, MnO_2/CuO and Fe_2O_3/CuO

The SEM image in figure 5.16(a) shows pure MnO_2 that appears to have spherical spongy-like morphology and appears to have formed agglomerates. The MnO_2/CuO in figure 5.16(b) shows a mixture of nanosheets of CuO and spherical grains of MnO_2. The Fe_2O_3/CuO sample in figure 5.16(c) shows a mixture of agglomerates of both MnO_2 and Fe_2O_3 nanoporous particles.

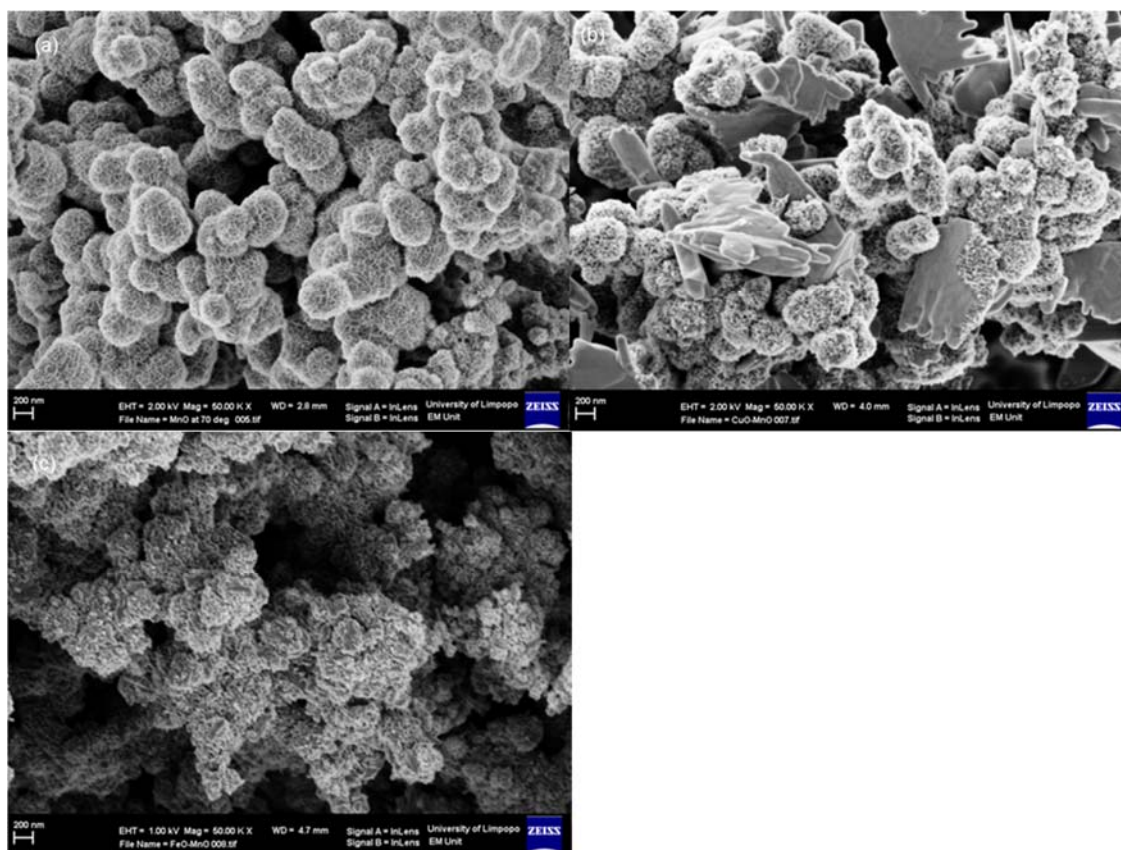**Figure 5.16:** SEM image of (a) MnO$_2$ (b) mixture of CuO/MnO$_2$ and (c) mixture of Fe$_2$O$_3$/CuO.

5.6.2. XRD analysis of 5wt.% (MnO$_2$/CuO)-MWCNTs and 5wt.% (MnO$_2$/Fe$_2$O$_3$)-MWCNTs

Figure 5.17 shows the XRD pattern of 5wt.% (MnO$_2$/CuO) on MWCNTs and 5wt.% (MnO$_2$/Fe$_2$O$_3$) on MWCNTs. The characteristic graphitic (002) peak of the MWCNTs is observed around 2θ = 26 $^{\circ}$. The MnO$_2$ reflections (211) and (220) are observed at around 2θ = 38.4 $^{\circ}$ and 44.6 $^{\circ}$ respectively. The (111) peak of the CuO is observed at around 2θ = 35.4 $^{\circ}$ on the 5% (MnO$_2$/CuO)-MWCNTs nanocomposite. The (104) and (110) peaks of the Fe$_2$O$_3$ are observed at around 2θ = 32.9 $^{\circ}$ and 35.5 $^{\circ}$, respectively, on the 5% (MnO$_2$/Fe$_2$O$_3$)-MWCNTs nanocomposite. The sharp intensity of the MnO$_2$ peaks might be due to inaccuracies with the measurements or the mixing was insufficient.
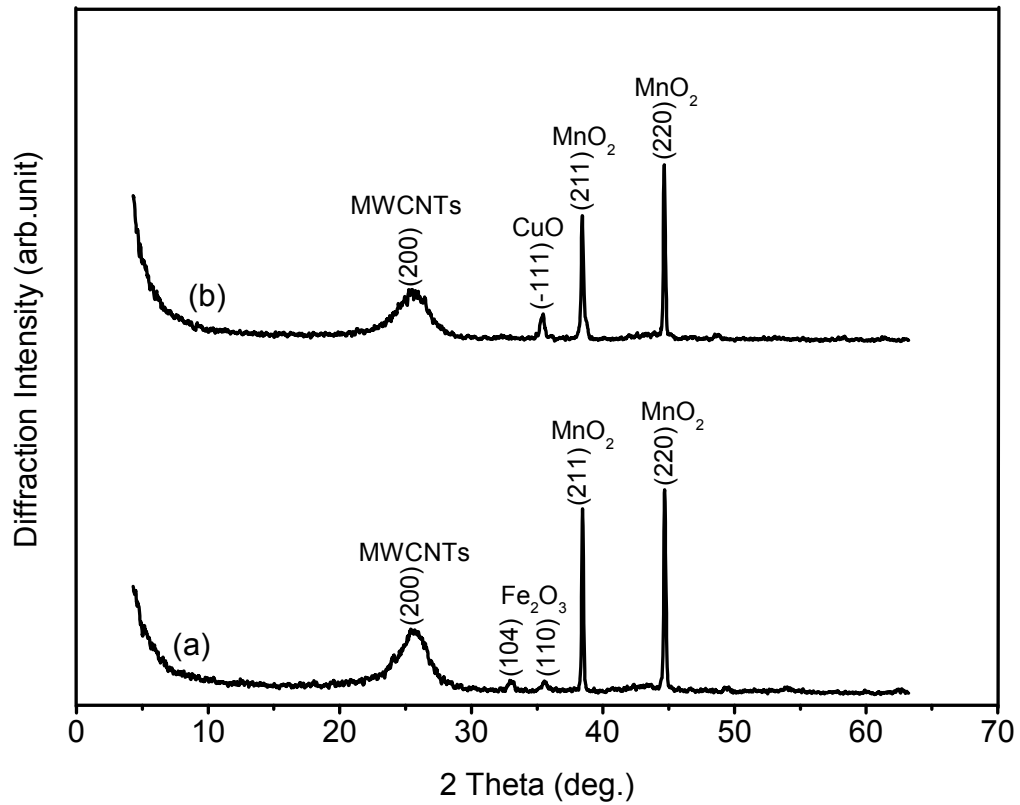
98

Figure 5.17: XRD patterns of (a) 5wt.% (MnO_2/Fe_2O_3)-MWCNTs and (b) 5wt.% (MnO_2/CuO)-MWCNTs.

5.7. Brunauer-Emmett-Teller analysis

Figure 5.18 depicts N_2 adsorption-desorption isotherm of the metal oxides-MWCNTs composites. The isotherms indicate the adsorption hysteresis behaviour in the $P/P_0 \sim$ 0.4 to 0.99. The BET isotherms indicate that all the composites were mainly mesoporous. The BET surface area and porosity of the metal oxides-MWCNTs as shown in table 4.1, indicates that the CuO@300 °C-MWCNTs (558.04 m^2/g) had an increase in the surface area and porosity as compared the acid treated MWCNTs (343.09 m^2/g),. The porosity enhancement is attributed to the coating of CuO nanoparticle (prepared at low temperature) onto the MWCNTs surface, resulting in surface roughness for adsorption of N_2.

The surface area and total pore volume of most nanocomposites are slightly lower than that of acid-treated MWCNTs. This may be due to the blocking effect on some of the tubes by the metal oxides and thus results in a decrease in surface area. Similar findings were reported by Yang *et al.* [10], on the BET surface area of SWCNTs when coated with different percentages of Ni nanoparticles. The surface area decreased from 584.8 m^2/g for the as-prepared SWCNTs to 436.0 m^2/g for the SWCNT + 12wt.%Ni. Zhang *et al.* [11] also reported a decrease in the BET surface area for acid-treated CNTs from 122.41 to 7.41 m^2/g for 80wt.% MnO_x/CNTs.

MWCNTs modified with metal oxides prepared at 500 °C showed lower surface area as compared to metal oxides prepared at 300 °C. This is due to particles agglomerations which led to blockages of MWCNTs inner tubes. Hence a decrease in the N_2 adsorption volume is observed on the adsorption isotherms (Figure 5.18).
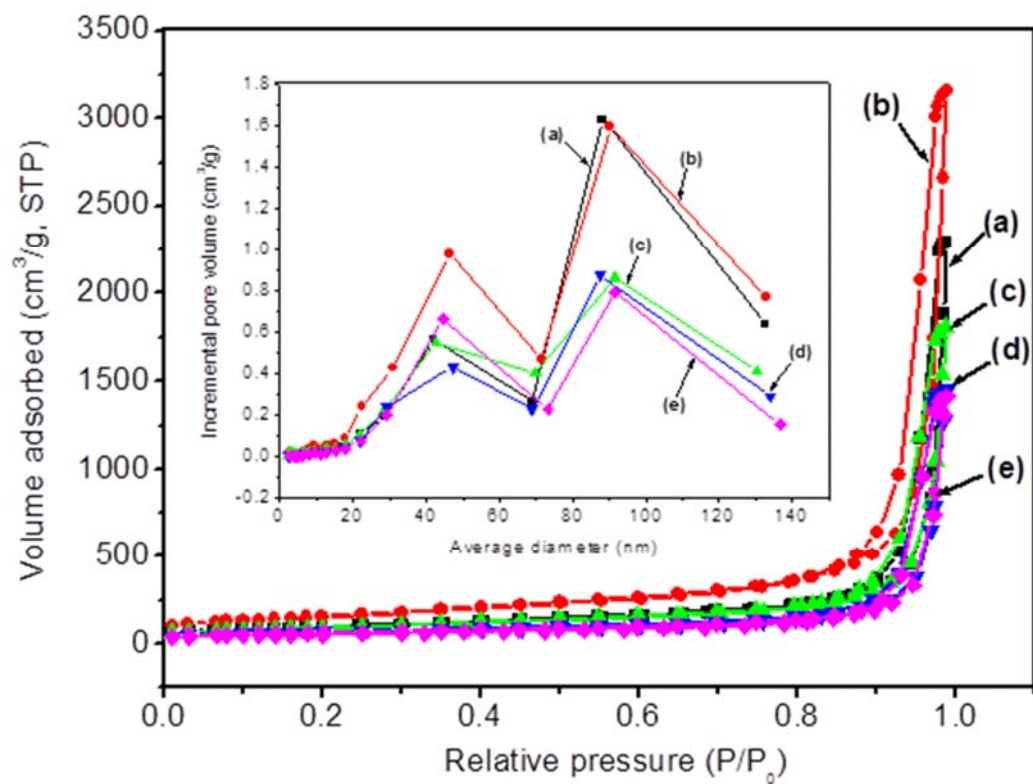
Figure 5.18: N$_2$ adsorption and desorption isotherms and BJH pore size distribution of (a) acid-treated MWCNTs (black line) (b) 5wt.% CuO@300 °C-MWCNTs (red line) (c) 5wt.% Fe$_2$O$_3$@300 °C-MWCNTs (green line) (d) 5wt.% NiO@300 °C-MWCNTs (blue line) and (e) 5wt.% Co$_3$O$_4$@300 °C-MWCNTs (magenta line).

Table 5.1: Surface characteristics of the metal-MWCNTs samples determined from nitrogen physisorption at -195.8 °C

Sample name	BET surface area (m^2g^{-1})	Pore volume (cm^3g^{-1})	Pore sizes (nm)
A-MWCNTs	343.09	2.91	33.96
CuO@300°C-MWCNTs	558.04	4.11	29.48
Fe_2O_3@300°C-MWCNTs	330.27	2.38	28.87
Co_3O_4@300°C-MWCNTs	281.78	2.41	34.20
NiO@300°C-MWCNTs	237.58	1.97	33.11
CuO@500°C-MWCNTs	230.42	1.91	33.06
NiO@500°C-MWCNTs	228.31	2.05	35.83
Co_3O_4@500°C-MWCNTs	212.23	2.03	38.23
Fe_2O_3@500°C-MWCNTs	192.40	1.55	32.27

5.8. Thermogravimetric analysis

The TGA and DTG profiles measured in flowing air for the metal oxides-MWCNTs composites are shown in figure 5.19. All metal oxide-MWCNTs composites exhibited one weight loss step. The TGA (figure 5.19 (a)) curves show that the presence of metal oxides reduces the stability of MWCNTs. The metal oxide-MWCNTs samples demonstrated the residual weights of between 5.8 - 8wt.% metal oxides. These results demonstrate the presence of an intended metal oxides loading of 5wt.% on MWCNTs. DTG curves (figure 5.19 (b)) consists of broad peaks at different positions and the maximum weight losses occurred at 529 °C, 619 °C, 644 °C and 653 °C for the MnO_2/CuO-MWCNTs, CuO@300 °C-MWCNTs, NiO@300 °C-MWCNTs and Fe_2O_3 °C-MWCNTs nanocomposites, respectively. This suggests a clear influence of the attachment of different metal oxides on the thermal stability of metal oxide-MWCNTs nanocomposites. Maximum weight loss for the acid treated MWCNTs occurs at 662 °C. This shows that metal oxides decrease the thermal stability of acid treated MWCNTs.
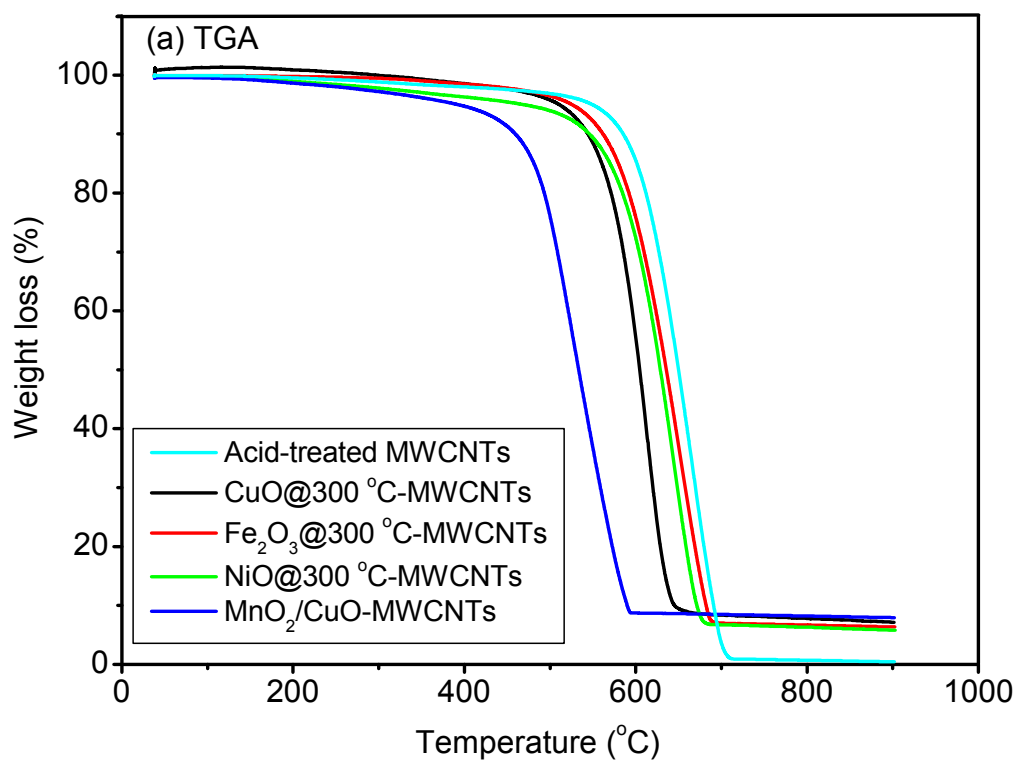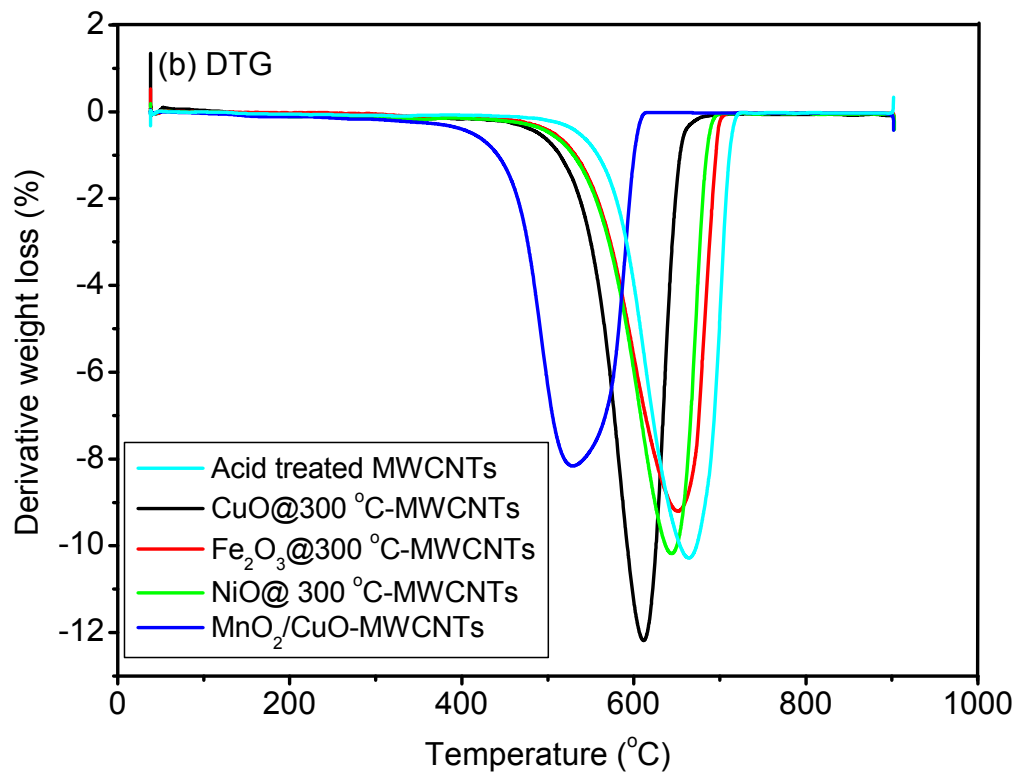
Figure 5.19: The (a) TGA and (b) DTG profiles of metal oxides-MWCNTs nanocomposites, measured in flowing air.

5.9. Electrochemical measurements

5.9.1. Hydrogen storage

5.9.1.1. Cyclic voltammetric characteristics of acid treated MWCNTs and metal oxides doped MWCNTs electrodes

The shape of the CV curve of the acid-treated MWCNTs (treated by $H_2O_2:HNO_3$), (Figure 5.20-5.23) is roughly rectangular in shape, indicating a typical double-layer capacitive behaviour [12, 13]. In this case, the dissolved ions are accumulated at the MWCNT/electrolyte interface by electrostatic attraction forces. The negative current reflects the number of hydrated potassium ions that accumulated during the cathodic polarization of the MWCNTs, while the positive current during anodic polarization corresponds to desorption of hydrated potassium ions [14]. Interestingly several humps are observed on the CV curves (Figure 5.20-5.23) of the metal oxide-MWCNTs nanocomposites, suggesting that, in addition to capacitive behaviour, the faradaic reaction also contributes to the measured discharge capacity [15].

5.9.1.2. Effects of pre-treatment temperature on the current response of 5wt.% CuO-MWCNTs electrodes

For comparison, the CV curves of the acid-treated MWCNTs and 5wt.% CuO-MWCNTs electrodes are shown in figure 5.20. Measurements were studied using a three electrode system in a 6 M solution of KOH as the electrolyte. Runs were carried out in a potential window of -1.4 to 0.2 V at a scan rate of 50 mV/s. Two pairs of redox peaks are observed on the 5wt.% CuO-MWCNTs nanocomposites which can be related to the sequential transitions of Cu^+ to Cu. The curve shows a cathodic peak around -0.58 V (vs Ag/AgCl), upon reversal of the scan direction a corresponding oxidation peak is observed around 0.02 V (vs Ag/AgCl) [2]. The possible mechanism is based on the adsorption of the H^+ ions on the surface of the 5wt.% CuO-MWCNTs composite. The primary reaction involved can be represented as:

$2CuO + 2H^+ + 2e^- \leftrightarrow Cu_2O + H_2O$ **(Equation 5.1)**

The CuO@300 °C-MWCNTs nanocomposite showed a higher BET surface area (558.04 m^2/g) in comparison to 230.42 m^2/g of the CuO@500 °C-MWCNTs nanocomposite. Therefore, the current response of the CuO@300 °C-MWCNTs nanocomposite was expected to be higher, followed by the CuO@400 °C-MWCNTs nanocomposite and lastly the CuO@500 °C-MWCNTs nanocomposite. However the composite with CuO at 300 °C shows the lowest current response. The CV measurements on this electrode were performed about 3 times and the same curve was obtained.
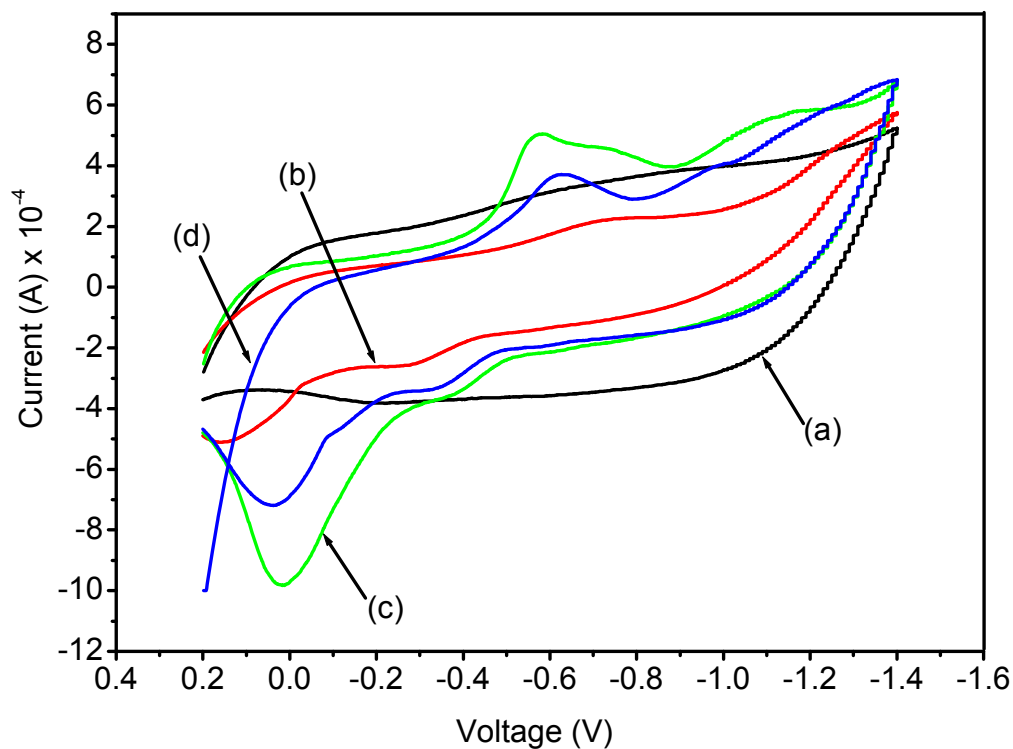

Figure 5.20: CV curves of (a) A-MWCNTs (b) 5wt.% CuO@300 °C-MWCNTs (c) 5wt.% CuO@400 °C-MWCNTs and (d) 5wt.% CuO@500 °C-MWCNTs.

5.9.1.3. Effects of pre-treatment temperature on the current response of 5wt.% Fe_2O_3-MWCNTs electrodes

Figure 5.21 shows the CV curves of the 5wt.% Fe_2O_3-MWCTs nanocomposites. Measurements were studied using a three electrode system in a 6 M solution of KOH as the electrolyte. Runs were carried out in a potential window of -1.4 to 0.2 V at a scan rate of 50 mV/s. Similarly redox peaks are observed which can be related to the transitions of Fe^{3+} to Fe^{2+}. The CV curves show a cathodic peak at around -1.30 V (vs Ag/AgCl) and a corresponding oxidation peak is observed at around -0.62 V (vs Ag/AgCl). The reaction involved can be represented as:

$$Fe_2O_3 + 2H^+ + 2e^- \leftrightarrow 2\,Fe(OH)_2 + 2H_2O \qquad \textbf{(Equation 5.2)}$$

The 5wt.% Fe_2O_3 @300 °C-MWCNTs shows the highest current response as expected. This electrode material showed the highest BET surface area of 330.27 m^2/g and small average crystallite size of 25.8 nm in comparison to 192.40 m^2/g and 63.8 nm of Fe_2O_3 @500 °C-MWCNTs.
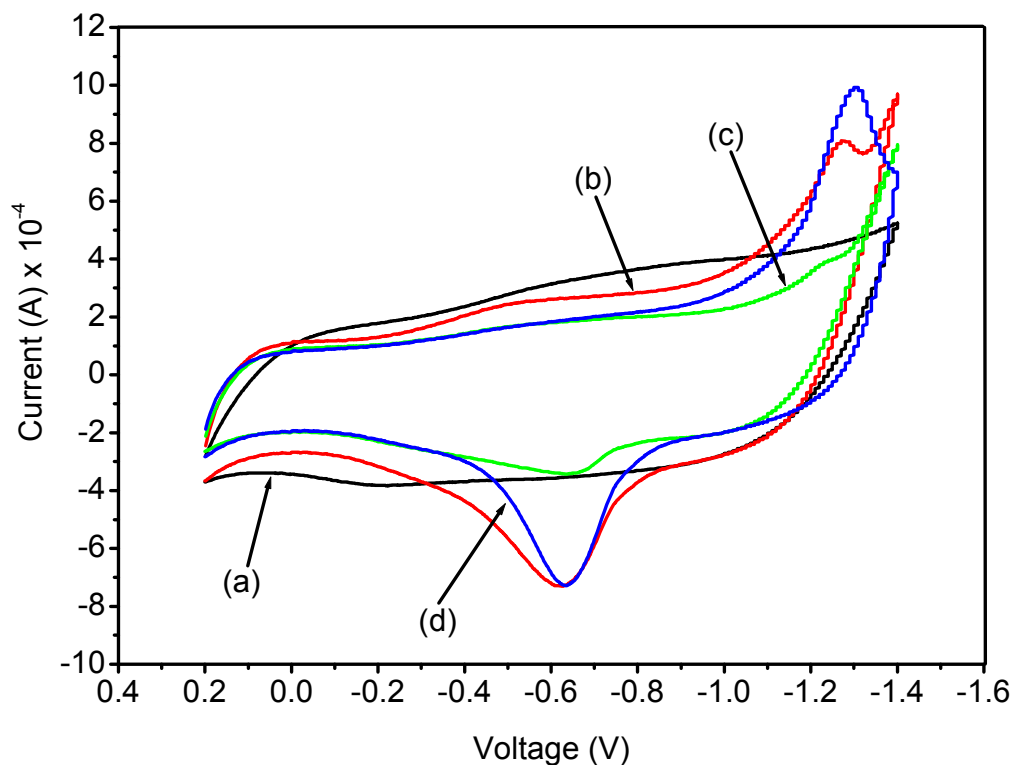
Figure 5.21: CV curves of (a) A-MWCNTs (b) 5wt.% Fe_2O_3@300 °C-MWCNTs (c) 5wt.% Fe_2O_3@400 °C-MWCNTs and (d) 5wt.% Fe_2O_3@500 °C-MWCNTs.

5.9.1.4. Effects of pre-treatment temperature on the current response of 5wt.% NiO-MWCNTs electrodes

The shapes of the CV curves of the 5wt.% NiO-MWCNTs (Figure 5.22) reveal that the adsorption/desorption mechanism is very similar to that of electric double-layer, in which the shape is normally close to an ideal rectangular shape. However, these results are not in agreement with the results that were reported previously [5, 13, 16, 17-19] since the proposed mechanism in NiO-MWCNTs composites is mainly from faradaic redox between NiO particles and KOH electrolyte according to the following electrochemical reaction:

$NiO + OH^- \leftrightarrow NiOOH + e^-$ **(Equation 5.3)**

The main factor contributing toward this behaviour may be the octahedral geometry of the NiO obtained, since in most or all previous papers, the NiO nanoparticles usually have the flake like morphology [5, 6]. Su *et al.* obtained the flake-like morphology of nickel oxide by the direct deposition of NiO onto the surface of CNTs, through refluxing a mixture of nickel nitrate hexahydrate, urea and MWCNTs, followed by calcination at 300 °C. They demonstrated that the flake-like morphology of NiO results in an open and porous structure of the NiO-CNT composites. Such an open hierarchical porous structure of NiO could permit easy access for solvated ions to the electrode/electrolyte interface, which is crucial for surface Faradaic reactions [5, 6]. The observed result suggests that the octahedral structure of NiO does not provide easy access for ions to the electrolyte/electrode interface, hence a decrease in surface area of NiO containing MWCNTs. This results in the dissolved ions being accumulated at the MWCNTs/electrolyte interface.

Comparing the three metal oxides/MWCNTs electrode materials it can be clearly observed that the NiO@300 °C-MWCNTs nanocomposite shows higher current response followed by NiO@400 °C-MWCNTs and lastly NiO@500 °C-MWCNTs. These results are consistent with the BET surface area of the composites which was found to be 237.58 and 228.31 m^2/g for the NiO@300 °C-MWCNTs and NiO@500 °C-MWCNTs, respectively. The calculated crystallite size of NiO@300 °C-MWCNTs nanocomposite is also lower (20.2 nm) in comparison to 24.9 nm of the NiO@500 °C-MWCNTs. Based on the size of NiO treated at 500 °C, the results suggests that the crystallite size influences the current response of the nanocomposites.
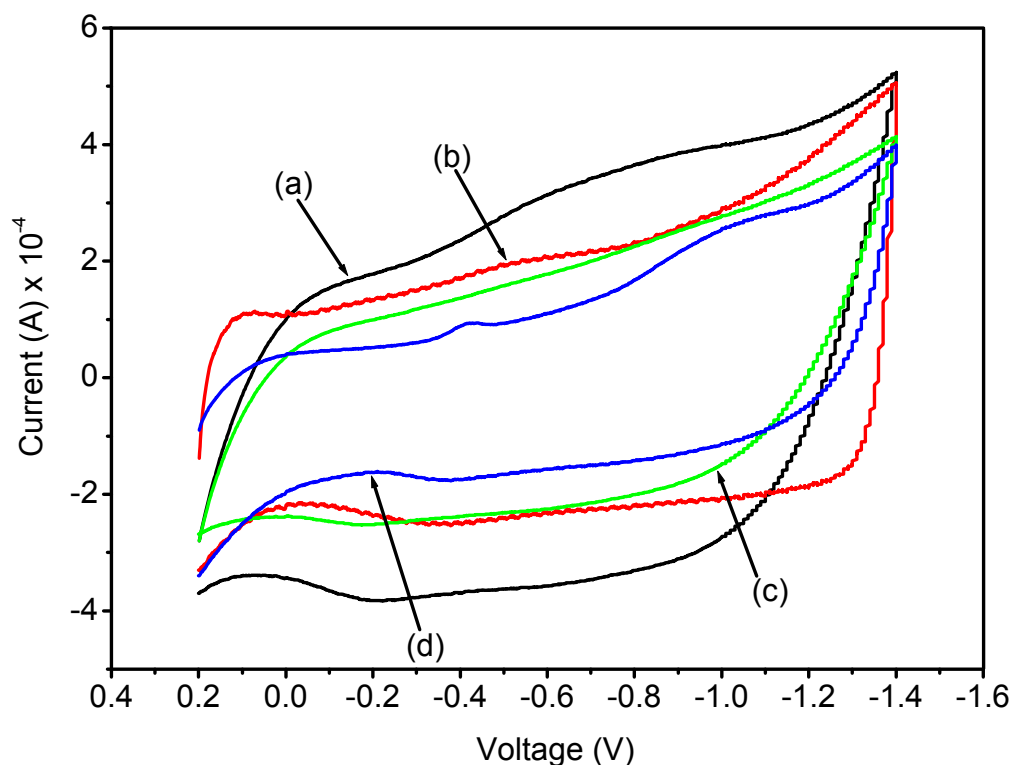
Figure 5.22: CV curves of (a) A-MWCNTs (b) 5wt.% NiO@300 °C-MWCNTs (c) 5wt.% NiO@400 °C-MWCNTs and (d) 5wt.% NiO@500 °C-MWCNTs.

5.9.1.5. Effects of pre-treatment temperature on the current response of the Co_3O_4-MWCNTs electrodes

From the CV curves of the 5wt.% Co_3O_4-MWCNTs shown in figure 5.23, it can be clearly seen that there are two strong distinct pairs or redox peaks during the anodic and cathodic sweeps. Measurements were studied using a three electrode system in a 6 M solution of KOH as the electrolyte. Runs were carried out in a potential window of -1.4 to 0.2 V at a scan rate of 50 mV/s. These redox peaks correspond to conversion between different cobalt oxidation states. The pair of broad redox peaks can be seen at -0.35 V and -0.76 V respectively. The possible mechanism is as follows [13]:

$Co_3O_4 + H_2O + OH^- \leftrightarrow 3CoOOH + e^-$ **(Equation 5.4)**
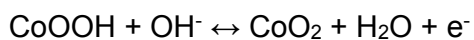
$CoOOH + OH^- \leftrightarrow CoO_2 + H_2O + e^-$ **(Equation 5.5)**

The Co_3O_4@300 °C-MWCNTs nanocomposite show the highest current response followed by Co_3O_4@400 °C-MWCNTs and lastly Co_3O_4@500 °C-MWCNTs. This is in good agreement with the BET surface area and the calculated crystallite sizes. The Co_3O_4@300 °C-MWCNTs showed the highest BET surface area of 281.78 m^2/g and average crystallite of 42.5 nm. The Co_3O_4@500 °C-MWCNTs nanocomposite showed the BET surface area of 212.23 m^2/g and average crystallite size of 59.8 nm, which is an increase of crystallite size with temperature.
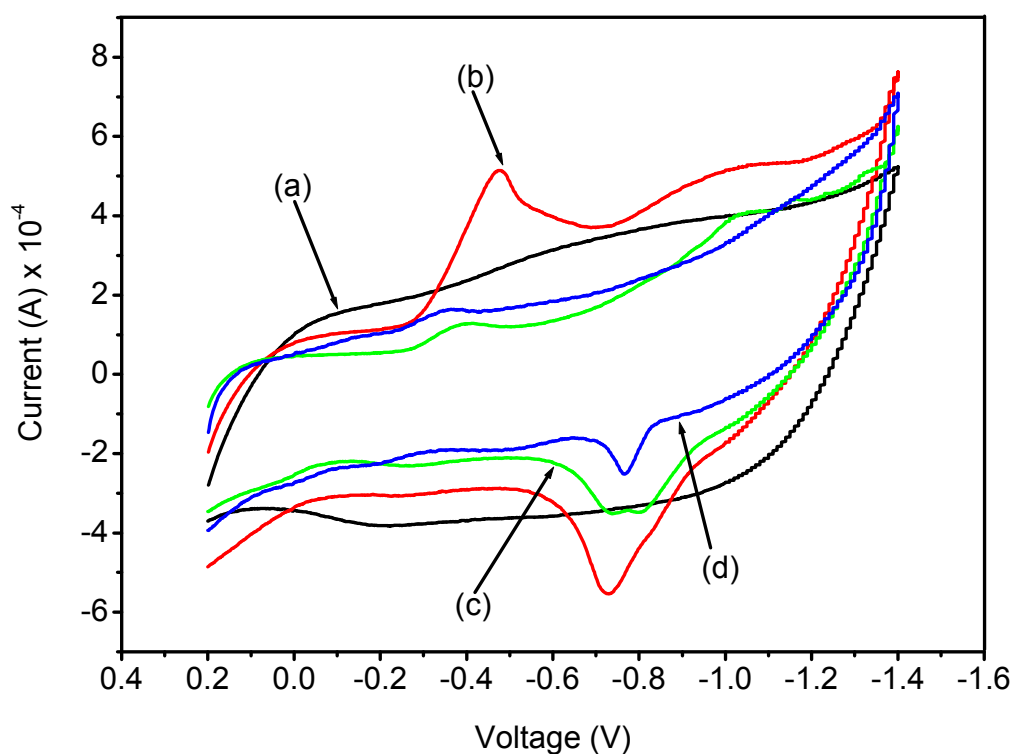

Figure 5.23: CV curves of (a) A-MWCNTs (b) 5wt.% Co_3O_4@300 °C-MWCNTs (c) 5wt.% Co_3O_4@400 °C-MWCNTs and (d) 5wt.% Co_3O_4@500 °C-MWCNTs.

5.9.1.6. Hydrogen discharge capacity characteristics of the electrodes

Figure 5.24 show the discharge capacity curves of the MWCNTs electrodes and the corresponding hydrogen storage capacities calculated from the curves are shown in table 5.2. From the calculated discharge capacities it can be clearly observed that

the 5wt.% CuO-MWCNTs shows higher hydrogen storage capacities as compared to the other electrode materials (See Appendix 2 to 4). The main factors contributing to the high discharge capacity are; (1) higher specific surface area obtained for the CuO-MWCNTs nanocomposites, (2) the nanosheet-like structure of CuO which provide suitable porosity for easy insertion/de-insertion of ions into/from the electrode matrix and lastly small crystallite sizes (19.73 nm at a pre-treatment temperature of 300 °C) obtained for the CuO-MWCNTs which shortens the ion diffusion paths within the active material.
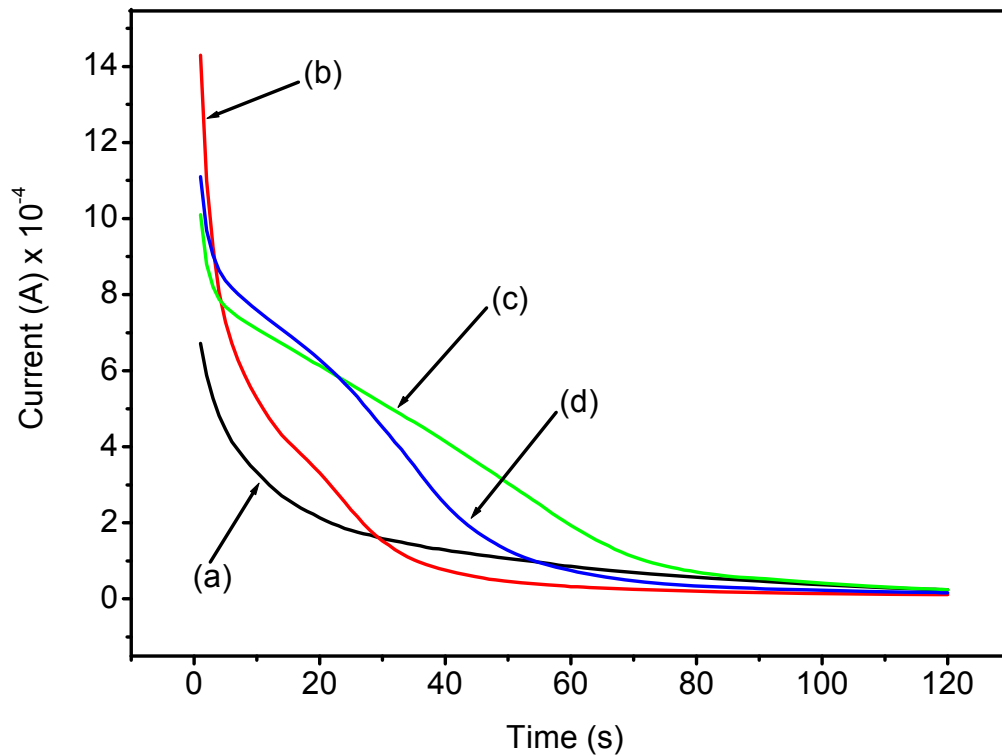

Figure 5.24: Discharge curves of (a) A-MWCNTs (b) 5wt.% CuO@300 °C-MWCNTs (c) 5wt.% CuO@400 °C-MWCNTs and (d) 5wt.% CuO@500 °C-MWCNTs.

Table 5.2: Electrochemical hydrogen storage data for the metal oxides-MWCNTs samples nanocomposites

MWCNTs samples	Discharge capacity (mAh/g)[a]		
CuO	-16.65		
A-MWCNTs	72.63		
5% (MnO$_2$/CuO)-MWCNTs	172.27		
	@300°C	**@400°C**	**@500°C**
5% CuO-MWCNTs	158.84	109.45	120.88
5% Fe$_2$O$_3$-MWCNTs	112.78	95.90	69.71
5% Co$_3$O$_4$-MWCNTs	90.13	63.16	54.39
5% NiO-MWCNTs	89.91	79.25	52.39

[a]All data were repeated three times.

5.9.1.7. Cyclic voltammetric characteristics of CuO, CuO-MWCNTs, MnO$_2$/CuO-MWCNTs electrodes

Since the 5wt.% CuO-MWCNTs electrode showed the highest hydrogen storage capacity as compared to all nanocomposites electrodes. MnO$_2$ was mixed with CuO (MnO$_2$/CuO molar ratio = 1:1) following the method described in chapter 3. The 5wt.% of MnO$_2$/CuO mixture was mixed with the acid-treated MWCNTs (treated by H$_2$O$_2$:HNO$_3$) using the method described in chapter 3. Figure 5.24 show the CV curves of CuO, 5wt.% CuO-MWCNTs and 5wt.% (MnO$_2$/CuO)-MWCNTs electrodes. Measurements were studied using a three electrode system in a 6 M solution of KOH as the electrolyte. Runs were carried out in a potential window of -1.4 to 0.2 V at a scan rate of 50 mV/s. A distorted, featureless CV curve is observed for the CuO electrode (see an insert). The main reason for this behaviour is the lack of electrical

conductivity for the CuO electrode [2]. The MnO$_2$/CuO-MWCNTs showed high current response, as compared to 5wt.% CuO-MWCNTs; with distinct oxidation and reduction peaks at around -0.66 V and 0.03 V, respectively. These results demonstrated that the current response of CuO-MWCNTs nanocomposite can be improved by addition of manganese oxide.
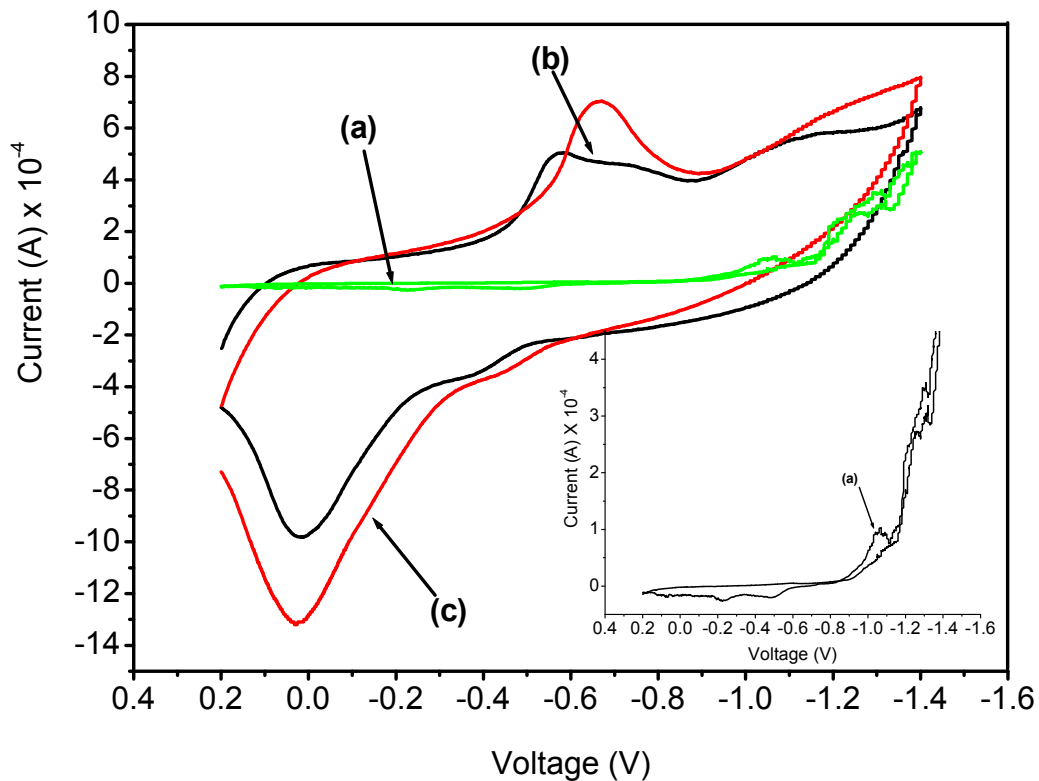

Figure 5.25: CV curves of (a) CuO (b) 5wt.% CuO-MWCNTs (c) 5wt.% (MnO$_2$/CuO)-MWCNTs and an insert of expanded CuO.

5.9.1.8. Concluding remarks on hydrogen storage capacities of metal oxides doped MWCNTs electrodes

The order of discharge capacity values of different nanocomposites is as follows: 5wt.% CuO-MWCNTs > 5wt.% Fe$_2$O$_3$-MWCNTs > 5wt.% Co$_3$O$_4$-MWCNTs > 5wt.% NiO-MWCNTs, at 300 °C pre-treatment of metal oxides. The characteristics of electrochemical reactions are strongly dependent on the shape and dimensionality of the electrode material at the nanoscale level [1]. The possible main factor that

contributed to low discharge capacity for the 5wt.% NiO-MWCNTs electrode is due to the cube-like morphology of the NiO nanoparticles obtained, which is not providing enough facilitation of the ion transport paths.

The discharge capacity decreased with an increase in pre-treatment temperature of the metal oxides except for 5wt.% CuO-MWCNTs electrode. The relation between the discharge capacity (DC) values and the calcination temperature for the electrodes is as follows: $DC_{300\ ^oC} > DC_{400\ ^oC} > DC_{500\ ^oC}$. Smaller average crystallite sizes, higher BET surface area and porosity enhancement are the major factors contributing to the high discharge capacity at lower metal oxide pre-treatment temperature (300 ^{o}C). Pure CuO nanoparticles (Appendix 5) showed -16 mAh/g of discharge capacity, indicating that the pure CuO nanoparticles have no hydrogen oxidation in the discharge process.

The highest discharge capacity of 172 mAh/g corresponding to an electrochemical hydrogen storage capacity of 0.64 wt% was obtained using the 5wt.% (MnO_2/CuO)-MWCNTs electrode. Particle size and morphology of metal oxide nanoparticles plays an important role in the electrochemical performance of metal oxides-MWCNTs nanocomposites. High crystallite sizes (19.73-63.80 nm) of metal oxides, might be the major factors that contributed to low hydrogen storage capacities; as compared to the values reported in the literature [20, 21].

5.9.2. Supercapacitor studies

5.9.2.1. Cyclic voltammetric characteristics of A-MWCNTs, 5wt.% Fe_2O_3@300 ^{o}C-MWCNTs, 5wt.% Fe_2O_3@400 ^{o}C-MWCNTs and 5wt.% Fe_2O_3@500 ^{o}C-MWCNTs

The prepared nanocomposites were subjected to typical cyclic voltammetric tests in a 1 M Na_2SO_4 solution. The measurements were carried out in a 1 M Na_2SO_4 aqueous electrolyte at room temperature. CV tests were carried out using a potential window ranging between -0.1 and 0.9 V at a scan rate of 50 mV/s It is well known that cyclic voltammetric measurements are helpful in understanding the microscopic electrochemical surface reactions at the electrode of the supercapacitor during the

charging and discharging process [22]. The studies was undertaken at a potential ranging between -0.1 to 0.9 V (versus Ag/AgCl) at a scan rate of 50 mV / s.

Figure 5.27 show the CV curves of the acid treated MWCNTs (treated by H_2O_2:HNO_3) and Fe_2O_3 (treated at different temperature) on-MWCNTs. These CVs are relatively rectangular in shape and exhibit near mirror image current response on voltage reversal indicating a reversible reaction and ideal capacitive behaviour for all the nanocomposites [7]. It can be clearly seen that the CV curves do not exhibit those clear peaks observed in the hydrogen storage case, indicating the absence or little redox activity in this case [23]. The main reason for the lack of redox activity is the change of the applied potential since varying the applied potential changes the oxidising/reducing ability of any electrode [24]. For example, more negative potentials increase the reducing ability of the electrode and vice versa.

The 5wt.% Fe_2O_3-MWCNTs (Figure 5.27) nanocomposites show higher enclosed area as compared to all the other electrode materials (See Appendix 6 to 8). This consequently mean higher specific capacitance, which implies that more number of charges are involved in the 5wt.% Fe_2O_3-MWCNTs nanocomposites in relation all the other nanocomposites. The major contributing factor to high specific capacitance is the tubular morphology of Fe_2O_3, which was reported by Xie *et al.* [3]. The highest specific capacitance was obtained for the nanocomposite with metal oxides prepared at high temperatures (400 ºC and 500 ºC). The Fe_2O_3@400 ºC-MWCNTs nanocomposite showed the highest specific capacitance, followed by the Fe_2O_3@500 ºC-MWCNTs nanocomposite. The Fe_2O_3@300 ºC-MWCNTs nanocomposite showed the lowest specific capacitance.

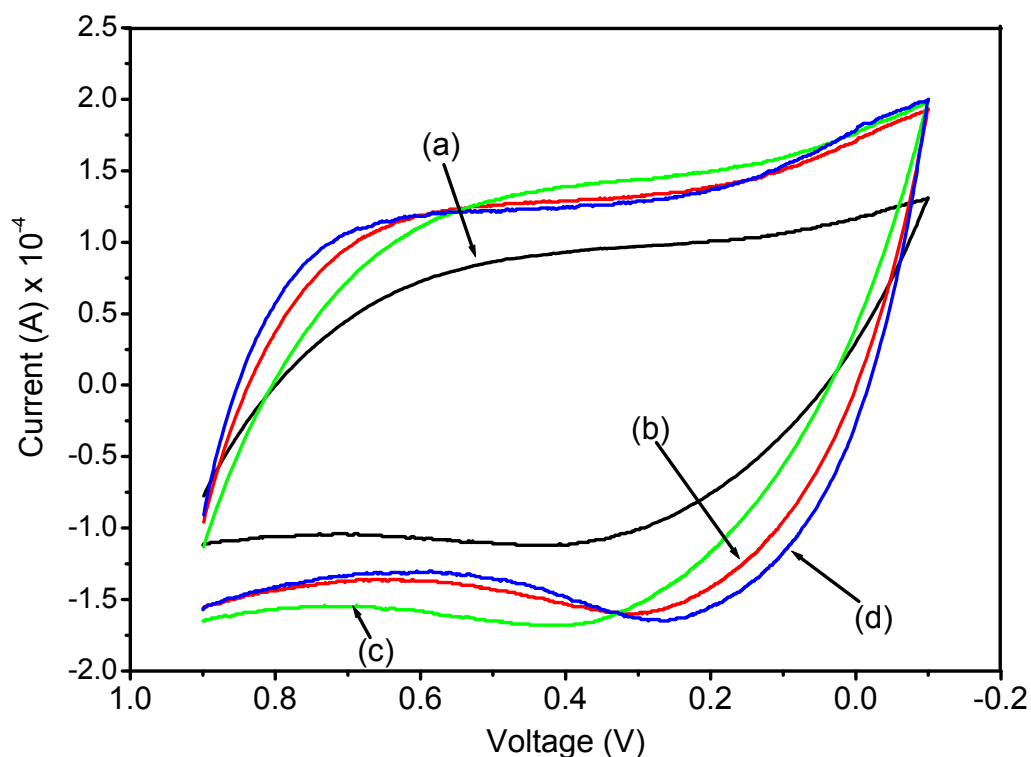**Figure 5.26:** CV curves of (a) A-MWCNTs (b) 5wt.% Fe_2O_3@300 °C-MWCNTs (c) 5wt.% Fe_2O_3@400 °C-MWCNTs and (d) 5wt.% Fe_2O_3@500 °C-MWCNTs.

5.9.2.2. Cyclic voltammetric characteristics of Fe_2O_3, 5wt.% Fe_2O_3-MWCNTs and 5wt.% (MnO_2/Fe_2O_3)-MWCNTs electrodes

When a thick- and compact metal oxide film is used alone for electrode fabrication, the charge-transfer-reaction kinetics is limited tremendously due to its poor electronic conductivity and difficulty in the penetration of electrolyte [25]; this is evidently shown by the CV curve of Fe_2O_3 electrode shown on figure 5.28. Measurements were carried out in a 1 M Na_2SO_4 aqueous electrolyte at room temperature. CV tests were carried out using a potential window ranging between -0.1 and 0.9 V at a scan rate of 50 mV/s. However, the incorporation of Fe_2O_3 on MWCNTs, gave high capacitance. Surprisingly, the capacitance decreased when MnO_2 was added into the Fe_2O_3-MWCNTs composites. The reason behind these is still unknown. The specific

capacitance values for the MWCNTs samples calculated from the CV curves are presented in table 5.3.
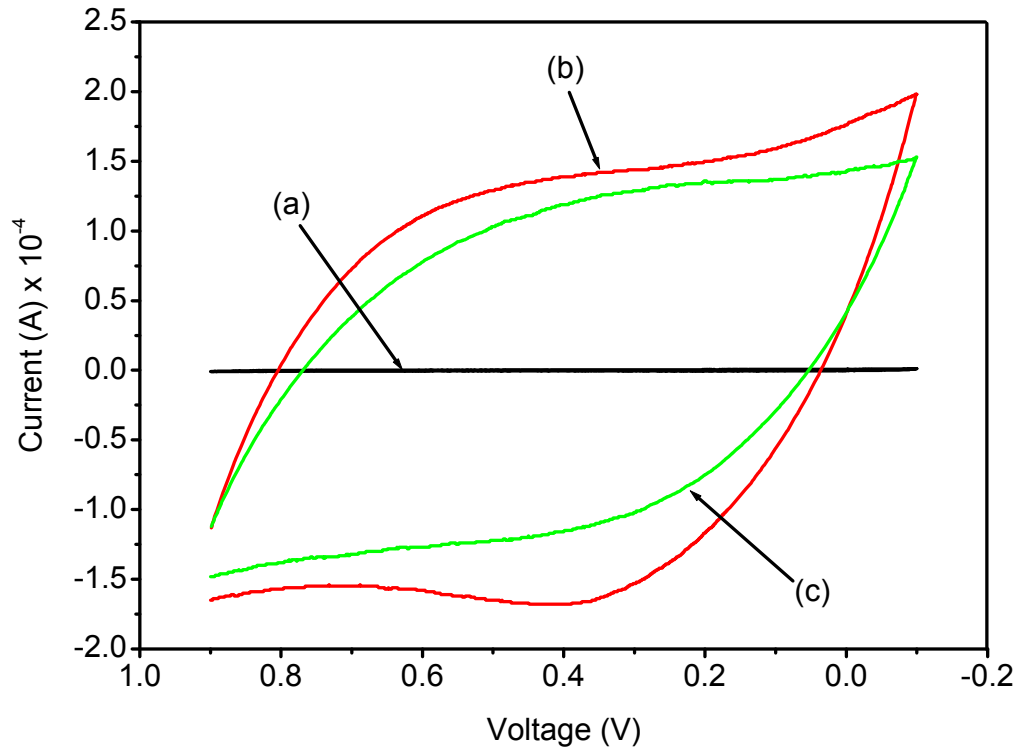

Figure 5.27: CV curves of the (a) Fe_2O_3 (b) 5wt.% Fe_2O_3-MWCNTs   (d) 5wt.% (MnO_2/Fe_2O_3)-MWCNTs.

Table 5.3: Specific capacitance of the metal oxides-MWCNTs nanocomposites

MWCNTs samples	Specific capacitance (F/g)		
Fe_2O_3	0.00		
A-MWCNTs	6.39		
5% (MnO_2/Fe_2O_3)-MWCNTs	8.10		
	@300 °C	@400 °C	@500 °C
5% Fe_2O_3-MWCNTs	9.26	9.70	9.46
5% CuO-MWCNTs	7.97	7.29	8.04
5% NiO-MWCNTs	7.77	8.30	8.87
5% Co_3O_4-MWCNTs	5.20	8.66	8.21

5.9.2.3 Concluding remarks on supercapacitance characteristics of metal oxides doped MWCNTs electrodes

It is well known that the larger enclosed area of the CV curves, the greater the specific capacitance of the nanocomposites [26]. A slight increase in the area of the curves was observed when the different metal oxides are introduced into the acid-treated MWCNTs (Figure 5.27 and Appendix 6-8). The increase in specific capacitance can be attributed to the unique coaxial nanostructure of the metal oxides. During the charge storage process the ultrathin metal oxide nanocoatings provide short ion/electron transport pathways while the porous interwoven network structure enables fast electrolyte penetration and facilitate continuous ion/electron transport throughout the electrode [27]. In other words the synergetic interaction between the metal oxides and MWCNTs results in improved electronic conductivity and ionic accessibility in the samples.

A slight increase in the specific capacitance for all the metal oxide-MWCNTs composites, as compared to the acid treated MWCNTs is possibly due to the small amount of the metal oxides inside the composite. No particular pattern is observed in terms of capacitance in relation to the calcination temperature for the metal oxides. The temperature dependence varies with each material but the values are almost similar.

5.10. References

[1] Dubal D.P, Gund G.S, Holze R and Lokhande C.D, Mild chemical strategy to grow micro-roses and micro-woolen like arranged CuO nanosheets for high performance supercapacitors, Journal of Power Sources 242 (2013) 687-698

[2] Pendashteh A, Mousavia M.F and Rahmanifar M.S, Fabrication of anchored copper oxide nanoparticles on graphene oxide nanosheets via an electrostatic coprecipitation and its application as supercapacitor, Electrochimica Acta 88 (2013) 347-357

[3] Xie K, Li J, Lai Y, Lu W, Zhang Z, Liu Y, Zhou L and Huang H, Highly ordered iron oxide nanotube arrays as electrodes for electrochemical energy storage, Electrochemistry Communications 13 (2011) 657-660

[4] Wang L, Zhang L.-C, Cheng J.-X, Ding C.-X and Chen C.-H, Watermelon used as a novel carbon source to improve the rate performance of iron oxide electrodes for lithium ion batteries, Electrochimica 102 (2013) 306-311

[5] Su A.D, Zhang X, Rinaldi A, Nguyen S.T, Liu H, Lei Z and Lu L, Hierarchical porous nickel-carbon nanotubes as advanced pseudocapacitor materials for supercapacitors, Chemical Physics Letters 561-562 (2013) 68-73

[6] Inandar A.I, Kim Y, Pawar S.M, Kim J.H, Im H and Kim H, Chemically grown, porous, nickel oxide thin-film for electrochemical supercapacitors, Journal of Power Sources 196 (2011) 2393-2397

[7] Xu C, Li B, Du H, Kang F and Zeng Y, Electrochemical properties of nanosized hydrous manganese dioxide synthesized by self-reacting microemulsion method, Journal of Power Sources 180 (2008) 664-670

[8] Deng J, Kang L, Bai G, Li Y, Li P, Liu X, Yang Y, Gao F and Liang W, Solution combustion synthesis of cobalt oxides (Co_3O_4 and Co_3O_4/CoO) nanoparticles as supercapacitor electrode materials, Electrochimica Acta 132 (2014) 127-135

[9] Abbas S.M, Hussain S.T, Ali S and Ahmad N, Synthesis of carbon nanotubes anchored with mesoporous Co_3O_4 nanoparticles as anode material for lithium-ion batteries, Electrochimica Acta 105 (2013) 481-488

[10] Yang C.-C, Li Y.J and Chen W, Electrochemical hydrogen storage behaviour of single-walled carbon nanotubes (SWCNTs) coated with Ni nanoparticles, International Journal of Hydrogen Energy 35 (2010) 2336-2343

[11] Zhang S, Chuang P, Ng K.C and Chen G.Z, Nanocomposites of manganese oxides and carbon nanotubes for aqueous supercapacitor stacks, Electrochimica Acta 55 (2010) 7447-7453

[12] Shen J, Liu A, Tu Y, Wang H, Jiang R, Ouyang J and Chen Y, Asymmetric deposition of manganese oxide in single walled carbon nanotube films as electrodes for flexible high frequency response electrochemical capacitors, Electrochimica Acta 78 (2012) 122-132

[13] Fan Z, Chen J, Cui K, Sun F, Xu Y and Kuang Y, Preparation and capacitive properties of cobalt–nickel oxides/carbon nanotube composites, Electrochimica Acta 52 (2007) 2959-2965

[14] Shan C, Yang H , Song J, Han D, Ivaska A and Niu L, Direct electrochemistry of glucose oxidase and biosensing for glucose based on graphene, Analytical Chemistry 81 (2009) 2378-2382

[15] Hsieh C, Chou Y and Lin J, Fabrication and electrochemical activity of Ni-attached carbon nanotube electrodes for hydrogen storage in alkali electrolyte, International Journal of Hydrogen Energy 32 (2007) 3457-3464

[16] Nam K, Kima K, Lee E, Yoon W and Yang X, Pseudocapacitive properties of electrochemically prepared nickel oxides on 3-dimensional carbon nanotube film substrates, Journal of Power Sources 182 (2008) 642-652

[17] Zhang L.L, Xiong Z and Zhao X.S, A composite electrode consisting of nickel hydroxide, carbon nanotubes, and reduced graphene oxide with an ultrahigh electrocapacitance, Journal of Power Sources 222 (2013) 326-332

[18] Zhu X, Dai H, Hu J, Ding L and Jiang L, Reduced graphene oxide–nickel oxide composite as high performance electrode materials for supercapacitors, Journal of Power Sources 203 (2012) 243-249

[19] Wang H, Yi H, Chen X and Wang X, Facile synthesis of a nano-structured nickel oxide electrode with outstanding pseudocapacitive properties, Electrochimica Acta 105 (2013) 353-361

[20] Gao P, Chen Y, Lv H, Li X, Wang Y and Zhang Q, Synthesis of CuO nanoribbon arrays with noticeable electrochemical hydrogen storage ability by a simple precursor dehydration route at lower temperature, International Journal of Hydrogen Energy 34 (2009) 3065-3069

[21] Liu E, Wang J, Li J, Shi C, He C and Du X, Enhanced electrochemical hydrogen storage capacity of multi-walled carbon nanotubes by TiO_2 decoration, International Journal of Hydrogen Energy 36 (2011) 6739-6743

[22] Xie L, Wu J, Chen C, Zhang C, Wan L, Wang J, Kong Q, Lv C, Li K and Sun G, A novel asymmetric supercapacitor with an activated carbon cathode and a reduced graphene oxide cobalt oxide nanocomposite anode ,Journal of Power Sources 242 (2013) 148-156

[23] Wu M.Q, Snook G.A, Chen G.Z and Fray D.J, Redox deposition of manganese oxide on graphite for supercapacitors, Electrochemistry Communication 6 (2004) 499-504

[24] Instruction manual for bas epsilon for electrochemistry, version 1.60.70 (2000-2004) bioanalytical systems

[25] Lang J, Yan X and Xue Q, Facile preparation and electrochemical characterisation of cobalt oxide/multi-walled carbon nanotube composites for supercapacitors, Journal of Power Sources 196 (2011) 7841-7846

[26] Zhang Y, Li G, Lv Y, Wang L and Zhang A, Electrochemical investigation of MnO_2 electrode material for supercapacitors, International Journal of Hydrogen Energy 36 (2011) 11760-11766

[27] Wang J, Yang Y, Huang Z and Kang F, Synthesis and electrochemical performance of MnO_2/CNTs-embedded carbon nanofibers nanocomposites for supercapacitors, Electrochimica Acta 75 (2012) 213-219

[28] Yan J, Fan Z, Wei T, Cheng J, Shao B, Wang K, Song L and Zhang M, Carbon nanotubes/MnO_2 composites synthesised by microwave-assisted method for supercapacitors with high power and energy densities, Journal of Power Sources 194 (2009)1202-1207

[29] Lehtinen E.J.K and Zachariah M.R, Energy accumulation in nanoparticle collision and coalescence processes, Aerosol science 33 (2002) 357-368

CHAPTER 6

GENERAL CONCLUSION

Treatment of MWCNTs with different acids/oxidiser results in the formation of different functional groups on the surface of MWCNTs as confirmed by FTIR spectroscopy. Amount of surface groups depends on the type of acid/oxidiser, with the amount increasing when the MWCNTs are treated by a mixture of the acids. All the acid-treated MWCNTs samples show better sedimentation stability in distilled water than the raw MWCNTs, which is due the interaction between solvent molecules and the surface groups produced after acid treatments. TEM and XRD results show that treatment with mild acids removes bamboo carbon structures inside the hollow nanotube and the walls remain intact, with formation of thin MWCNTs walls.

Treatment of MWCNTs with strong acid mixtures (HNO_3:H_2SO_4) results in the formation of carbon structures inside the tubes. This resulted in a decrease in the surface area, hydrogen storage capacity and capacitance of the materials. The structural stability of the acids/oxidiser treated MWCNTs, as shown by TGA was as follows: HNO_3:H_2SO_4 < H_2O_2:HNO_3 < H_2O_2: H_2SO_4. The electrochemical studies demonstrated that under the same testing conditions, the MWCNTs treated by H_2O_2:HNO_3 (1:3) had the highest hydrogen storage capacity as compared with the other treated MWCNTs. The highest discharge capacity obtained is 72.63 mAh/g (MWCNTs treated by H_2O_2:HNO_3), which is higher by a factor of 8.82 as compared with the raw MWCNTs (8.23 mAh/g). The specific capacitance increased from 4.9 F/g (raw MWCNTs) to 8.9 F/g (MWCNTs treated by H_2O_2:HNO_3), an increase by a factor of 1.8. Thus, the modification of the MWCNTs with acids/oxidiser improves their surface properties, which leads to an increased electrochemical hydrogen storage capacity and capacitance.

A successful incorporation of metal oxides (CuO, Fe_2O_3, NiO, and Co_3O_4) into the inner/surface structure of acid-MWCNTs was confirmed by XRD, SEM and TEM

results. The electrochemical hydrogen storage and capacitance of MWCNTs was improved by the presence of metal oxides. The metal oxides nanoparticles acted as redox sites for hydrogen storage, thus leading to a better electrochemical hydrogen storage capacity. The hydrogen storage capacity decreased with an increase in pre-treatment temperature of metal oxides, however the capacitance values varied. The structural stability of metal oxides doped MWCNTs, as shown by TGA was as follows: CuO@300 ^{o}C-MWCNTs < NiO@300 ^{o}C-MWCNTs < Fe_2O_3@300 ^{o}C-MWCNTs.

The hydrogen storage capacities were crystallite size and surface area dependent, with smaller crystallite size related to higher hydrogen storage. The 5wt.% CuO@300 ^{o}C-MWCNTs electrodes gave the highest discharge capacity of 159 mAh/g (which is related to 0.59 wt.% hydrogen storage). This value increased to 172 mAh/g, when MnO_2 was added. The 5wt.% Fe_2O_3@400 ^{o}C-MWCNTs electrodes gave the highest specific capacitance of 9.70 F/g as compared to all the other electrode materials. However, the addition of MnO_2 decreased the above stated capacitance value.

FUTURE WORK AND RECOMMENDATIONS

The study demonstrated that treatment of MWCNTs with mixtures of acids has effects on the structural properties of MWCNTs which results in the decrease or increase of hydrogen and energy storage capacities of MWCNTs. The study has also shown that metal oxides (CuO, MnO_2, Fe_2O_3) with an average crystallite size of less than 20 nm have the potential to enhance electrochemical performance of MWCNTs. Future studies will include the following:

- Further characterisation of MWCNTs treated by mixtures of acids by Raman spectra and XPS to have a clear understanding of the factors affecting the electrochemical performance of MWCNTs towards hydrogen and energy storage.
- SEM analysis of MWCNTs after different life cycle to study morphological changes associated with charging and discharging.
- Synthesize metal oxides with average particle sizes of less than 15 nm.
- Synthesize NiO with the flake like morphology using the method described in chapter 5, section 5.4.

APPENDICES

1. **The discharge capacity and hydrogen weight percentage were calculated as follows:**

MnO_2/CuO-MWCNTs nanocomposite,

$$I = I_f - I_i = 0.07mA - 1.62mA = -1.55mA$$

$$t = 120.0s \approx 3.33 \times 10^{-2} h$$

$$m = 0.3mg = 3.0 \times 10^{-4} g$$

$$DC = \left(\frac{(3.33 \times 10^{-2} h)(1.55mA)}{3.0 \times 10^{-4} g} \right) = 172mAh/g$$

$$wt.\% = \left(\frac{(172mAh/g)(2.02wt.\%)}{540mAh/g} \right) = 0.64wt.\%$$

2. **The specific capacitance was calculated as follows:**

Fe_2O_3@400 °C-MWCNTs nanocomposite,

$$C_s = \left(\frac{\int_{V_2}^{V_1} I(V)dV}{(V_1 - V_2)vm} \right)$$

$$v = 50mVs^{-1}$$

$$m = 0.3mg = 3.0 \times 10^{-4} g$$

$$I = 0.19mA - (-0.17mA) = 0.36mA = 3.64 \times 10^{-4} A$$

$$C_s = \left(\frac{((3.64 \times 10^{-4} A/2)(900mV)^2) - ((3.64 \times 10^{-4} A/2)(-100mV)^2)}{(1000mV)(50mVs^{-1})(3.0 \times 10^{-4} g)} \right)$$
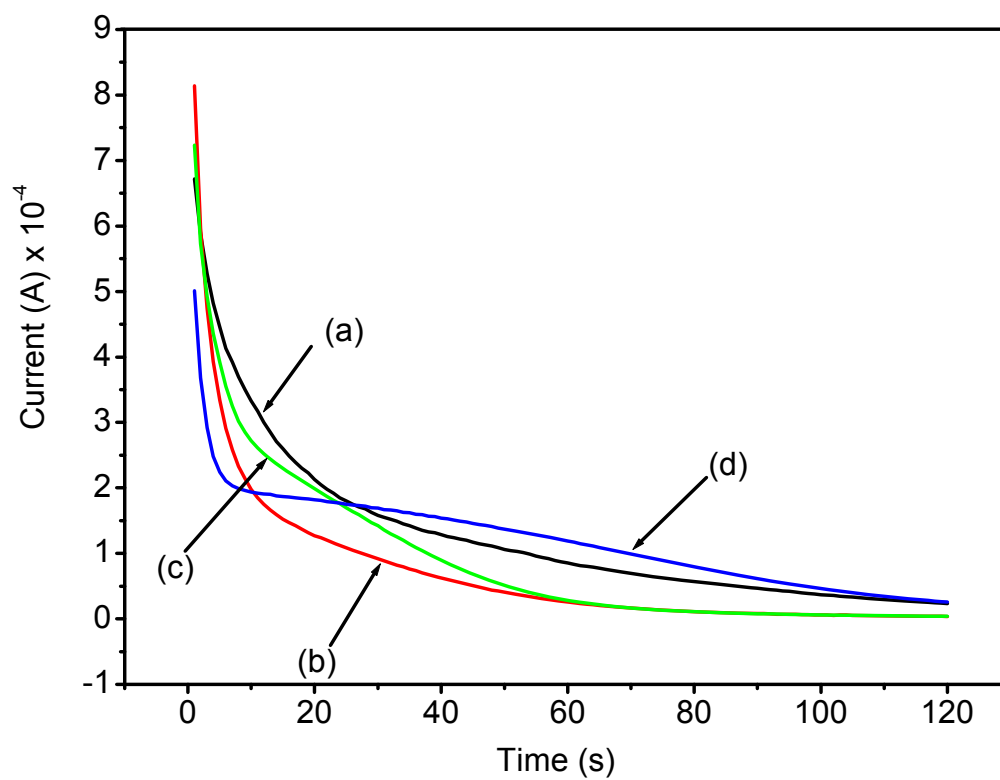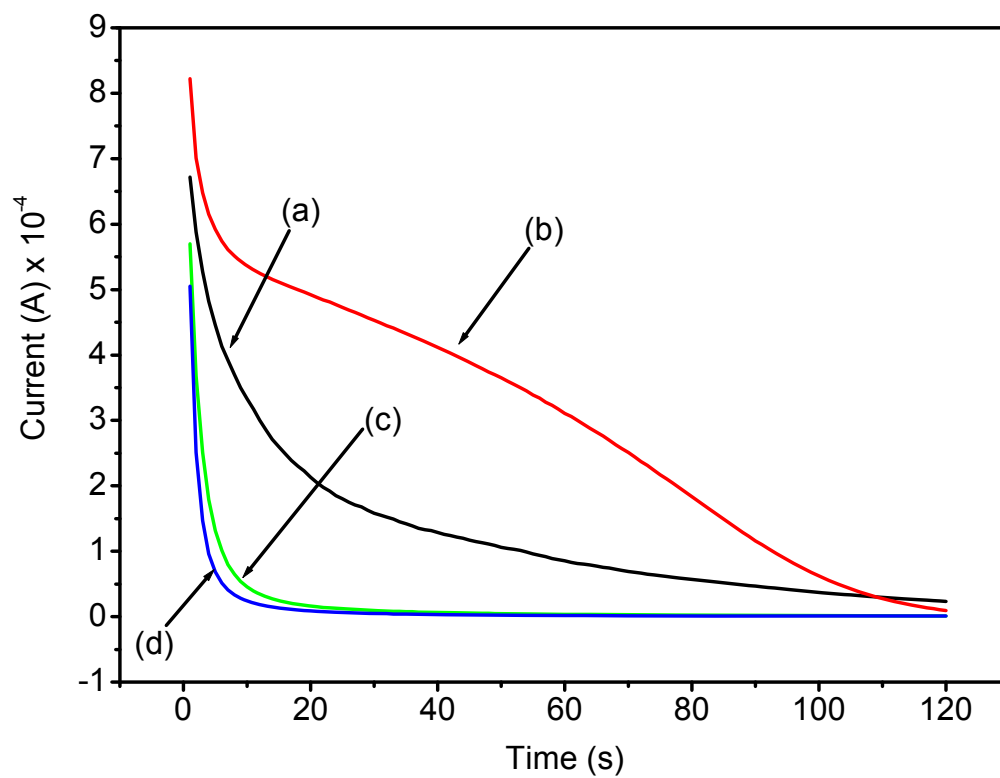
$$C_s = 9.7F/g$$
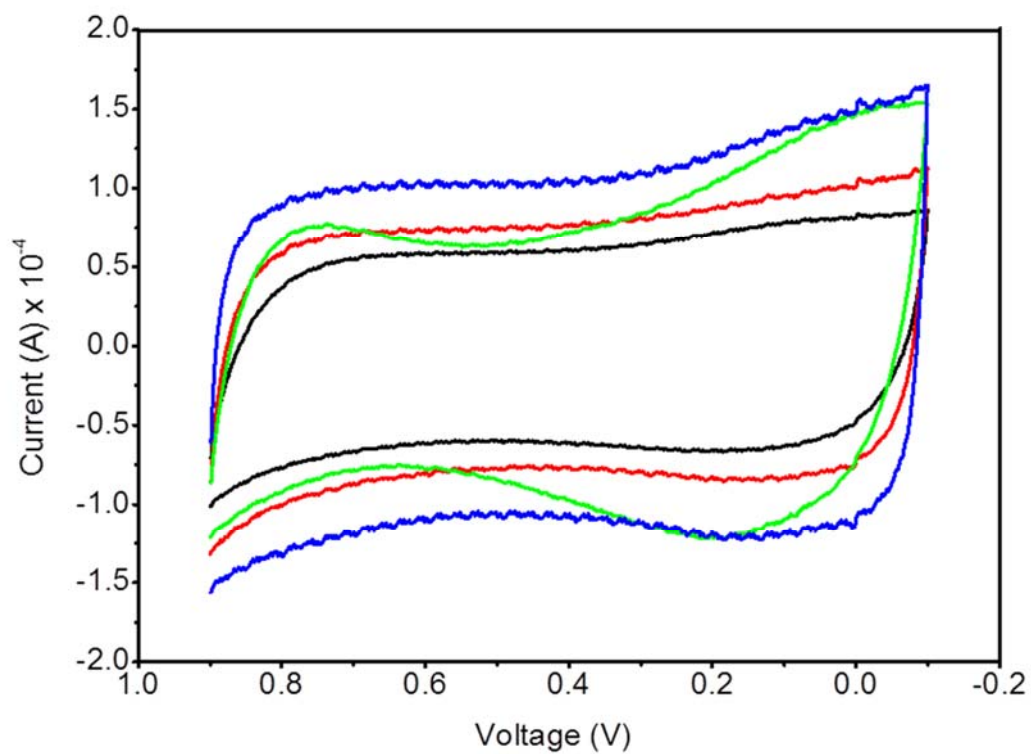
Appendix 1: CV curves of the (a) raw MWCNTs (black line), MWCNTs treated by (b) H_2SO_4 (red line) (c) HNO_3 (green line) and (d) H_2O_2 (blue line).
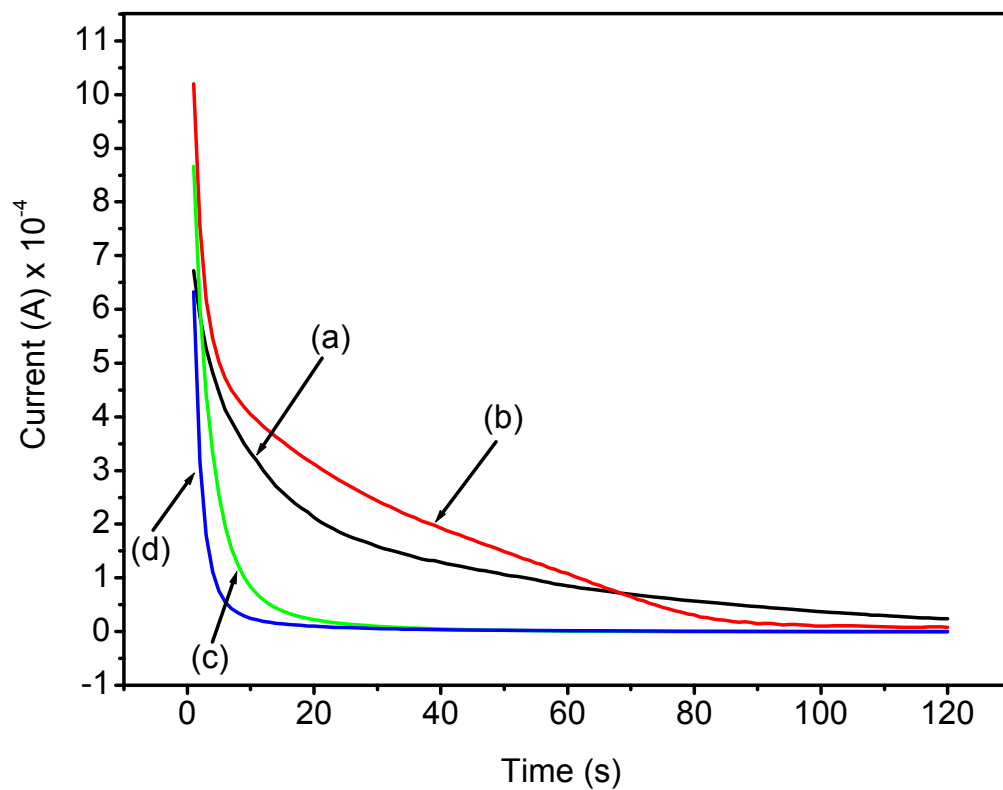
Appendix 2: Discharge curves of (a) A-MWCNTs (b) 5wt.% Fe_2O_3@300 °C-MWCNTs (c) 5wt.% Fe_2O_3@400 °C-MWCNTs and (d) 5wt.% Fe_2O_3@500 °C-MWCNTs.
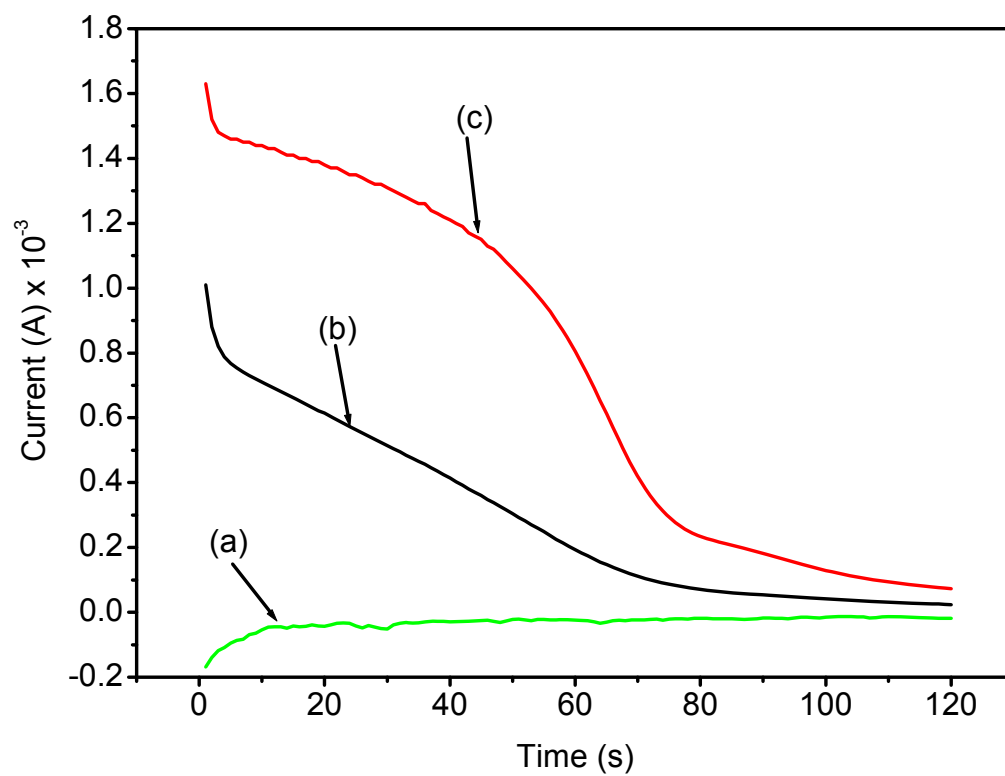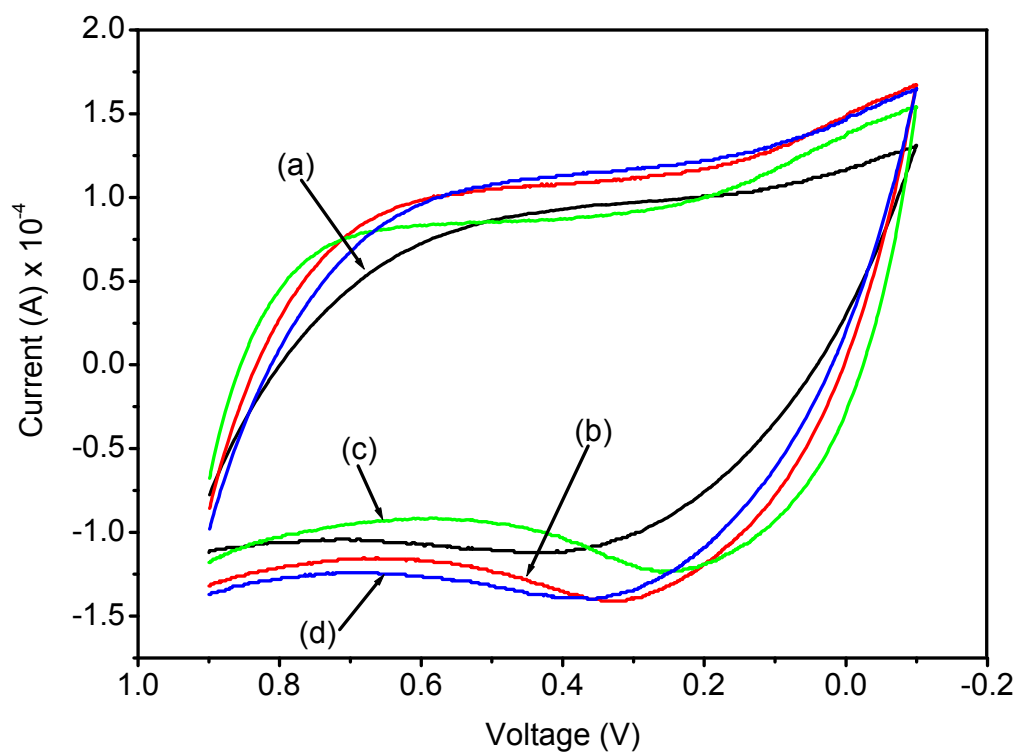
Appendix 3: Discharge curves of (a) A-MWCNTs (b) 5wt.% NiO@300 °C-MWCNTs (c) 5wt.% NiO@400 °C-MWCNTs and (d) 5wt.% NiO@500 °C-MWCNTs.
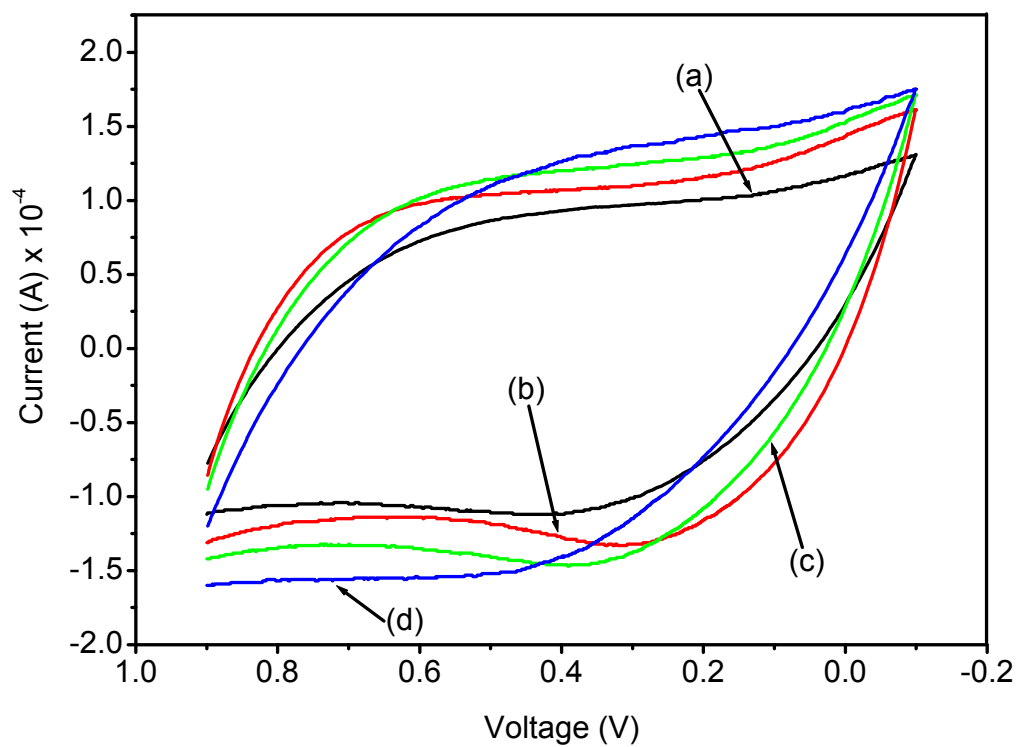
Appendix 4: Discharge curves of (a) A-MWCNTs (b) 5wt.% Co_3O_4@300 ^oC-MWCNTs (c) 5wt.% Co_3O_4@400 ^oC-MWCNTs and (d) 5wt.% Co_3O_4@500 ^oC-MWCNTs.
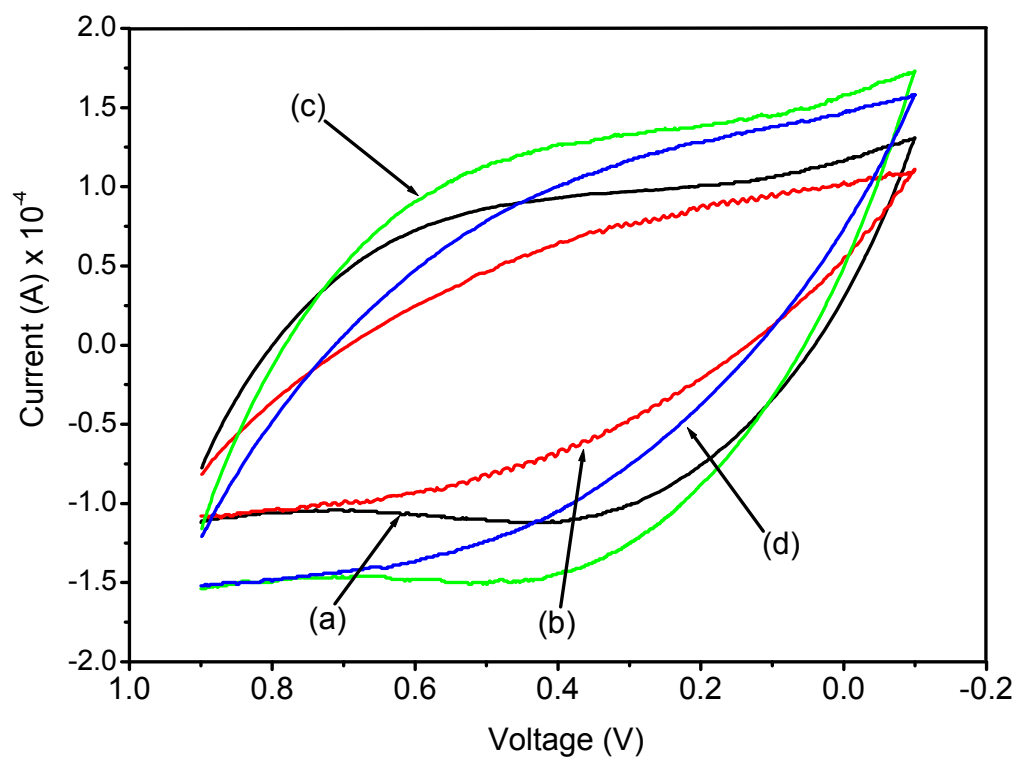
Appendix 5: Discharge curves of (a) CuO (b) 5wt.% CuO-MWCNTs and (c) 5wt.% (MnO$_2$/CuO)-MWCNTs.

Appendix 6: CV curves of (a) A-MWCNTs (b) 5wt.% CuO@300 °C-MWCNTs (c) 5wt.% CuO@400 °C-MWCNTs and (d) 5wt.% CuO@500 °C-MWCNTs.

Appendix 7: CV curves of (a) A-MWCNTs (b) 5wt.% NiO@300 ºC-MWCNTs (c) 5wt.% NiO@400 ºC-MWCNTs and (d) 5wt.% NiO@500 ºC-MWCNTs.

Appendix 8: CV curves of (a) A-MWCNTs (b) 5wt.% Co_3O_4@300 °C-MWCNTs (c) 5wt.% Co_3O_4@400 °C-MWCNTs and (d) 5wt.% Co_3O_4@500 °C-MWCNTs.